Fabrication and Characterization of Antibacterial Surfaces Derived From Geranium Essential Oil Using PECVD

Ph. D. Thesis

Ahmed Al-jumaili

July 2019

For the degree of Doctor of Philosophy

In the College of Science and Engineering

James Cook University

Supervisors:

Prof Mohan Jacob, Dr. Kateryna Bazaka and Dr. Mostafa Rahimi Azghadi

Declaration

I declare that this thesis is my own work and has not been submitted in any form for another degree or diploma at any university or other institute of tertiary education. Information derived from the published and unpublished work of others has been acknowledged in the text, and a list of references is given.

_____

Ahmed Al-jumaili

December, 2018

Statement of access to this thesis

I, the under-signed, the author of this work, understand that James Cook University will make this work available for use within the University Library, and via the Australian Digital Thesis Network, for use elsewhere.

I understand that as an unpublished work, a thesis has significant protection under the Copyright Act.

I do not wish to place any restriction on access to this thesis. However, any use of its content must be acknowledged and could potentially be restricted by future patents.

Ahmed Al-jumaili

December, 2018

Acknowledgements

First and foremost, I am greatly indebted to my supervisor Prof. Mohan Jacob for his support and guidance throughout my research work. All of my academic achievements have been accomplished because of his consistent assistance and inspiring guidance.

I would like to thank Dr. Katia Bazaka who contributed valuable expertise and excellent advices throughout all experimental and theoretical work in this thesis. I also appreciate the support of Dr. Mostafa Rahimi Azghadi.

I am gratitude to our collaborators A/Prof. Jeffrey Warner and Dr. Peter Mulvey from College of Public Health, Medical & Vet Sciences who provided their knowledge and facilities to run the antibacterial experiments in this thesis.

Thanks to my friends and colleagues, Surjith Alancherry and Avishek Kumar, who assisted in various experiments and data obtaining during this thesis, as well as created a highly supportive atmosphere to accomplish the work.

Special thanks to our administrative staff at the School of Engineering and Physical Sciences, Melissa Norton and Rebecca Steele for their excellent academic services.

Appreciations to JCU Advanced Analytical Centre crew who provided their assistance regarding AFM, SEM, ICP and Raman Spectroscopy characterizations. Also, thanks to the electrical workshop staff, John Renehan and Lloyd Baker.

It is with immense pleasure that I dedicate this thesis to every-member of my family, my Mom, my brother and my sisters who stood by me during my study and always offered their love, care and support.

Finally, I acknowledge that my PhD scholarship was financially funded by the Ministry of Higher Education and Scientific Research in Iraq. In addition, I acknowledge the financial support provided by James Cook University Graduate Research Scheme (GRS).

Abstract

Essential oils and plant extracts are rich sources of biologically-active compounds that can be used for manufacturing of antibacterial surfaces. This thesis reports the fabrication of pristine polymers, and zinc oxide/polymer films from geranium essential oil utilizing low power plasma-enhanced chemical vapor deposition technique (PECVD). The topographical, optical, mechanical, chemical, electrical and antibacterial properties of the fabricated films were in-depth studied.

Geranium-derived polymer films were fabricated at various input RF power. The resultant polymer were founded to be optically transparent in the visibly region. The refractive index, extinction coefficient, and optical band gap were found to be not significantly dependent on the RF power. The crosslinking of the material increased with increasing input power. The topographical features appeared to be uniform, smooth, and pinhole free for all samples, and the surface roughness increased with an increase in the input power. Sample fabricated at 10 W demonstrated a remarkable reduction in the number of cells, biovolume, or biofilm thickness, while there was no significant difference in the bacterial growth between samples fabricated at 50 W and control.

Zinc oxide nanoparticles were incorporated in the fabricated polymer films via a single-step approach that combines simultaneous plasma polymerization of geranium oil with thermal decomposition of zinc acetylacetonate $Zn(acac)_2$. The resultant nanocomposite thin films were systematically investigated. XPS survey proved the presence of ZnO in the matrix of formed polymers at 10 W and 50 W. SEM images demonstrated that the average size of ZnO nanoparticle slightly increased with an increase in the power of deposition from approximately 60 nm at 10 W to approximately 80 nm at 50 W. Confocal scanning laser microscopy images showed that viability of *S. aureus* and *E.coli* cells significantly reduced on surfaces of ZnO/composites compare to pristine polymers.

The electrical properties of pristine and ZnO/composites thin films were investigated in metal–insulator–metal (MIM) structures. It was found that the capacitance of the films decreases at low frequencies ($C \approx 10^{-11}$) and remains at a relatively constant value ($C \approx 10^{-10}$) at high frequencies. These films also have a low dielectric constant across a wide range of frequencies that decreases as the input RF power increases. The conductivity of pristine polymers was determined to be around 10^{-16}–$10^{-17}\ \Omega^{-1}\ m^{-1}$, which is typical for insulating materials. Incorporation of ZnO nanoparticles into the polymer films did not change the nature of charge transport, as the nanocomposite films were found to behave as an insulator. However, the conductivity slightly of nanocomposite materials slightly improved measuring $10^{-14}\ \Omega^{-1}\ m^{-1}$.

Increasing the input power, along with introducing hydrogen gas to the plasma tube, produces desired sp^2-bonded carbon nanostructures such as graphene materials. PECVD) had been utilized for the fabrication of high-quality vertically erected graphene nano-walls from geranium essential oil. The graphene synthesized using well-controllable system directly on silicon and quartz substrates without use any catalyst. SEM showed that the formed graphene had a length of few hundreds nanometers with thickness of 7 to 25 nm. AFM further confirmed the very sharp edges of the produced graphene. The material revealed relatively high water contact angle value ranging around 123˚. Antibacterial performance of graphene nano-walls was studied against gram-positive and gram-negative microorganisms. Confocal scanning laser microscopy images demonstrated that the viability of *E.coli* and *S. aureus* cells were 32% and 38% were alive on graphene compare to controls, respectively.

Contents

List of figures

List of tables

List of publications

1. Al-Jumaili, A., K. Bazaka, and M.V. Jacob, Retention of Antibacterial Activity in Geranium Plasma Polymer Thin Films. *Nanomaterials*, 2017. 7(9): p. 270.

2. Al-Jumaili, A.; Kumar, A.; Bazaka, K.; Jacob, M. Plant secondary metabolite-derived polymers: A potential approach to develop antimicrobial films. *Polymers* 2018, *10*, 515.

3. Al-Jumaili, A.; Alancherry, S.; Bazaka, K.; Jacob, M.V. The electrical properties of plasma-deposited thin films derived from pelargonium graveolens. *Electronics* 2017, *6*, 86.

4. Al-Jumaili, A.; Alancherry, S.; Bazaka, K.; Jacob, M. Review on the antimicrobial properties of carbon nanostructures. *Materials* **2017**, *10*, 1066.

5. Al-Jumaili, A.; Mulvey, P.; Kumar, A.; Prasad, K.; Bazaka, K.; Warner, J.; Jacob, M.V. Eco-friendly nanocomposites derived from geranium oil and zinc oxide in one step approach. *Scientific Reports* **2019**, *9*, 5973.

6. Ahmed Al-Jumaili, K.B., and Mohan V. Jacob. Electrically-insulated coatings derived from ZnO/polymer plasma composite films. *Advances in Materials Science and Engineering-Hindawi* **2018** (under review).

Book chapter:

Al-Jumaili, A.; Alancherry, S.; Grant, D.; Kumar, A.; Bazaka, K.; Jacob, M.V. Plasma treatment of polymeric membranes. In *Non-thermal plasma technology for polymeric materials*, Elsevier: 2019; pp 211-240.

Also contributed to:

Kumar, A.; Grant, D.; Alancherry, S.; Al-Jumaili, A.; Bazaka, K.; Jacob, M.V. Plasma polymerization: Electronics and biomedical application. In *Plasma science and technology for emerging economies*, Springer: 2017; pp 593-657.

CHAPTER I

Introduction

I.1 Rational

Even though synthetic antibiotics have been the best weapon for eradicating microbial infections since the arrival of penicillin, the overuse of these medications is gradually rendering them ineffective. It is anticipated that if new strategies are not developed soon, medical treatments could retreat to the era where slight injuries and common infections develop into serious medical problem. One promising strategy has been inspired by the inherent bioactivity of plant secondary metabolites. It is known that most plants produce these organic molecules as antimicrobial agents to combat harmful microorganisms. In their liquid form, geranium, lavender, garlic, oregano, lemongrass, cinnamon oils are good examples of naturally-occurring substances with strong antibacterial activity. Their individual constituents, e.g. citronellol and geraniol are aromatic acyclic monoterpene alcohols that are very powerful bactericides. These essential oils have proved broad-spectrum nonspecific biocide activities against different microbial species such as *E. coli*, *P. aeruginosa*, and several drug-resistant bacteria (e.g. *MRSA*).

Current progresses in cold plasma polymerization have enabled the conversion of essential oils and their derivatives into thin, highly-adherent and defect-free optically-transparent coatings, whose biological activity and degradation kinetics can be controlled by controlling the chemical structure of the precursor and the plasma processing conditions. From a processing point of view, various essential oils are compatible with plasma polymerization, which is in essence a chemical vapor deposition process enhanced by the catalytic activity of plasma, because they are highly volatile at room temperature no external heat or carrier gas are required to deliver the precursor macromolecules to the fabrication zone. The resultant films have more than a few advantages such as low cytotoxicity, long-term stability, and a reduced possibility of emerging bacterial resistance. These advantageous properties render the plasma films produced from plant secondary metabolites a suitable candidate for bioactive coating applications.

In this regard, that plasma polymers are documented for favorable electrical properties (e.g. dielectric constant) making them a suitable candidate for various organic electronics industries. Organic films derived from essential oils such as terpenol, linalyl acetate, and γ-terpinene have been demonstrated to be appropriate for different applications such as insulating layers, encapsulation layers in organic electronics, and biocompatible coatings for implants. As organic microelectronics is a speedily developing technology to manufacture commercially feasible

devices, research on new plasma polymers and their approaches should yield various possible applications.

Plasma system can be modified to introduce inorganic nanoparticles in the configuration of the formed polymer, where the chemical reaction in the gas-phase and the formation of nanoparticles simultaneously occurred. Subsequently, plasma-composite materials comprise inorganic nanoparticles within short polymeric chains that are unsystematically branched and terminated with a high cross-linking medium. It is interesting to notice that even an extremely low amount of metal are needed to yield important changes in the polymer properties. Among different materials, zinc oxide nanoparticles have shown desired biological and electrical properties such as powerful antibacterial performance, high luminous transmittance chemical/physical stability and possess wide and direct bandgap of 3.4 eV and a large exciton binding energy of 60 meV. Zinc oxide is also relatively low cost, available in commercial quantities and can be prepared in several nanostructure morphological forms (e.g. spherical particles, nano-rode, etc). Accordingly, ZnO is important from both biological and electrical point of view.

Based on the above-mentioned points, renewable geranium essential oil was selected as a monomer for this project. Environmentally friendly plasma polymerization technique was utilized as a fabrication method due to its capability of manufacturing high quality thin films. The thermal decomposition of zinc acetylacetonate hydrate (Zn $(C_5H_7O_2)_2 \cdot xH_2O$) was used to produce zinc oxide nanoparticles that integrated in the structure of geranium plasma polymers.

I.2 Research Objectives

This project aims to produce a range of novel organic thin films from renewable geranium essential oil for advanced and emerging applications in biomedical and microelectronics fields. This is accomplished through addressing the following goals:

- To fabricate organic thin films derived from geranium monomer using plasma polymerization technique and characterize the material's optical, morphological, mechanical, and chemical properties.

- To retain the inherent antibacterial activity of geranium essential oil into active polymer coatings through plasma polymerization technique

- To develop green nanocomposites produced from geranium oil and the thermal decomposition of zinc acetylacetonate in one step modified-plasma technique.

- To study the feasibly of the composites as antibacterial coatings for suitable medical devices and implants.

- To determine the material's electrical properties, both pristine polymer and ZnO doped composite. This included investigations into the dielectric constant, the conductivity and the mechanisms of charge transport through the material.

- To produce high quality graphene nano-walls from geranium oil using high-power PECVD without the aid of any catalyst.

This thesis work has demonstrated that the nano-structural thin films can be developed from geranium essential oils through plasma polymerization technique. Achieving the above objectives led to a number of contributions in the fields of polymers and composites antibacterial coatings. The developed material is also expected to benefit the progression of current and novel applications in organic microelectronics. Overall, the work accomplished in this thesis is likely to have a significant impact on the research and applied fields of employing natural and environmentally friendly precursors for producing functional advanced materials.

1.3 Thesis Organization

This thesis is presented as a sequence of chapters, each representing a manuscript at various stages of publication. A short abstract is given at the beginning of each chapter to ensure consistency and flow when reading chapters in sequential order.

The reported work in this thesis was completed by the candidate Ahmed Al-jumaili and has involved deep discussions with academic supervisors and experts as evident in the all publications. Project supervisors Prof. Mohan Jacob and Dr. Katia Bazaka shared expertise in the field and provided advices for all Chapters. A/Prof Jeffrey Warner and Dr. Peter Mulvey provided help in antibacterial experiments and analysis of the data in chapter IV.

Chapter I shows the main objective and the rational for this study.

Chapter II scrutinized the challenges of bacterial adhesion, biofilms formation, and medical device-associated infections are reviewed. Also, it highlights the up-to-date progress in the fields of antibacterial surfaces derived from essential oils, and their applications in biomaterials. The retention of inherent antimicrobial activity of plant secondary metabolites within solid polymers, as bioactive coatings, are broadly discussed. This chapter is published as *Al-Jumaili, A.; Kumar, A.; Bazaka, K.; Jacob, M.V. Plant Secondary Metabolite-Derived Polymers: A Potential Approach to Develop Antimicrobial Films. Polymers 2018, 10, 515.*

Chapter III illustrated the thin film fabrication method and the details of the experiments. In addition, the material properties, and antibacterial activity of geranium oil-based polymers fabricated using plasma polymerization are reported. The results of this study have been published as *Al-Jumaili, A.; Bazaka, K.; Jacob, M.V. Retention of Antibacterial Activity in Geranium Plasma Polymer Thin Films. Nanomaterials 2017, 7, 270.*

Chapter IV describes the fabrication and characterizations of nanocomposite films produced from geranium essential oil and the thermal decomposition of $Zn(acac)_2$ in one step hybrid-plasma system. The chemical composition, surfaces characteristics, antimicrobial performance and metal release of the designed nanocomposite are systematically presented.

Chapter V reports the study of the influence of power deposition on the dielectric constant, the conductivity and the mechanisms of charge transport through of the fabricated polymers. *Al-Jumaili, A.; Alancherry, S.; Bazaka, K.; Jacob, M.V. The Electrical Properties of Plasma-Deposited Thin Films Derived from Pelargonium graveolens. Electronics 2017, 6, 86.* Section II of this chapter investigates the electrical properties of ZnO NPs incorporated in the plasma geranium films.

Chapter VI discuss the formation of high quality graphene materials by PECVD technique. Raman spectroscopy, surface characterization and the antibacterial performance of the formed vertically erected graphene nano-walls are discussed in details.

Chapter IX provides the overall conclusion about the thesis and recommendations for the future work.

Chapter II

Literature Review

Chapter II reviews scientific background for the research presented in this thesis. It firstly focuses on challenges of bacterial adhesion, biofilms formation, and medical device-associated infections. Then, this chapter highlights current progress in plant secondary metabolites-derived antimicrobial polymers and their applications in biomaterials.

Chapter II was published as *Al-Jumaili, A.; Kumar, A.; Bazaka, K.; Jacob, M.V. Plant Secondary Metabolite-Derived Polymers: A Potential Approach to Develop Antimicrobial Films. Polymers 2018, 10, 515.*

Abstract

The persistent issue of bacterial and fungal colonization of artificial implantable materials and decreasing efficacy of conventional systemic antibiotics used to treat implant-associated infections has led to the development of a wide range of antifouling and antibacterial strategies. This article reviews one such strategy where inherently biologically active renewable resources, i.e. plant secondary metabolites (PSMs) and their naturally occurring combinations (i.e. essential oils) are used for surface functionalization and synthesis of polymer thin films. With a distinct mode of antibacterial activity, broad spectrum of action and diversity of available chemistries, plant secondary metabolites present an attractive alternative to conventional antibiotics. However, their conversion from liquid to solid phase without significant loss of activity is not trivial. Using selected examples, this article shows how plasma techniques provide a sufficiently flexible and chemically reactive environment to enable the synthesis of biologically-active polymer-coatings from volatile renewable resources.

II.1. Introduction

In 1963, Lieutenant W. Sanborn was first to systematically relate surface contamination to the transmission of microorganisms [1]. Later, numerous studies have confirmed the attachment and proliferation of microbial cells on artificial surfaces, such as that of medical devices [2, 3]. In spite of significant progress in the development of antibacterial and antifouling surfaces, microbial adhesion and resulting development of a thick sessile layer, i.e. the biofilm, on the surfaces of synthetic implants remains a major issue with their clinical use [4]. Therapeutic statistics have demonstrated that approximately 80% of the worldwide surgical site associated-

infections may relate to the microscopic biofilm formation [5]. Further, owing to microbial infection, and subsequent failure of medical devices, there has been a significant increase in the number of revision surgeries [6, 7]. In the United States alone, approximately 17 million new biofilm-related infections are reported annually, leading to approximately 550,000 fatalities each year [8].

Emergence of bacteria that are resistant to typically used antibiotics is now well recognized [9, 10]. The most serious problem with antibiotic resistance is that some pathogenic bacteria have now become resistant to virtually all standard antibiotics [11, 12]. Significant examples are methicillin-resistant *Staphylococcus aureus* (MRSA), vancomycin-resistant *Enterococcus* (VRE), multi-drug-resistant *Mycobacterium tuberculosis* (MDR-TB) and *Klebsiella pneumoniae* carbapenemase-producing bacteria [13]. Moreover, today, MRSA, a leading cause of most common hospital infections, and *Neisseria gonorrhoeae*, the pathogen responsible for gonorrhoea, are almost resistant to benzyl penicillin, while in the past, these pathogens were highly susceptible to the drug [14]. The impact of microbial resistance can be diminished considerably through reduced antibiotic consumption.

Renewable resources have attracted some research attention as precursors for developing tailored bioactive polymers that are capable of minimizing the rate of bacterial adhesion and biofilm growth in healthcare facilities. Within the therapeutic arsenal of naturally-available alternatives that have been explored, plant secondary metabolites (PSMs), such as essential oils and herb extracts have revealed relatively powerful broad-spectrum antibacterial activities [15, 16]. Good examples of currently used PSMs are tea tree (*Melaleuca alternifolia*), geranium, zataria, and cinnamon oils that have shown inherent bactericidal performance in their liquid and/or vapour form toward important pathogenic microbes. Due to the presence of a large number of active molecules within a single essential oil or plant extract, their antimicrobial pathway is not fully understood and cannot be attributed to a particular mechanism [17]. However, the pharmaceutical, cosmetic and food industries have recently paid great attention to bioactive PSMs, by way of the usage of natural additives as a substitute for synthetic preservatives [18]. Indeed, PSMs are a relatively low-cost renewable resource available in commercial quantities, with limited toxicity and potentially have different biocidal mechanisms to synthetic antibiotics, which makes them an appropriate precursor for “green” functional polymeric materials. On the other hand, using PSMs for surface functionalization through immobilisation or synthesis of coatings without loss of functionality is challenging, in part due to the issues with solubility and volatility of these precursors. Plasma-assisted technique overcomes these challenges, allowing the fabrication of a polymerized 3D matrix from renewable precursors with control over its surface properties and chemical functionality. Under appropriate fabrication conditions, plasma-enabled synthesis may

help preserve/retain the inherently antimicrobial functionality of PSMs within the solid polymer-like thin films. Plasma polymers of PSMs (PP-PSMs) reveal several advantages including low cytotoxicity, long-term stability and a reduced risk of developing microbial resistance. These advantageous properties render PP-PSMs a suitable candidate for bioactive coating applications.

Thus, the focus of this article is on:

- The challenge of bacterial adhesion, biofilms formation, and medical device-associated infections.
- The retention of inherent antimicrobial activity of sustainable monomers, e.g. plant secondary metabolites within solid polymers with the aim of applying them as bioactive coatings.

II.2. Microbial contamination

Global production of medical devices and associated materials is an industry worth over $180 billion, and is expanding swiftly [19]. Microbial contamination of these biomaterials is a serious and widespread problem facing current health system because it often leads to devastating infections and failure of the affected device. Adhesion of planktonic microorganisms (e.g. bacteria and fungi) to surfaces is the first stage during surface colonisation, followed by the subsequent formation of biofilms which provide an ideal environment for the microbial community to flourish and effectively evade treatment. An active biofilm can be up to 1000 times more resistant to an antimicrobial treatment than planktonic bacteria of the same species [20, 21]. Biofilms act as a nidus for systemic pathogenic infections, including dental cavities, periodontal disease, pneumonia associated with cystic fibrosis, otitis media, osteomyelitis, bacterial prostatitis, native valve endocarditis, meloidosis and musculoskeletal infections [22, 23]. Thus, a thorough understanding of the mechanisms by which microorganisms attach to the substrate, and the structure and dynamics of biofilms formation is necessary to develop bio-active coatings that reduce or prevent medical device-associated infections.

II.2.1. Bacterial adhesion

Bacterial cells are essentially capable of attaching to all natural and artificial surfaces [24]. Yet, it has been assumed that bacteria favourably stick to rougher surfaces for three reasons: (i) a higher surface area available for attachment, (ii) protection from shear forces, and (iii) chemical changes that cause preferential physicochemical interactions [25]. Also, there is consensus among scientists that the solid-liquid interface between a surface and an aqueous medium (e.g. water and blood) provides a suitable environment for the adhesion and propagation of bacteria [26].

Before the first microorganism reaches the surface, water, salt ions, or proteins that exist in the environment will adhere to the substrate, with the nature of the attachment dependent on the properties of the material [27] and the chemistry of the environment. Consequently, a single layer of organic macromolecules called a 'conditioning film' is formed [28]. The characteristics of conditioning films in turn significantly influence the surface colonization. As the bacterial cell approaches the surface (a few nanometres), the initial stage of adhesion is governed by a number of physico-chemical effects, which include long-range and short-range forces. The long range forces include gravitational, van der Waals, and electrostatic interactions, while the short range forces include hydrogen bonding, dipole–dipole, ionic, and hydrophobic interactions [21, 29]. The initial microbial attachment is considered reversible, as the cell will attach to the conditioning film not the surface itself. During adhesion to the surface, various bacteria can transiently produce flagella that render them very motile. Depending on the species, microorganisms may have appendage such as fimbriae, polymeric fibers also called pili or curli, which enhance the attachment to surfaces [30]. For example, curli fibres of *E. coli* are 4-6 nm wide unbranched filaments, having a distinctive morphology that can be easily detected by electron microscopy [31]. If the microorganisms are not immediately removed from the surface, they can anchor themselves more permanently by producing a large amount of fibrous glycocalyx that performs the role of the 'cement' to attach cells to the targeted surface [32].

II.2.2. Biofilms formation

After adhering to solid surfaces, the next step of permanent attachment is growing a bacterial 'sanctuary', which is the biofilm. Biofilm formation is a four stage process which includes: (i) irreversible attachment, (ii) early development, (iii) maturation, and (iv) detachment or dispersal of cells, as seen Figure **II.** 1 [29]. In the irreversible adhesion, major changes occur in gene/protein expression of microbial cells. It has been shown conclusively that bacteria secrete a highly hydrated layer (biofilm) that provides a shield against host defence system and antibiotics, and strengthens the attachment of the microorganisms to the surface. Early steps of biofilm formation are controlled by physical adsorption processes and evolution dynamics of planktonic pathogens [33].

A biofilm cluster consists of accumulations of extracellular polymeric substances (EPS), primarily polysaccharides, proteins, nucleic acids and lipids [34, 35]. Typically, a viable biofilm involves three organic layers. The first layer is attached to the surface of the tissue or biomaterial, the second layer is called the 'biofilm base', which holds the bacterial aggregation, and the third layer, known as the 'surface film', performs as an outer layer where planktonic organisms are released [6]. Biofilm architecture is heterogeneous both in space and time. The thickness of a

biofilm varies depending on the microbial species. For example, the mean thickness of *P. aeruginosa* biofilm is about 24 μm, while *S. epidermidis* has a mean biofilm thickness of 32.3 μm, and can reach more than 400 μm in some species [36]. Active biofilms are highly hydrated, with 50-90% of the overall area at each sectioning depth comprising EPS and liquid [37]. Direct microscopic observation has shown that biofilm clusters accumulate a large quantity of pathogens within a small area, with microorganism cell densities on an infected surface reaching 10^6 cells/cm^2 [38]. Microorganisms communicate with each other inside a biofilm by producing chemotactic particles or pheromones, in a process called 'quorum sensing' [39]. Biofilm sanctuaries can include a single infectious species or multiple infectious species, as well as non-pathogenic microorganisms which nevertheless can produce substances that would benefit the survival and proliferation of the pathogenic species. In the case of the infection of medical devices and implants, a single bacterial species is usually responsible for biofilm formation. While in environmental surfaces, groupings of various species will usually dominate the biofilm [40].

Hydrodynamic, physiological, and ecological conditions, along with presence of other colonisers and harmful agents (e.g., antibiotics and antimicrobial nanoparticles) considerably influence the biofilm structure. For example, biofilm structures of *P. fluorescens* and *P. aeruginosa* are significantly affected by nutritional cues, e.g., carbon and iron availability in their surroundings, respectively [41]. It has been reported that shear forces affect the distribution of micro-colonies due to the passage of fluid over the biofilm. At low shear forces, the colonies are formed like a channel, while at high shear forces, the colonies are extended and susceptible to rapid vibrations [42]. These channels are essential for bacteria to transport necessary water, nutrients and oxygen to the bacterial community within the biofilm [43]. It has been shown that an increasing loading rate applied under a stable shear stress induced the formation of thicker and rougher biofilms [44]. Detachment is a fundamental process in biofilm development that benefits bacterial life cycle by allowing planktonic cells to return to the environment and settle new territories [45]. Three different biofilm strategies have been suggested to elucidate biofilm detachment: (i) swarming dispersal, where planktonic cells are freed from a bacterial cluster; (ii) clumping dispersal, where aggregates of microbial cells are separated as clumps; and (iii) surface dispersal, where biofilm matrices move across infected surfaces through shear-mediated transport [46]. Detachment initiation has been proposed to initiate in response to specific endogenous or/and exogenous cues (e.g. a lack of nutrients that causes starvation, or high cell densities) [47]. The event of detachment is complex and random. In some cases, separation of large masses (cell clusters above 1000 μm^2) from mature biofilms represents only 10% of the detachment process, yet accounts for more than 60% of the microorganisms detached [48]. A considerable amount of literature has been published on biofilms, yet the mechanisms of biofilm detachment are poorly understood [49, 50]. Better understanding to the detachment mechanisms is necessary to evaluate accurately the spatial

distribution of the bacterial cells in their environment, their ability to survive as well as their resistance to biocides.

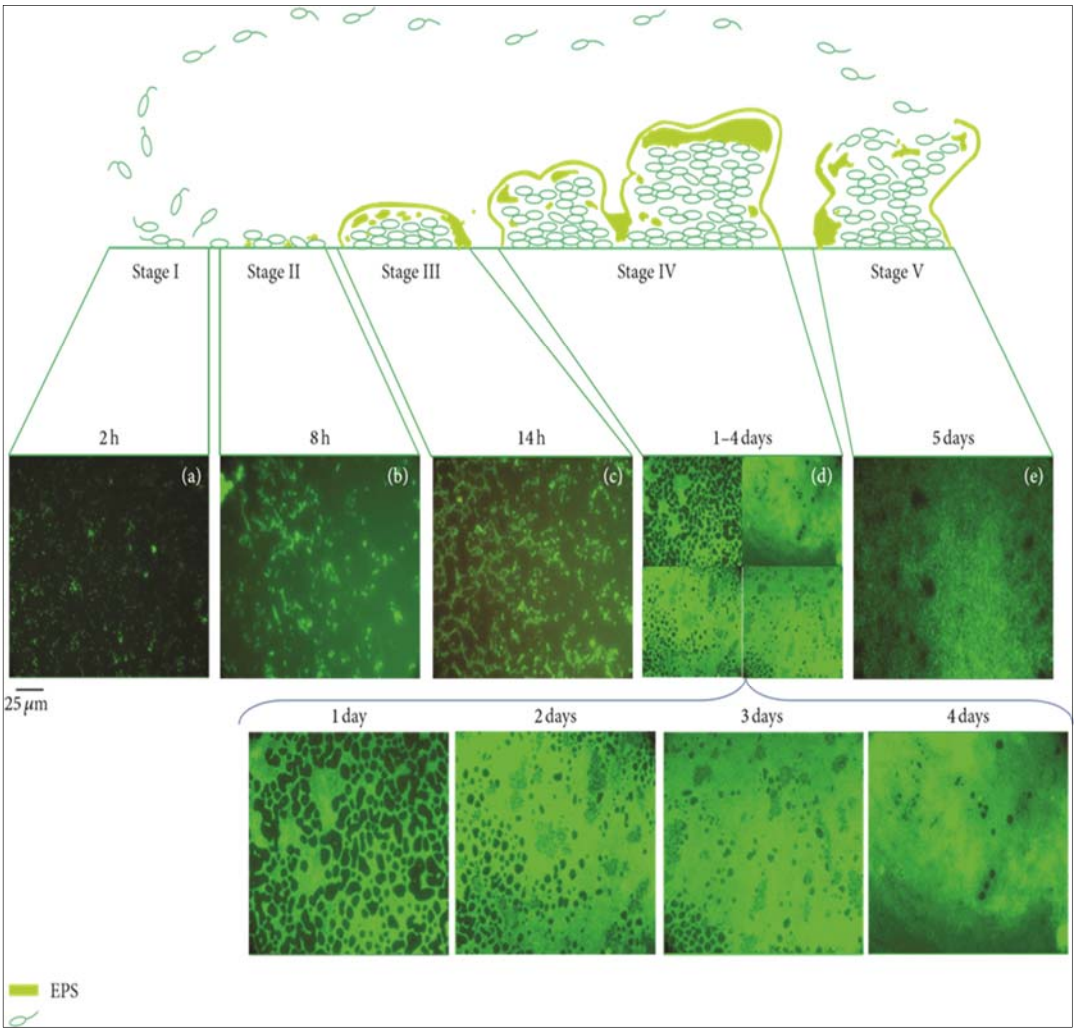

Figure II.1. Schematic of the lifecycle of P. aeruginosa grown in glucose media. Images of inverted fluorescence microscopy with 400x magnification present stages of biofilm development. In stage I, planktonic bacteria attach to a solid surface. In stage II, the attachment becomes irreversible. Stage III elucidates the micro-colony foundation. Stage IV illustrates the biofilm maturation and growth of the three-dimensional bacterial sanctuaries. In stage V, dispersion occurs and free planktonic cells are released from the cluster biofilm to colonize new locations. Images characterize a 250 × 250 μm^2 field. Reproduced with permission from [51].

II.2.3. The impact of biofilm formation in healthcare environment

Microbial infections related to bacterial attachment and biofilm formation have been detected on various medical devices including prosthetic heart valves, orthopedic implants, intravascular catheters, artificial hearts, contact lenses, left ventricular assist devices, cardiac pacemakers, vascular prostheses, cerebrospinal fluid shunts, urinary catheters, ocular prostheses and contact

lenses, and intrauterine contraceptive devices [52]. The three most common device-related infections are central line-associated bloodstream infection, ventilator-associated pneumonia (VAP), and Foley catheter-associated urinary tract infection (UTI) [53]. Studies have shown that 60-70% of nosocomial infections are associated with some type of an implanted medical device [54]. More specifically, the Centre for Disease Control and Prevention in the USA reported that of the infections in medical devices, 32% are urinary tract infections, 22% are surgical site infections, 15% can be attributed to pneumonia and lung infections, and 14% constitute bloodstream infections [55]. Microorganisms also form biofilms on damaged vascular endothelium of native heart valves in patients with pre-existing cardiac disease, causing *Candida* infectious endocarditis [35]. It is known that biofilms of *Candida* species cause malfunctioning of the valve in tracheo-oesophageal voice prostheses, leading to an increase in air flow resistance and potential fluid leakage [56]. Furthermore, scanning electron microscopy confirmed biofilm development at the tip of urinary catheters even after a short period of exposure [29].

While a large number of microorganisms are capable of causing infections, those that are able to survive and thrive in clean sites, such as that of clinics and hospitals, present a considerable threat [57]. These organisms include gram-positive *Enterococcus faecalis*, *Candida albicans*, *Staphylococcus aureus*, *Staphylococcus epidermidis*, and *Streptococcus viridans*; and gram-negative *Escherichia coli*, *Klebsiella pneumoniae*, *Proteus mirabilis*, and *Pseudomonas aeruginosa*. Prevalence of these pathogens is a serious problem in modern societies. For example, *C. albicans* causes superficial and serious systemic diseases, and is known as one of the major agents of contamination in indwelling medical devices [58-60]. *P. aeruginosa* is an opportunistic pathogen of immunocompromised hosts and can cause native acute and chronic lung infections that result in significant morbidity and mortality, especially in cystic fibrosis patients [61, 62]. *S. aureus* and *S. epidermidis* have been shown to strongly adhere and form biofilms on metallic implants, e.g. orthopaedic screws, leading to potential device failure [6].

II.3. The antibacterial activities of PSMs

Even though synthetic antibiotics have been the best weapon for eradicating microbial infections since the arrival of penicillin, the overuse of these medications is gradually rendering them ineffective. It is anticipated that if new strategies are not developed soon, medical treatments could retreat to the era where slight injuries and common infections develop into serious medical problem. One promising strategy has been inspired by the inherent bioactivity of plant secondary metabolites [63]. It is known that most plants produce these organic molecules as antimicrobial agents to combat harmful microorganisms [64, 65]. In the past few decades, the progress in the synthesis of nanoscale materials, in particular plasma assisted-fabrication provides the means to retain the antimicrobial activities of PSMs within bioactive coatings. This family of techniques is

compatible with PSMs, and offers several advantages such as being an environmentally friendly, versatile, and low-cost technology (discussed further in this article).

In their liquid form, lavender, garlic, oregano, lemongrass, cinnamon oils are good examples of naturally-occurring substances with strong antibacterial activity [66, 67]. Their individual constituents, e.g. citronellol and geraniol are aromatic acyclic monoterpene alcohols that are very powerful bactericides [68-71]. Terpinene-4-ol, a major component of tea tree oil, is a broad-spectrum nonspecific biocide well-known as a natural agent against microbial species such as *E. coli*, *P. aeruginosa*, *Acinetobacter baumannii*, and several drug-resistant bacteria (e.g. MRSA) [72]. A number of PSMs have been used against cancer cells, whereas others are currently used in food preservation [73, 74]. In their vapour phase, a number of PSMs has demonstrated strong antibacterial activities [75, 76]. So far, there are thousands of natural oil currently known. Among them, 300 oil are important and commonly used in the pharmaceutical, food, sanitary, agronomic, perfume and cosmetic productions [77].

PSMs are extracted as part of highly complex mixtures of various individual constituents (often hundreds of components) [78]. PSMs were reported to contain a variety of chemical groups in their structure, such as alcohols (terpineol, menthol, geraniol, linalool, citronellol, borneol), aldehydes (benzaldehyde, citral, cinnamaldehyde, citronellal, vanillin), acids (benzoic, cinnamic, isovaleric, myristic), esters (acetates, cinnamates, benzoates, salicylates), hydrocarbons (cymene, sabinene, myrcene, storene), ketones (carvone, camphor, pulegone, menthone, thujone), phenol ethers (safrol, anethol), phenols (carvacrol, eugenol, thymol), terpenes (camphene, cedrene, limonene, pinene, phellandrene) and oxides (cineol)[79].

II.3.1. The antibacterial mechanisms of PSMs

The antibacterial action of PSMs (in their liquid form) is complex and not yet fully understood; it potentially involves several mechanisms, as summarised in Figure II.2. A number of researchers have proposed that the hydrophobic nature of PSMs allows them to accumulate and perturb the structure and function of lipids of the microbial cell membrane, disturbing the biological function and causing failure of chemiosmotic control and rendering the membrane more permeable [66, 80]. An increase in membrane fluidity and permeability results in membrane expansion, damage of membrane-embedded proteins and triggers inhibition of respiration system and alteration of ion transport activities of bacterial cells [81]. For example, carvacrol oil was reported to make the cell membrane permeable for K^+ and H^+, consequently dissipating the proton motive force and inhibiting ATP production [82]. Similarly, menthol and citronellol causes an expansion of the cell membrane, leading to passive diffusion of ions between the stretched phospholipids [83]. Ultee and Smid (2001) hypothesized that during exposure to PSMs, the driving force for optimal

secretion of the toxin (ATP or the proton motive force) is not sufficient, causing accumulation of the toxin inside the cell, which in turn inhibits normal microbial metabolism [84]. Some active PSMs are capable to coagulate the microbial cytoplasm, leading to cells inactivation [85]. For example, it has been obsedrved that coagulated materials (related to denatured membranes, cytoplasmic constituents, and proteins) were formed outside of the bacterial body when cells (*E. coli*) were grown in the presence of tea tree oil. These coagulates were released through microscopic holes produced in the cell wall as a result of the interaction with the oil [86].

Exposure to PSMs can lead to the reduction in enzymatic activities, loss of turgor pressure, changes in DNA synthesis and inhibition of different metabolic functions [82]. Moreover, some oils, such as rose, geranium, lavender and rosemary have been shown to inhibit cell-cell communication, affecting the quorum sensing (QS) network in the bacterial community [87]. QS-system is vital for bacterial growth and hence any interference with the sensing network may reduce pathogenicity, biofilm formation, and antibiotic resistance during infection events.

The antimicrobial performance of PSMs is linked to their chemical structure, particularly the presence of -OH functional groups [88]. Each compound may reveal a different biocidal mechanism toward microorganisms [83]. The bioactivity of several active oils is associated with the presence of phenolic groups. For example, the antimicrobial efficacy of clove, thyme, and oregano oils is related to the presence of phenol-containing eugenol, thymol, and carvacrol, respectively [89]. However, other findings indicate that the components present in high quantities with the oil are not necessarily responsible for the entire biological activity of a PSM. The antibacterial performance of these complex mixtures relies on a variety of synergistic effects of different sub-components in the oil. Furthermore, it can also be attributed to the presence of other components that may be effective even in small quantities [90, 91]. In the case of essential oils containing a high percentage of phenolic compounds (e.g. carvacrol, thymol), it can be assumed that their bactericidal action would be similar to other phenolic groups, e.g. by way of the disturbance of the membrane, disorder the proton motive force, electron flow, and coagulation of cell contents [80]. In the case of complex mixtures, where numerous active molecules are present, potential synergistic and antagonistic influences, as well as minor compounds that can have an important contribution to the oil's activity need to be considered [92, 93]. It is important to indicate that the biocidal mechanisms of PSMs are dissimilar from currently used synthetic antibiotics, which should minimise the likelihood of the development of microbial cross-drug resistance [94].

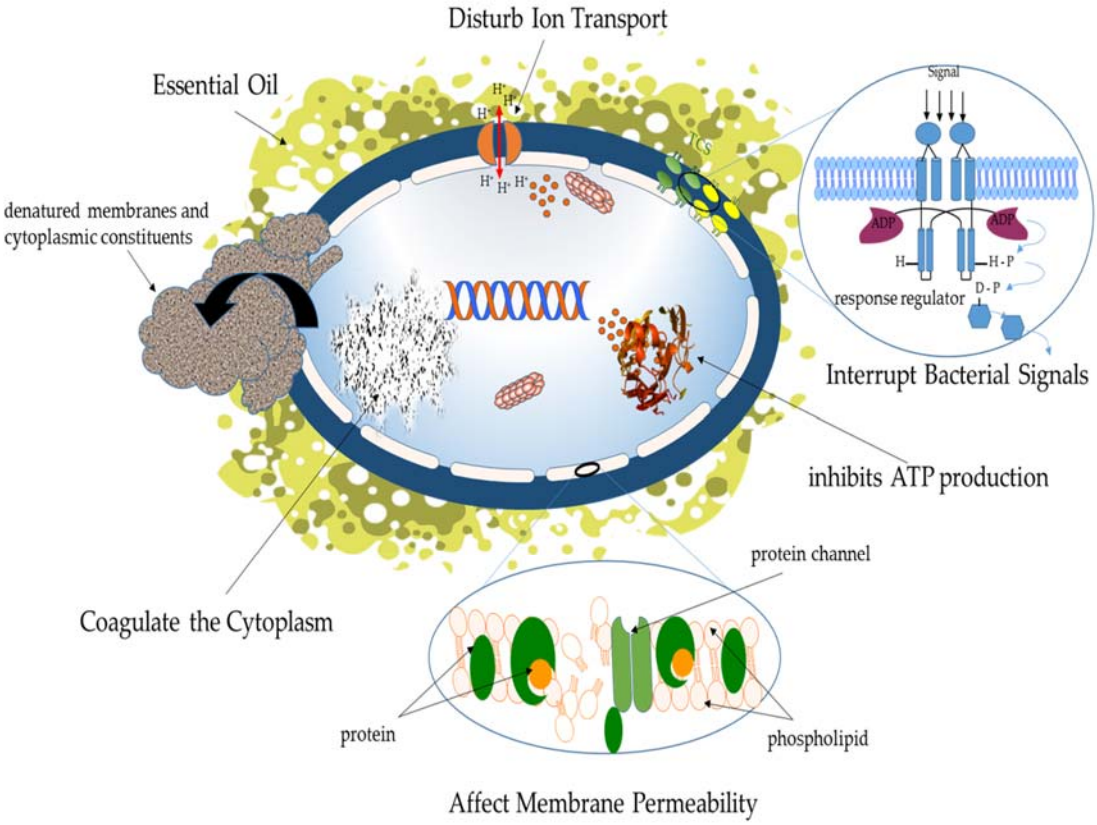

Figure II.2. Scheme represents the proposed antibacterial mechanisms of secondary planet metabolises in their liquid form.

II.3.2. Sustainable polymers from bioactive essential oils

Ecological concerns of current petroleum processing, along with economic recession, depleting reserves, and political aspects, have led to increased interest in the production of sustainable polymers derived from renewable resource [95, 96]. These eco-friendly polymers can be derived from a wide range of possible precursor materials, including oxygen-rich monomers (e.g. carboxylic acids), hydrocarbon-rich monomers (fatty acids, terpenes, vegetable oils), and non-hydrocarbon monomers (carbon dioxide) [97]. So far, polymers derived from essential oils, vegetable oils, bio-ethanol, cellulose, fats, resins, naturally occurring polysaccharides, microbial syntheses and other natural ingredients have been widely used for a variety of applications [98-103]. Essential oils, in particular, are renewable in nature, relatively inexpensive, available in commercial quantities, and display minimal toxicity compared to many conventionally-used precursors, which makes them an appropriate precursor for “green” functional materials. Among

them, terpenes (major components in a large number of essential oils) have received considerable attention. Their structure contains one or more carbon–carbon double bonds, showing a carbon skeleton of isoprene. The abundance of double bonds allows for cationic and radical polymerization of terpenes, along with epoxidation as a path to biodegradable oxygenated polymers [104]. Cationic polymerization has been generally accepted to be the most appropriate kind of chain reaction for these monomers [105]. However, essential oils have not been widely applied for production of bioactive polymers due to limitations associated with fabrication systems and oil properties [106, 107]. These limitations include challenges in controlling the surface chemistry and morphology of the synthesised materials, and solubility and/or volatility of the natural monomers.

Recent technological advances in the field of controlled polymerization, catalysis, nano-encapsulation, and effective organic functionalization, give great potential for the application of essential oils in manufacturing of sustainable polymers with innovative designs and characteristics. This allows the fabrication of organic films with good control over film thickness, physico-chemical properties and, importantly, biological functionality. For instance, it was possible to successfully engineer antibacterial UV-cured networks by using a thiol-ene route with covalent immobilization of natural terpene (linalool and a trithiol) as antibacterial agents, without employing any organic solvent. These bio-based materials exhibited attractive thermal properties, not affected by water penetration under high moisture conditions, and strong inhibition against microorganisms [108]. Chen et al. (2012) developed reversible transfer polymerization approach to design a series of cationic rosin-containing methacrylate bioactive-copolymers. The antibacterial activities of these rosin-containing copolymers were found to be dependent on both the degree of quaternization of rosin group, the molecular weight of copolymers, along with the conformation of hydrophobic group [109]. Furthermore, a cinnamon essential oil/cyclodextrin integrated into polylactic acid nanofilm made by electrospinning and co-precipitation showed strong antimicrobial activity [110].

Several studies have been carried out in order to incorporate active essential oils into selected polymers through applying emulsification or homogenization methods, where ultra-fine emulsions of oils are formed containing polymer at the continuous aqueous phase. Upon drying, lipid droplets remain incorporated into the polymer structure. The releasing rate of the embedded-oil from films is subject to multiple factors, such as electrostatic interactions between the oil and the polymer chains, osmosis, structural variations induced by the presence of the oil as well as environmental circumstances [111]. Remarkably, a small fraction of an incorporated essential oil within a polymer structure is sufficient to achieve desired antimicrobial properties. For example, quince seed mucilage films containing low percentage (1.5 - 2%) of oregano essential oil were

reported to be very effective against several microorganisms, including *S. aureus, E. coli* and *S. putrefaciens* [112]. Other findings showed that inactive chitosan films were transformed into bioactive materials when a small quantity (~1-2%) of extracts from two endemic herbs (*Thymus moroderi* or *Thymus piperella*) were integrated within the films [113].

Encapsulation of oils has been developed as one such technology that has great potential to improve the physical stability of the active components, protecting them from degradation due to environmental aspects (e.g. oxygen, light, moisture, pH) [114]. Among the nanometric encapsulation structures currently being used, nanoemulsions are mainly utilized due to the possibility of formulation with natural components and the compatibility with industrially scalable manufacturing processes by high pressure homogenization [115]. Nanoemulsions are defined as emulsions with ultra-small droplet size of approximately 100 nm. At this tiny dimension, there is a potential of enhancing physicochemical properties and stability of the active compound. In addition, the oil bioactivity can be considerably increased, since significant increases in the surface area per unit of mass can be achieved, improving the passive mechanisms of cell absorption, which again allow for the reduction of the oil quantity required to ensure antimicrobial action [116]. The encapsulated essential oils are promising antimicrobial agents for biodegradable/edible coatings in food packaging industries to inhibit pathogenic microorganisms [117]. It has been reported that the encapsulation in nanoemulsion formulation of a terpenes mixture and limonene increased the antimicrobial performance of the pure compounds against various microorganisms such as *E. coli* and *Saccharomyces cerevisiae*, through increases of transport mechanisms in the membrane of the target cell [115]. Mohammadi et al. (2015) also encapsulated *Zataria multiflora* essential oil in chitosan nanoparticles (average size of 125-175 nm) and reported that a controlled and sustained release of essential oil for 40 days can be accomplished, along with a superior antifungal performance in comparison with the un-encapsulated oil [118]. Moreover, films with 1.5% nanocomposite marjoram oil diminished the numbers of *E. coli, S. aureus,* and *Listeria monocytogenes* populations with respect to the control up to 4.52, 5.80, and 6.33 log, respectively [119]. Similarly, introduction of carvacrol nanoemulsions into modified chitosan have led to the development of a bioactive film active against gram negative pathogenic bacteria [120].

It is worth to mention that, in many cases, the vapor phase of essential oils exhibits strong inhibitive performance against pathogens, even more effective than direct application [121, 122]. For instance, Avila-Sosa et al. (2012) found that chitosan films incorporating cinnamon or Mexican oregano essential oils can inhibit fungi by vapor contact at lower oil concentrations than those required for amaranth and starch polymeric coatings [111].

II.3.3. Plasma-assisted fabrication of PSMs

Among fabrication techniques, cold plasma polymerization is a multipurpose approach that relatively fast and low-cost for fabricating coatings from a wide array of natural precursors, including those that do not usually polymerize by conventional methods, and do not require further chemical or physical processing (e.g. annealing, catalysts) [123]. From a processing point of view, many PSMs are compatible with plasma polymerization, which is in essence a chemical vapour deposition process enhanced by the catalytic activity of plasma, because they are highly volatile at room temperature, thus no external heat or carrier gas are required to deliver the precursor macromolecules to the fabrication zone.

Introducing of PSMs molecules, in vapour phase, into a highly reactive plasma field triggers a wide range of reactions including fragmentation, oligomerisation, rearrangement, and polymerization. The degree of dissociation is highly dependent on the amount of energy provided into the plasma system and the pressure in the chamber. The fragmentation is initiated by active electrons rather than thermal excitation or chemical reaction, creating a unique mixture of chemically-diverse species (e.g. unsaturated bonds, ions, neutrals, free radicals), which may not be reachable under other conditions [124]. It is believed that weakly ionised plasma and relatively low substrate temperature during deposition promote condensation and adsorption of non-excited species, which help to increase the proportion of non/partially-fragmented precursor molecules on the substrate [125]. The recombination of the reactive species and precursor molecules may lead to the formation of the organic thin layer (polymer) on the surface of a given substrate. Due to the diversity of functional groups and reactive species, the polymer can be formed in several ways, involving free-radicals induced-polymerization of fragments containing unsaturated carbon-carbon bonds, recombination fragment/recombination initiated by the plasma-generated and surface-attached reactive ions [126]. The formed polymer is often highly branched and highly cross-linked (amorphous), comprising large quantities of trapped free radicals in its structure [127].

A large number of species that exists in the discharge (e.g. ions, electrons, stable molecules, radicals and photons) can react with each other and with the forming chains through a range of interaction mechanisms, as seen in Figure II.3. The complexity of the process of PSMs plasma makes the evaluation of each specific reaction, along with the prediction of material properties very challenging. In some cases, few specific reactions can dominate the formation of the film, especially at low input power. Thus, it is rational to propose that films fabricated from PSMs using plasma under specific deposition conditions (e.g. specific input power, frequency, flow rate, temperature) could retain some/most of original functional groups of the original PSMs within

the bioactive three-dimensional solid film. In addition, the un-fragmented precursor molecules trapped within the polymer during the fabrication may elute over time, acting as a drug release coating, with the capacity to retard microbial attachment and biofilm development on the surface [128].

A number of attempts had been made to manufacture antibacterial surfaces based on plasma polymerization of essential oils, where the antibacterial performance is based only on the natural bioactivity of the polymerized surfaces, in absence of synthetic additives, inorganic nanoparticles or conventional antibiotics. Using this information, we strongly encourage the reader to further research this rapidly growing and highly-promising arena. Here, we highlight the successful manufacturing of antimicrobial coatings from different PSMs through cold plasma polymerization technique.

II.3.3.1. Terpinen-4-ol

Terpinen-4-ol is a monocyclic terpene alcohol that is an active component of tea tree oil. Terpinen-4-ol has demonstrated powerful antimicrobial and anti-inflammatory properties [129, 130]. Upon interaction with microorganisms, cyclic terpene hydrocarbons have shown to accumulate in the cell membrane. This disturbs membrane integrity, triggering an increased passive flux of protons through the membrane and dissipation of the proton motive force [131]. Bazaka et al. (2011) prepared plasma polymerized coatings derived from terpinen-4-ol at various input power levels, showing a considerable potential in minimizing bacterial attachment and metabolic activity of *S. aureus* and *P. aeruginosa*. Fabrication at low input power level of 10 W resulted in a partial retention of biologically-active groups of the original precursor, which led to a significant antimicrobial and antibiofouling activities of terpenol-derived coatings [132]. Confocal laser scanning microscopy evidently showed that around 90% of *S. aureus* cells retained on the films of 10 W substrata were non-viable, in comparison to that retained on the surface of 25 W films [133, 134]. However, when fabricated at higher input power (25 W), these films lost their biocidal activity, and promoted adhesion and proliferation of tested bacterial cells and biofilm development. In a recent report, the decrease in antibacterial activity with increasing RF energy was also observed in the plasma polymerization of polyterpenol films [135].

II.3.3.2. Carvone

Carvone is found in various essential oils, such as caraway, spearmint, and dill. This PSM has shown a variety of antiproliferative effects with regards to microbial cells, by the presence of a monoterpene group in its structure [136, 137]. In addition, carvone and its related compounds were shown to be potential chemopreventive agents, due to their ability to induce increased activity of detoxifying enzymes. The α,β-unsaturated ketone system in carvone is generally expected to be responsible for the high enzyme-inducing action [138]. Recently, Chan et al.

(2016) fabricated polymer coatings resultant from plasma polymerization of carvone [139]. At an input power of 10 W, carvone polymerized coatings demonstrated almost equal antimicrobial performance against both gram negative and gram positive bacteria (86% decrease in *E. coli* and 84% reduction in *S. aureus*), with no cytotoxic effect towards primary human endothelial cells. In addition, these coatings were smooth, highly cross-linked hydrocarbons, with low fraction of carboxyl, hydroxyl, and amine-amide functionalities. Although the carvone surfaces reduce bacterial adhesion, it was observed that some cells were damaged and died after attaching to the surface. The scanning electron microscope (SEM) images clearly exhibited membrane distortion, pore creation and membrane rupture of microorganisms attached on the surface of plasma polymers of carvone.

II.3.3.3. Eucalyptol

Eucalyptol, a major component of eucalyptus oil and a minor component of tea tree oil, is a saturated monoterpene known by a variety of synonyms, such as 1,8-cineole, 1,8-epoxy-p-menthane and cajeputol. This PSM has been demonstrated to retain strong biological activities, including anti-inflammatory, antifungal, antibiofilm and antiseptic properties toward a range of bacteria [140-143]. The retention of the natural bio-active groups of the 1,8-cineole oil was also achieved using plasma polymerization. Fabricated at 20 W, moderate hydrophobic coatings were achieved, with the ability to reduce the attachment of *E. coli* and *S. aureus* cells by 98% and 64%, respectively, compare to unmodified glass. In addition, the 1,8-cineole plasma films resisted biofilm formation after 5 days of incubation in the presence of bacterial cells. The polymer surface and any products that may be released from the film were also found to be not cytotoxic to mammalian cells [144]. In the same way, Mann and Fisher (2017) used a range of applied RF powers (P = 50–150 W) and $H_2O_{(v)}$ plasma-treatment during the plasma fabrication of 1,8-cineole polymers. The fabricated films retained some antimicrobial behaviour characteristic of the precursor, in addition to desired properties, such as being highly adherent to the substrate, conformal, and with smooth surfaces. The *in vitro* studies showed that *E. coli* were largely nonviable and unable to colonize the plasma-cineole surface over the 5 day biofilm development assay period. The biofilm coverage on these surfaces was significantly lower (<10%) than on glass control [145].

II.3.3.4. Geranium

Geranium (*Pelargonium graveolens*) oil produces a mixture of various components (more than 80) such as linalool, citronellol and geraniol [146]. Studies have revealed that geranium oil is able to combat pathogens, both gram-negative and gram-positive bacterial strains [73, 147]. More recently, geranium oil-derived coatings were also found to have the potential to reduce the microbial adhesion and biofilm formation of select human pathogens, such as *S. aureus*, *P.*

aeruginosa and *E. coli*. The input RF power, in particular, played a substantial role in controlling the surface bio-chemistry and extensively enhanced the biocidal activity of the fabricated coatings. Films deposited at 10 W proved a significant decrease in the number of cells, biovolume, and biofilm thickness. In contrast, there was no significant change in the bacterial colonisation between films fabricated at 50 W and an unmodified glass control. In addition to their biological activities, geranium polymer films showed several advantages, including low density, uniform coverage, good adhesion, and considerable physical stability [148, 149].

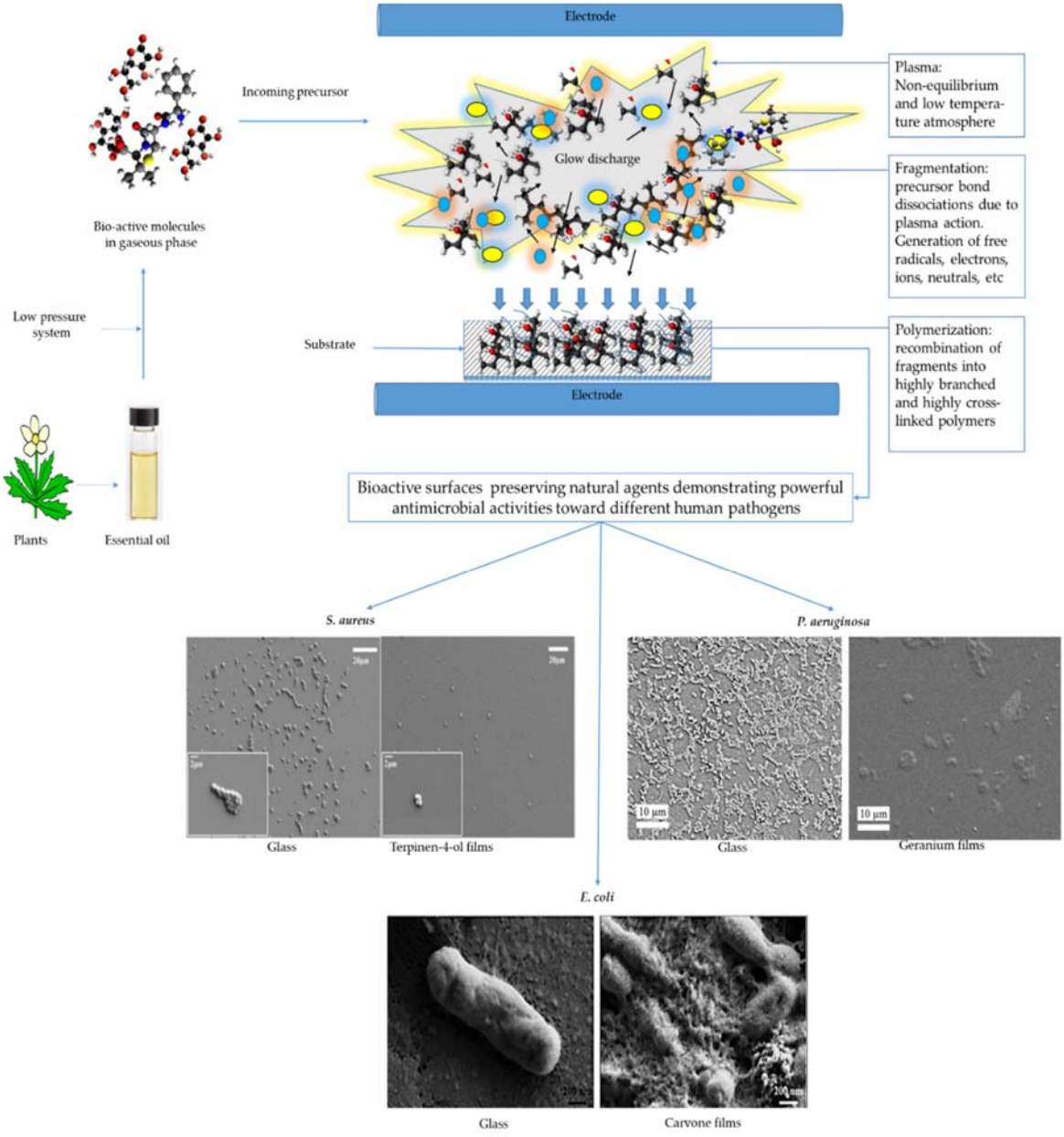

Figure II.3. Representative examples of plasma polymerization of plant secondary metabolises, where retention of the antimicrobial activity was achieved. As soon as a bioactive secondary plant

metabolite (or an essential oil) is placed under low pressures, the molecules gain sufficient kinetic energy to evaporate and begin independently moving towards the glow region within the deposition chamber. Exposure of the molecules to the highly reactive plasma initiates various chemical reactions such as bonds fragmentation, oligomerisation, and polymerization. At chosen plasma parameters, the process allows for the preservation of active functional groups of PSMs within the cross-linked solid polymeric films. Direct observations of SEM demonstrated powerful antimicrobial performance of geranium, terpenen-4-ol and carvony films in contact with different pathogens. The antimicrobial activities of these films included anti-biofouling effects and/or bactericidal actions (e.g. membrane distortion, pores creation and membrane damage). The SEM images are reproduced with permission from [132, 139, 148].

Despite the fact that the mechanism by which the deactivation process takes place remains not fully understood, the attractive antibacterial performance of PP-PSMs surfaces indicate that the original active chemistry of the oils are partially retained within the structure of fabricated films. Undeniably, plasma parameters are key factors that determine the extent of retention of biological functionality. The degree of precursor fragmentation is directly related to the amount of applied energy (RF power). For example, during the polymerization of geranium oil and terpinen-4-ol , a slight increase in the input power resulted in failure to preserve the desired functional groups within the polymer. One reason for this loss of the bactericidal activity could be the complete dissociation of the precursor functionalities upon plasma exposure. Furthermore, these polymerized films demonstrated a wide range of functional groups in their structure, such as primarily methyl/methylene functionalities as well as hydroxyl, alkene and carbonyl groups. The hydroxyl group particularly is broadly accepted to be an antimicrobial agent of polymer surfaces. It was previously reported that *S. aureus* cells do not preferentially attach to polymers comprising –OH functionality than those bearing carboxylic and methyl groups [150]. However, other surface parameters should be carefully considered during plasma fabrication. It is well known that surface chemistry, hydrophobicity, free energy, and architecture of polymer films have the potential to significantly influence the final antibacterial outcome. The synergistic effects of these parameters may determine the inhibition of bacterial attachment and proliferation.

II.3.4. Properties of PSM-derived polymers

To be a successful polymeric antibacterial coating satisfying requirements for biomedical applications, the material should possess a range of specific biological, physical and chemical properties. Films fabricated from PSMs display a wide range of desired properties, including optical transparency, moderate hydrophilicity, relatively high degradation temperature, low post-annealing retention, and good biocompatibility, forming simple, useful, and versatile bioactive

coatings. Hence, a brief description of some important physicochemical characteristics of PP-PSMs fabricated at low input power (below 100 W) is provided below.

As a general trend observed for PP-PSMs, polymers deposited at higher input power are typically less susceptible to mechanical deformation. This trend is owing to an increase in the degree of cross-linking correlated with higher input power, and hence films are likely to be more stable and less susceptible to wear [151]. Highly cross-linked polymers are expressively more stiff and dense compared to conventional polymers (amorphous or crystalline arrangements). This is related to the vibrational movement of the carbon backbone of the polymeric structure that is constrained by the presence of a multiple covalent bonds between polymer chains [152].

The topographical features of PP-PSMs fabricated at suitable parameters have been shown to be uniform, pinhole free, with films being highly-adherent to the substrate [149, 153-158]. The uniformity indicates that polymerization reactions occurred on the surface of the substrate in preference to the gas phase. Moreover, ultra-smooth surfaces (with an average roughness of less than 1 nm) were attained for plasma polymerization of various PSMs, which particularly is a significant factor that may influence the initial microbial adhesion [159, 160]. It is worth to mention that the properties of the surface of plasma polymerized films are highly susceptible to growth conditions, especially the input power, where more energetic ions can cause more surface bombardment and etching. Furthermore, the chosen precursor plays an important role in the overall surface properties, since it to a degree defines the chemical functionalities and determines the quantities of free radicals in the plasma system [161, 162].

A large number of plasma polymers developed from PSMs were reported to have favourable optical properties. Although optical properties were affected by processing parameters during film deposition, PP-PSMs were found to be optically transparent in the visible region and have high absorption in the infrared region. The refractive index and extinction coefficient were in the range of 1.5 and 0.001 (at 500 nm), respectively [163, 164]. In addition, PSMs-derived polymer materials have optical energy gap (E_g) values in the insulating and semiconducting region. For example, films fabricated from terpinen-4-ol, linalool, γ-terpinene and geranium have E_g= 2.5, 2.9, 3.0 and 3.6 eV, respectively [148, 160, 165]. It is important to note that the optical properties of plasma films are characteristically dependent on the structure of the *p*-conjugated chains in both the ground and the excited stats, as well as on the inter-chain orientation [166].

In general, PP-PSMs were moderately hydrophilic, with values of contact angles ranging from ~50° to 80°. The wetting characteristics were defined largely by plasma conditions and the chemistry of the chosen precursor. For example, improved hydrophobicity of the surface was observed for films fabricated from γ-terpinene with increasing the deposition RF power, from

61.0° (10 W) to 80.7° (75 W). This polymer revealed a strong electron donor and a negligible electron acceptor behaviour [167]. The range of contact angle values of plasma polymer are well-suited for biological uses, since they enable and promote adhesion of various cell types [148].

Given their potential application as an antibacterial coating for implants, the cytocompatibility of PP-PSMs was examined for several types of mammalian cells. A study that tested the biocompatibility of coatings fabricated from various oils (e.g. limonene, tea tree, lavender, and eucalyptus) at different deposition power showed minimum toxic effects. After being implanted in mice for 3 days, 14 days and 28 days, all PP-PSM films were demonstrated to be biocompatible. While in most cases, these coatings did not produce an unwanted host or material response, in a number of mice sinus formation was observed, however it was deemed not significant [168]. The biocompatibility of polymer films is a property that should be addressed carefully for protective coatings in medical applications, in particular for implantable devices, since the film surface directly interfaces with various bio-components including blood, proteins, cells and tissue growth. Hence, non-biocompatible coatings may lead to failure, toxic responses, abnormal cell/tissue responses, and device degradation.

It should be noted that PP-PSMs have shown some limitations. For example, they are generally insoluble in organic-solvents owing to their high degree of crosslinking. This feature, in particular, greatly complicates the characterization of the polymers [126]. It was also observed that PP-PSMs are highly susceptible to changes brought by the chemical composition of the medium (e.g. the aqueous solution and body fluid) that may affect their operation in some applications [169].

II.4. Challenges in the fabrication of PSM-derived polymers

In the scientific and manufacturing field, replication or reproduction of the consistent systematic results is the key to success [170]. A major issue of plasma techniques is the constancy of the result, particularly across different plasma systems due to differences in processing parameters (e.g. power, pressure, temperature, flow rate and tube geometry). For example, changes in the design of plasma equipment can affect the dynamics of the flow of vapors through the system, and the profile of the plasma discharge zone, which could potentially alter the nature, homogeneity and density of the gas phase species inside the reactor. Indeed, this problem becomes more obvious during the fabrication of functional coatings from PSMs, where retention of certain chemical moieties is essential [171]. To minimize the variation of films produced across different plasma systems, scaling factor route can be applied that takes into account both the actual energy consumed in the active plasma field, and the differences in the geometry of the utilized reactors [172].

Another concern comes from the varying properties of the renewable precursor. It is well documented that essential oil composition is very complex and depends on multiple interacting factors. In addition, De Masi et al. (2006) reported that chemical compounds of essential oils were found extremely variable in the various cultivars/genotypes of the same plant species and they are not necessarily correlated with genetic relationships [173]. At this regard, the oil quality and biological activity can be affected also by the conditions of storage, e.g. temperature [174]. The potential to obtain biopolymer films with consistent properties regardless of base material source, method or time of harvest is important for successful integration into the industrialised process.

It is generally accepted that the chemical composition of essential oils varies by plant health, growth stage, climate, edaphic factors, and harvest time. On the other hand, the degradation kinetics of these oils due to external factors (e.g. temperature, light, and atmospheric oxygen exposure, presence of impurities) should be thoroughly taken into account [175]. For example, pure cinnamaldehyde was reported to decompose to benzaldehyde at temperatures approaching 60 °C. But, once it combined with eugenol or cinnamon leaf oil, cinnamaldehyde remained stable at 200 °C [176]. The molecular structures of natural oil have, in particular, a substantial effect on the degree of degradation. Compounds rich in allylic hydrogen atoms could be most potential targets for autoxidation, where hydrogen atom abstraction is giving rise to resonance-stabilized radicals that highly preferable owing to lower activation energy [177]. Furthermore, essential oil components are generally known to easily convert into each other (through processes such as isomerization, oxidation, cyclization, or dehydrogenation reactions), since their structural relationship within the same chemical group [175, 177].

It is important to mention that serval essential oils (e.g. tea tree, lavender, and terpenene-4-ol) have shown some irritation and allergies in users (via inhalation or direct contact) [178-180]. The allergic reactions typically arise from certain components such as benzyl alcohol, cinnamyl alcohol, iso-eugenol, eugenol, hydroxycitronellal, geraniol and various others constituents [181-183]. However, sensitive symptoms due to essential oils can range from relatively minor incidences of irritation and sensitisation, to contact dermatitis and the most serious anaphylactic reaction, thus should be well considered [184, 185].

As mentioned previously in this article, typical plasma polymerization of PSMs (continuous mode) yields the fragmentation of large quantity of precursor molecules. The random recombination of fragments, radicals and atoms renders the chemical structure and configuration completely irregular. In fact, even when fabrication coatings under low energy conditions, an irregular structure dominates and the density of the wanted functional group remains low. Pulsed-plasma polymerization can address this issue. This technique offers a sequence of on-periods (a few μs-long period during which fragmentation takes place) and off-periods (μs to ms-long

periods during which recombination and polymerization occurs), where the resultant polymer should consist of more chemically regular structures than those of the continuous mode [186]. The idea is to further reduce the degree of dissociation/fragmentation of the precursor molecules, and hence the off-period reactions contributing more non-fragmented functionalities into the formed polymer. To date, the pulsed-plasma polymerization has not been used for the synthesis of antibacterial surfaces from PSMs. We highly encourage researchers to explore and expand the usage of pulsed-plasma method, where the optimization of the desired functionality will essentially include the increasing/decreasing the off-period in pulsed polymerization.

II.5. Conclusion

A better understanding of the way to preserve/retain the bioactivity of essential oils within a thin film is critical for the development of a wide range of bactericidal coatings suitable for medical devices. Aforementioned polymer materials that derived from renewable resources present a promising approach toward producing antimicrobial and biocompatible materials and tissue contact coatings. However, information on the long-term performance of plasma polymerized PSMs thin films requires further exploration. Also, although a small number of systematic studies showed promising antimicrobial activity of encapsulating essential oils, further research in this direction is warranted.

References

1. Sanborn, L.W.R., *The relation of surface contamination to the transmission of disease.* American Journal of Public Health and the Nations Health, 1963. **53**(8): p. 1278-1283.
2. Dancer, S.J., *Importance of the environment in meticillin-resistant Staphylococcus aureus acquisition: the case for hospital cleaning.* The Lancet infectious diseases, 2008. **8**(2): p. 101-113.
3. Knetsch, M.L.W. and L.H. Koole, *New Strategies in the Development of Antimicrobial Coatings: The Example of Increasing Usage of Silver and Silver Nanoparticles.* Polymers, 2011. **3**(4): p. 340-366.
4. Wu, S., et al., *Plasma-modified biomaterials for self-antimicrobial applications.* ACS Appl Mater Interfaces, 2011. **3**(8): p. 2851-60.
5. Edmiston Jr, C.E., et al., *Clinical and microbiological aspects of biofilm-associated surgical site infections*, in *Biofilm-Based Healthcare-Associated Infections*. 2015, Springer. p. 47-67.

6. Veerachamy, S., et al., *Bacterial adherence and biofilm formation on medical implants: A review.* Proceedings of the Institution of Mechanical Engineers, Part H: Journal of Engineering in Medicine, 2014. **228**(10): p. 1083-1099.
7. Batoni, G., G. Maisetta, and S. Esin, *Antimicrobial peptides and their interaction with biofilms of medically relevant bacteria.* Biochimica et Biophysica Acta (BBA)-Biomembranes, 2016. **1858**(5): p. 1044-1060.
8. Joseph, R., et al., *Cationic Pillararenes Potently Inhibit Biofilm Formation without Affecting Bacterial Growth and Viability.* Journal of the American Chemical Society, 2016. **138**(3): p. 754-757.
9. Mingeot-Leclercq, M.-P. and J.-L. Décout, *Bacterial lipid membranes as promising targets to fight antimicrobial resistance, molecular foundations and illustration through the renewal of aminoglycoside antibiotics and emergence of amphiphilic aminoglycosides.* MedChemComm, 2016. **7**(4): p. 586-611.
10. Chopra, I. and M. Roberts, *Tetracycline antibiotics: mode of action, applications, molecular biology, and epidemiology of bacterial resistance.* Microbiology and molecular biology reviews, 2001. **65**(2): p. 232-260.
11. Woon, S.-A. and D. Fisher, *Antimicrobial agents–optimising the ecological balance.* BMC medicine, 2016. **14**(1): p. 114.
12. Mathur, S. and R. Singh, *Antibiotic resistance in food lactic acid bacteria—a review.* International journal of food microbiology, 2005. **105**(3): p. 281-295.
13. *Antibiotic resistant bacteria*, D.o.H.H. Services, Editor. 2015, State Government of Victoria, : Australia.
14. *Antibiotic resistant bacteria.* 2016; Available from: https://www.betterhealth.vic.gov.au/health/conditionsandtreatments/antibiotic-resistant-bacteria?viewAsPdf=true.
15. Hasan, J., R.J. Crawford, and E.P. Ivanova, *Antibacterial surfaces: the quest for a new generation of biomaterials.* Trends in biotechnology, 2013. **31**(5): p. 295-304.
16. O'Bryan, C.A., et al., *Potential of plant essential oils and their components in animal agriculture–in vitro studies on antibacterial mode of action.* Frontiers in veterinary science, 2015. **2**: p. 35.
17. Nazzaro, F., et al., *Effect of essential oils on pathogenic bacteria.* Pharmaceuticals, 2013. **6**(12): p. 1451-1474.
18. Murbach Teles Andrade, B.F., et al., *Antimicrobial activity of essential oils.* Journal of Essential Oil Research, 2014. **26**(1): p. 34-40.

19. Altenstetter, C. *Global and local dynamics: The regulation of medical technologies in the European Union, Japan and the United states*. in *Third Biennial Conference 'Regulation in the age of Crisis', Dublin, Ireland*. 2010.
20. Méndez-Vilas, A. and J. Díaz, *Microscopy: Science, technology, applications and education*. 2010: Formatex Research Center.
21. Hetrick, E.M. and M.H. Schoenfisch, *Reducing implant-related infections: active release strategies.* Chemical Society Reviews, 2006. **35**(9): p. 780-789.
22. Chandki, R., P. Banthia, and R. Banthia, *Biofilms: a microbial home.* Journal of Indian Society of Periodontology, 2011. **15**(2): p. 111.
23. de la Fuente-Núñez, C., et al., *Bacterial biofilm development as a multicellular adaptation: antibiotic resistance and new therapeutic strategies.* Current Opinion in Microbiology, 2013. **16**(5): p. 580-589.
24. Chen, Y., et al., *Nanoscale cell wall deformation impacts long-range bacterial adhesion forces on surfaces.* Applied and environmental microbiology, 2014. **80**(2): p. 637-643.
25. Scheuerman, T.R., A.K. Camper, and M.A. Hamilton, *Effects of substratum topography on bacterial adhesion.* Journal of colloid and interface science, 1998. **208**(1): p. 23-33.
26. Donlan, R.M., *Biofilms: microbial life on surfaces.* Emerg Infect Dis, 2002. **8**(9).
27. Crawford, R.J. and E.P. Ivanova, *Superhydrophobic surfaces*. 2015, Elsevier.
28. Boland, T., R.A. Latour, and F.J. Stutzenberger, *Molecular basis of bacterial adhesion*, in *Handbook of Bacterial Adhesion*. 2000, Springer. p. 29-41.
29. Basak, S., et al., *Biofilms: A Challenge to Medical Fraternity in Infection Control.* INFECTION CONTROL, 2013: p. 57.
30. Anselme, K., et al., *The interaction of cells and bacteria with surfaces structured at the nanometre scale.* Acta Biomaterialia, 2010. **6**(10): p. 3824-3846.
31. Epstein, E.A., M.A. Reizian, and M.R. Chapman, *Spatial clustering of the curlin secretion lipoprotein requires curli fiber assembly.* Journal of bacteriology, 2009. **191**(2): p. 608-615.
32. Fletcher, M. and D.C. Savage, *Bacterial adhesion: mechanisms and physiological significance*. 2013: Springer Science & Business Media.
33. Moss, J.A., et al., *Stability and change in estuarine biofilm bacterial community diversity.* Applied and environmental microbiology, 2006. **72**(9): p. 5679-5688.
34. Flemming, H.-C. and J. Wingender, *The biofilm matrix.* Nature Reviews Microbiology, 2010. **8**(9): p. 623-633.
35. Douglas, L.J., *Candida biofilms and their role in infection.* Trends in microbiology, 2003. **11**(1): p. 30-36.

36. Ma, L., et al., *Assembly and development of the Pseudomonas aeruginosa biofilm matrix.* PLoS Pathog, 2009. **5**(3): p. e1000354.
37. Karimi, A., et al., *Interplay of physical mechanisms and biofilm processes: review of microfluidic methods.* Lab on a Chip, 2015. **15**(1): p. 23-42.
38. Sharafat, I., et al., *Interactive Effect of Trivalent Iron on Activated Sludge Digestion and Biofilm Structure in Attached Growth Reactor of Waste Tyre Rubber.* Environmental Technology, 2017(just-accepted): p. 1-37.
39. Hassan, A., et al., *Evaluation of different detection methods of biofilm formation in the clinical isolates.* Brazilian Journal of Infectious Diseases, 2011. **15**(4): p. 305-311.
40. Nguyen, S.H., et al., *Natural Antibacterial Surfaces*, in *Antibacterial Surfaces*. 2015, Springer. p. 9-26.
41. Jackson, D.W., et al., *Biofilm formation and dispersal under the influence of the global regulator CsrA of Escherichia coli.* Journal of bacteriology, 2002. **184**(1): p. 290-301.
42. Socransky, S.S. and A.D. Haffajee, *Dental biofilms: difficult therapeutic targets.* Periodontology 2000, 2002. **28**(1): p. 12-55.
43. Donlan, R.M., *Biofilm formation: a clinically relevant microbiological process.* Clinical Infectious Diseases, 2001. **33**(8): p. 1387-1392.
44. Derlon, N., et al., *Growth limiting conditions and denitrification govern extent and frequency of volume detachment of biofilms.* Chemical Engineering Journal, 2013. **218**: p. 368-375.
45. Barraud, N., et al., *Involvement of nitric oxide in biofilm dispersal of Pseudomonas aeruginosa.* Journal of bacteriology, 2006. **188**(21): p. 7344-7353.
46. Hall-Stoodley, L., J.W. Costerton, and P. Stoodley, *Bacterial biofilms: from the natural environment to infectious diseases.* Nature reviews microbiology, 2004. **2**(2): p. 95-108.
47. Alexander, S.-A. and C.H. Schiesser, *Heteroorganic molecules and bacterial biofilms: Controlling biodeterioration of cultural heritage.* Organic Chemistry, 2017(part ii): p. 180-222.
48. Fish, K.E., A.M. Osborn, and J. Boxall, *Characterising and understanding the impact of microbial biofilms and the extracellular polymeric substance (EPS) matrix in drinking water distribution systems.* Environmental science: water research & technology, 2016. **2**(4): p. 614-630.
49. Kaplan, J.á., *Biofilm dispersal: mechanisms, clinical implications, and potential therapeutic uses.* Journal of dental research, 2010. **89**(3): p. 205-218.
50. Parsek, M.R., *Controlling the connections of cells to the biofilm matrix.* Journal of bacteriology, 2016. **198**(1): p. 12-14.

51. Rasamiravaka, T., et al., *The formation of biofilms by Pseudomonas aeruginosa: a review of the natural and synthetic compounds interfering with control mechanisms.* BioMed research international, 2015. **2015**.
52. Bryers, J.D., *Medical biofilms.* Biotechnology and bioengineering, 2008. **100**(1): p. 1-18.
53. *Device-Related Infections.* 2006; Available from: http://www.infectioncontroltoday.com/articles/2006/11/device-related-infections.aspx.
54. Pradeep, K.S., H. Easwer, and N.A. Maya, *Multiple drug resistant bacterial biofilms on implanted catheters-a reservoir of infection.* The Journal of the Association of Physicians of India, 2013. **61**(10): p. 702-707.
55. Klevens, R.M., et al., *The impact of antimicrobial-resistant, health care–associated infections on mortality in the United States.* Clinical infectious diseases, 2008. **47**(7): p. 927-930.
56. Coenye, T., et al., *Prevention of Candida albicans biofilm formation.* The Open Mycology Journal, 2011. **5**(1).
57. Deorukhkar, S.C. and S. Saini, *Why Candida Species have Emerged as Important Nosocomial Pathogens?* Int. J. Curr. Microbiol. App. Sci, 2016. **5**(1): p. 533-545.
58. Sanclement, J.A., et al., *Bacterial biofilms in surgical specimens of patients with chronic rhinosinusitis.* The Laryngoscope, 2005. **115**(4): p. 578-582.
59. Ramage, G., J.P. Martínez, and J.L. López-Ribot, *Candida biofilms on implanted biomaterials: a clinically significant problem.* FEMS Yeast research, 2006. **6**(7): p. 979-986.
60. Jabra-Rizk, M.A., et al., *Candida albicans Pathogenesis: Fitting within the Host-Microbe Damage Response Framework.* Infection and Immunity, 2016. **84**(10): p. 2724-2739.
61. Alhede, M., et al., *Phenotypes of non-attached Pseudomonas aeruginosa aggregates resemble surface attached biofilm.* PloS one, 2011. **6**(11): p. e27943.
62. Wagner, V.E. and B.H. Iglewski, *P. aeruginosa biofilms in CF infection.* Clinical reviews in allergy & immunology, 2008. **35**(3): p. 124-134.
63. Kateryna, B., et al., *Plasma-potentiated small molecules—possible alternative to antibiotics?* Nano Futures, 2017. **1**(2): p. 025002.
64. Silva, N. and A. Fernandes Júnior, *Biological properties of medicinal plants: a review of their antimicrobial activity.* Journal of venomous animals and toxins including tropical diseases, 2010. **16**(3): p. 402-413.
65. Inès Hammami, M.A.T.a.A.R., *Chemical compositions, antibacterial and antioxidant activities of essential oil and various extracts of Geranium sanguineum L. flowers.* Scholars Research Library, 2011: p. 135-144.

66. Hui, L., et al., *Chemical composition of lavender essential oil and its antioxidant activity and inhibition against rhinitis-related bacteria.* African Journal of Microbiology Research, 2010. **4**(4): p. 309-313.
67. Glinel, K., et al., *Antibacterial surfaces developed from bio-inspired approaches.* Acta biomaterialia, 2012. **8**(5): p. 1670-1684.
68. Hierro, I., et al., *Action of different monoterpenic compounds against Anisakis simplex sl L3 larvae.* Phytomedicine, 2004. **11**(1): p. 77-82.
69. Bigos, M., et al., *Antimicrobial activity of geranium oil against clinical strains of Staphylococcus aureus.* Molecules, 2012. **17**(9): p. 10276-10291.
70. Friedman, M., et al., *Antibacterial activities of plant essential oils and their components against Escherichia coli O157: H7 and Salmonella enterica in apple juice.* Journal of agricultural and food chemistry, 2004. **52**(19): p. 6042-6048.
71. Tisserand, R. and R. Young, *Essential oil safety: a guide for health care professionals.* 2013: Elsevier Health Sciences.
72. Sun, L.-m., C.-l. Zhang, and P. Li, *Characterization, antibiofilm, and mechanism of action of novel PEG-stabilized lipid nanoparticles loaded with terpinen-4-ol.* Journal of agricultural and food chemistry, 2012. **60**(24): p. 6150-6156.
73. Prabuseenivasan, S., M. Jayakumar, and S. Ignacimuthu, *In vitro antibacterial activity of some plant essential oils.* BMC complementary and alternative medicine, 2006. **6**(1): p. 39.
74. Faid, M., et al., *Almond paste: physicochemical and microbiological characterization and preservation with sorbic acid and cinnamon.* Journal of Food Protection®, 1995. **58**(5): p. 547-550.
75. Maruzzella, J.C. and N.A. Sicurella, *Antibacterial activity of essential oil vapors.* Journal of Pharmaceutical Sciences, 1960. **49**(11): p. 692-694.
76. Maruzzella, J.C., J.S. Chiaramonte, and M.M. Garofalo, *Effects of vapors of aromatic chemicals on fungi.* Journal of Pharmaceutical Sciences, 1961. **50**(8): p. 665-668.
77. Akthar, M.S., B. Degaga, and T. Azam, *Antimicrobial activity of essential oils extracted from medicinal plants against the pathogenic microorganisms: A review.* Issues in Biological Sciences and Pharmaceutical Research, 2014. **2**(1): p. 1-7.
78. Calo, J.R., et al., *Essential oils as antimicrobials in food systems – A review.* Food Control, 2015. **54**(Supplement C): p. 111-119.
79. Eze, U.A., *"In vitro Antimicrobial Activity of Essential Oils from the Lamiaceae and Rutaceae Plant Families Against β*

-Lactamse-Producing Clinical Isolates Of Moraxella Catarrhalis". EC Pharmaceutical Seience 2016. **2.3**: p. 325-337.

80. Burt, S., *Essential oils: their antibacterial properties and potential applications in foods—a review.* International Journal of Food Microbiology, 2004. **94**(3): p. 223-253.
81. Devi, K.P., et al., *Eugenol (an essential oil of clove) acts as an antibacterial agent against Salmonella typhi by disrupting the cellular membrane.* Journal of ethnopharmacology, 2010. **130**(1): p. 107-115.
82. Ultee, A., E. Kets, and E. Smid, *Mechanisms of action of carvacrol on the food-borne pathogen Bacillus cereus.* Applied and environmental microbiology, 1999. **65**(10): p. 4606-4610.
83. Swamy, M.K., M.S. Akhtar, and U.R. Sinniah, *Antimicrobial properties of plant essential oils against human pathogens and their mode of action: An updated review.* Evidence-Based Complementary and Alternative Medicine, 2016. **2016**.
84. Ultee, A. and E.J. Smid, *Influence of carvacrol on growth and toxin production by Bacillus cereus.* International Journal of Food Microbiology, 2001. **64**(3): p. 373-378.
85. Raut, J.S. and S.M. Karuppayil, *A status review on the medicinal properties of essential oils.* Industrial Crops and Products, 2014. **62**(Supplement C): p. 250-264.
86. Gustafson, J., et al., *Effects of tea tree oil on Escherichia coli.* Letters in applied microbiology, 1998. **26**(3): p. 194-198.
87. Szabó, M.Á., et al., *Inhibition of quorum-sensing signals by essential oils.* Phytotherapy research, 2010. **24**(5): p. 782-786.
88. Christaki, E., et al., *Aromatic plants as a source of bioactive compounds.* Agriculture, 2012. **2**(3): p. 228-243.
89. Ben Arfa, A., et al., *Antimicrobial activity of carvacrol related to its chemical structure.* Letters in applied microbiology, 2006. **43**(2): p. 149-154.
90. Bassolé, I.H.N. and H.R. Juliani, *Essential oils in combination and their antimicrobial properties.* Molecules, 2012. **17**(4): p. 3989-4006.
91. Trombetta, D., et al., *Mechanisms of antibacterial action of three monoterpenes.* Antimicrobial agents and chemotherapy, 2005. **49**(6): p. 2474-2478.
92. Wang, W., et al., *Antibacterial activity and anticancer activity of Rosmarinus officinalis L. essential oil compared to that of its main components.* Molecules, 2012. **17**(3): p. 2704-2713.
93. Ćavar, S., et al., *Chemical composition and antioxidant and antimicrobial activity of essential oil of Artemisia annua L. from Bosnia.* Industrial Crops and Products, 2012. **37**(1): p. 479-485.
94. STOICA, P., et al., *Fabrication, characterization and bioevaluation of novel antimicrobial composites based on polycaprolactone, chitosan and essential oils.* Romanian Biotechnological Letters, 2015. **20**(3): p. 10521.

95. Balat, M. and M. Balat, *Political, economic and environmental impacts of biomass-based hydrogen.* International Journal of Hydrogen Energy, 2009. **34**(9): p. 3589-3603.
96. Balzani, V. and N. Armaroli, *Energy for a sustainable world: from the oil age to a sun-powered future*. 2010: John Wiley & Sons.
97. Winnacker, M. and B. Rieger, *Recent progress in sustainable polymers obtained from cyclic terpenes: synthesis, properties, and application potential.* ChemSusChem, 2015. **8**(15): p. 2455-2471.
98. Saggiorato, A.G., et al., *Antifungal Activity of Basil Essential Oil (Ocimum basilicum L.): Evaluation In Vitro and on an Italian-type Sausage Surface.* Food and Bioprocess Technology, 2012. **5**(1): p. 378-384.
99. Teramoto, Y. and Y. Nishio, *Cellulose diacetate-graft-poly (lactic acid) s: synthesis of wide-ranging compositions and their thermal and mechanical properties.* Polymer, 2003. **44**(9): p. 2701-2709.
100. Arrieta, M.P., et al., *Ternary PLA–PHB–Limonene blends intended for biodegradable food packaging applications.* European Polymer Journal, 2014. **50**: p. 255-270.
101. Robertson, M.L., J.M. Paxton, and M.A. Hillmyer, *Tough Blends of Polylactide and Castor Oil.* ACS Applied Materials & Interfaces, 2011. **3**(9): p. 3402-3410.
102. Morschbacker, A., *Bio-Ethanol Based Ethylene.* Polymer Reviews, 2009. **49**(2): p. 79-84.
103. Mathers, R.T., et al., *Functional Hyperbranched Polymers Using Ring-Opening Metathesis Polymerization of Dicyclopentadiene with Monoterpenes.* Macromolecules, 2009. **42**(5): p. 1512-1518.
104. Quilter, H.C., et al., *Polymerisation of a terpene-derived lactone: a bio-based alternative to ε-caprolactone.* Polymer Chemistry, 2017. **8**(5): p. 833-837.
105. Gandini, A., *The irruption of polymers from renewable resources on the scene of macromolecular science and technology.* Green Chemistry, 2011. **13**(5): p. 1061-1083.
106. Wilbon, P.A., F. Chu, and C. Tang, *Progress in renewable polymers from natural terpenes, terpenoids, and rosin.* Macromolecular rapid communications, 2013. **34**(1): p. 8-37.
107. Shit, S.C. and P.M. Shah, *Edible polymers: challenges and opportunities.* Journal of Polymers, 2014. **2014**.
108. Modjinou, T., et al., *Antibacterial Networks Based on Isosorbide and Linalool by Photoinitiated Process.* ACS Sustainable Chemistry & Engineering, 2015. **3**(6): p. 1094-1100.
109. Chen, Y., et al., *Amphipathic antibacterial agents using cationic methacrylic polymers with natural rosin as pendant group.* RSC Advances, 2012. **2**(27): p. 10275-10282.

110. Wen, P., et al., *Fabrication of electrospun polylactic acid nanofilm incorporating cinnamon essential oil/β-cyclodextrin inclusion complex for antimicrobial packaging.* Food Chemistry, 2016. **196**: p. 996-1004.
111. Avila-Sosa, R., et al., *Antifungal activity by vapor contact of essential oils added to amaranth, chitosan, or starch edible films.* International Journal of Food Microbiology, 2012. **153**(1): p. 66-72.
112. Jouki, M., et al., *Quince seed mucilage films incorporated with oregano essential oil: Physical, thermal, barrier, antioxidant and antibacterial properties.* Food Hydrocolloids, 2014. **36**: p. 9-19.
113. Ruiz-Navajas, Y., et al., *In vitro antibacterial and antioxidant properties of chitosan edible films incorporated with Thymus moroderi or Thymus piperella essential oils.* Food Control, 2013. **30**(2): p. 386-392.
114. Quirós-Sauceda, A.E., et al., *Edible coatings as encapsulating matrices for bioactive compounds: a review.* Journal of food science and technology, 2014. **51**(9): p. 1674-1685.
115. Donsì, F., et al., *Nanoencapsulation of essential oils to enhance their antimicrobial activity in foods.* LWT - Food Science and Technology, 2011. **44**(9): p. 1908-1914.
116. Sessa, M., G. Ferrari, and F. Donsì, *Novel edible coating containing essential oil nanoemulsions to prolong the shelf life of vegetable products.* Chem. Eng. Trans, 2015. **43**: p. 55-60.
117. Peng, Y. and Y. Li, *Combined effects of two kinds of essential oils on physical, mechanical and structural properties of chitosan films.* Food Hydrocolloids, 2014. **36**: p. 287-293.
118. Mohammadi, A., M. Hashemi, and S.M. Hosseini, *Nanoencapsulation of Zataria multiflora essential oil preparation and characterization with enhanced antifungal activity for controlling Botrytis cinerea, the causal agent of gray mould disease.* Innovative Food Science & Emerging Technologies, 2015. **28**: p. 73-80.
119. Alboofetileh, M., et al., *Antimicrobial activity of alginate/clay nanocomposite films enriched with essential oils against three common foodborne pathogens.* Food Control, 2014. **36**(1): p. 1-7.
120. Severino, R., et al., *Antimicrobial effects of modified chitosan based coating containing nanoemulsion of essential oils, modified atmosphere packaging and gamma irradiation against Escherichia coli O157:H7 and Salmonella Typhimurium on green beans.* Food Control, 2015. **50**: p. 215-222.
121. Goñi, P., et al., *Antimicrobial activity in the vapour phase of a combination of cinnamon and clove essential oils.* Food Chemistry, 2009. **116**(4): p. 982-989.

122. López, P., et al., *Solid- and Vapor-Phase Antimicrobial Activities of Six Essential Oils: Susceptibility of Selected Foodborne Bacterial and Fungal Strains.* Journal of Agricultural and Food Chemistry, 2005. **53**(17): p. 6939-6946.
123. Jacob, M.V., et al. *RF plasma polymerised thin films from natural resources*. in *International Journal of Modern Physics: Conference Series*. 2014. World Scientific.
124. Kumar, A., et al., *Tailoring terpenoid plasma polymer properties by controlling the substrate temperature during PECVD.* Journal of Applied Polymer Science.
125. Lopez, G.P. and B.D. Ratner, *Substrate temperature effects on film chemistry in plasma deposition of organics. 1. Nonpolymerizable precursors.* Langmuir, 1991. **7**(4): p. 766-773.
126. Shi, F.F., *Recent advances in polymer thin films prepared by plasma polymerization synthesis, structural characterization, properties and applications.* Surface and Coatings Technology, 1996. **82**(1): p. 1-15.
127. Bazaka, K., et al., *Efficient surface modification of biomaterial to prevent biofilm formation and the attachment of microorganisms.* Applied microbiology and biotechnology, 2012. **95**(2): p. 299-311.
128. Bazaka, K., et al., *Anti-bacterial surfaces: natural agents, mechanisms of action, and plasma surface modification.* RSC Advances, 2015. **5**(60): p. 48739-48759.
129. Brady, A., et al., *In vitro activity of tea-tree oil against clinical skin isolates of meticillin-resistant and-sensitive Staphylococcus aureus and coagulase-negative staphylococci growing planktonically and as biofilms.* Journal of medical microbiology, 2006. **55**(10): p. 1375-1380.
130. Mondello, F., et al., *In vitro and in vivo activity of tea tree oil against azole-susceptible and-resistant human pathogenic yeasts.* Journal of Antimicrobial Chemotherapy, 2003. **51**(5): p. 1223-1229.
131. Carson, C.F., B.J. Mee, and T.V. Riley, *Mechanism of action of Melaleuca alternifolia (tea tree) oil on Staphylococcus aureus determined by time-kill, lysis, leakage, and salt tolerance assays and electron microscopy.* Antimicrobial agents and chemotherapy, 2002. **46**(6): p. 1914-1920.
132. Bazaka, K., et al., *The effect of polyterpenol thin film surfaces on bacterial viability and adhesion.* Polymers, 2011. **3**(1): p. 388-404.
133. Bazaka, K., et al., *Effect of plasma-enhanced chemical vapour deposition on the retention of antibacterial activity of terpinen-4-ol.* Biomacromolecules, 2010. **11**(8): p. 2016.
134. Bazaka, K., M.V. Jacob, and E.P. Ivanova. *A study of a retention of antimicrobial activity by plasma polymerized terpinen-4-ol thin films*. in *Materials Science Forum*. 2010. Trans Tech Publ.

135. Bayram, O. and O. Simsek, *Investigation of the effect of RF energy on optical, morphological, chemical and antibacterial properties of PolyTerpenol thin films obtained by RF-PECVD technique.* Journal of Materials Science: Materials in Electronics, 2018. **29**(8): p. 6586-6593.
136. Aggarwal, K.K., et al., *Antimicrobial activity profiles of the two enantiomers of limonene and carvone isolated from the oils of Mentha spicata and Anethum sowa.* Flavour and Fragrance Journal, 2002. **17**(1): p. 59-63.
137. McGeady, P., D.L. Wansley, and D.A. Logan, *Carvone and Perillaldehyde Interfere with the Serum-Induced Formation of Filamentous Structures in Candida a lbicans at Substantially Lower Concentrations than Those Causing Significant Inhibition of Growth.* Journal of natural products, 2002. **65**(7): p. 953-955.
138. de Carvalho, C.C.C.R. and M.M.R. da Fonseca, *Carvone: Why and how should one bother to produce this terpene.* Food Chemistry, 2006. **95**(3): p. 413-422.
139. Chan, Y.W., et al., *Plasma polymerized carvone as an antibacterial and biocompatible coating.* Materials Science and Engineering: C, 2016. **68**: p. 861-871.
140. Juergens, U., et al., *Anti-inflammatory activity of 1.8-cineol (eucalyptol) in bronchial asthma: a double-blind placebo-controlled trial.* Respiratory medicine, 2003. **97**(3): p. 250-256.
141. Dalleau, S., et al., *In vitro activity of terpenes against Candida biofilms.* International journal of antimicrobial agents, 2008. **31**(6): p. 572-576.
142. Serafino, A., et al., *Stimulatory effect of Eucalyptus essential oil on innate cell-mediated immune response.* Bmc Immunology, 2008. **9**(1): p. 17.
143. Juergens, U.R., et al., *Inhibitory activity of 1, 8-cineol (eucalyptol) on cytokine production in cultured human lymphocytes and monocytes.* Pulmonary pharmacology & therapeutics, 2004. **17**(5): p. 281-287.
144. Pegalajar-Jurado, A., et al., *Antibacterial activity studies of plasma polymerised cineole films.* Journal of Materials Chemistry B, 2014. **2**(31): p. 4993-5002.
145. Mann, M.N. and E.R. Fisher, *Investigation of Antibacterial 1, 8-Cineole-Derived Thin Films Formed via Plasma-Enhanced Chemical Vapor Deposition.* ACS applied materials & interfaces, 2017. **9**(42): p. 36548-36560.
146. Jalali-Heravi, M., B. Zekavat, and H. Sereshti, *Characterization of essential oil components of Iranian geranium oil using gas chromatography–mass spectrometry combined with chemometric resolution techniques.* Journal of Chromatography A, 2006. **1114**(1): p. 154-163.
147. Edwards-Jones, V., et al., *The effect of essential oils on methicillin-resistant Staphylococcus aureus using a dressing model.* Burns, 2004. **30**(8): p. 772-777.

148. Al-Jumaili, A., K. Bazaka, and M.V. Jacob, *Retention of Antibacterial Activity in Geranium Plasma Polymer Thin Films.* Nanomaterials, 2017. **7**(9): p. 270.
149. Al-Jumaili, A., et al., *The Electrical Properties of Plasma-Deposited Thin Films Derived from Pelargonium graveolens.* Electronics, 2017. **6**(4): p. 86.
150. Tegoulia, V.A. and S.L. Cooper, *Staphylococcus aureus adhesion to self-assembled monolayers: effect of surface chemistry and fibrinogen presence.* Colloids and Surfaces B: Biointerfaces, 2002. **24**(3): p. 217-228.
151. Bazaka, K. and M.V. Jacob, *Nanotribological and nanomechanical properties of plasma-polymerized polyterpenol thin films.* Journal of Materials Research, 2011. **26**(23): p. 2952-2961.
152. Bae, I., et al., *Characterization of organic polymer thin films deposited using the PECVD method.* JOURNAL-KOREAN PHYSICAL SOCIETY, 2007. **50**(6): p. 1854.
153. Bazaka, K. and M.V. Jacob, *Effects of iodine doping on optoelectronic and chemical properties of polyterpenol thin films.* Nanomaterials, 2017. **7**(1): p. 11.
154. Vasilev, K., S.S. Griesser, and H.J. Griesser, *Antibacterial surfaces and coatings produced by plasma techniques.* Plasma Processes and Polymers, 2011. **8**(11): p. 1010-1023.
155. Jampala, S.N., et al., *Plasma-enhanced synthesis of bactericidal quaternary ammonium thin layers on stainless steel and cellulose surfaces.* Langmuir, 2008. **24**(16): p. 8583-8591.
156. Barnes, L. and I. Cooper, *Biomaterials and Medical Device-Associated Infections*. 2014: Elsevier.
157. Lischer, S., et al., *Antibacterial burst-release from minimal Ag-containing plasma polymer coatings.* Journal of the Royal Society Interface, 2011. **8**(60): p. 1019-1030.
158. Bayram, O., *Determination of the optical and chemical properties of aniline doped plasma polymerized cineole thin films synthesized at various RF powers.* Journal of Materials Science: Materials in Electronics, 2018.
159. Bazaka, K., et al., *Photostability of plasma polymerized γ-terpinene thin films for encapsulation of OPV.* Scientific Reports, 2017. **7**.
160. Bazaka, K. and M. Jacob, *Synthesis of radio frequency plasma polymerized non-synthetic Terpinen-4-ol thin films.* Materials Letters, 2009. **63**(18): p. 1594-1597.
161. Yasuda, H., *Plasma polymerization*. 2012: Academic press.
162. Ahmad, J., et al., *Structural Characterization of γ-Terpinene Thin Films Using Mass Spectroscopy and X-Ray Photoelectron Spectroscopy.* Plasma Processes and Polymers, 2015. **12**(10): p. 1085-1094.
163. Easton, C. and M. Jacob, *Optical characterisation of radio frequency plasma polymerised Lavandula angustifolia essential oil thin films.* Thin Solid Films, 2009. **517**(15): p. 4402-4407.

164. Taguchi, D., et al., *Analyzing hysteresis behavior of capacitance–voltage characteristics of IZO/C60/pentacene/Au diodes with a hole-transport electron-blocking polyterpenol layer by electric-field-induced optical second-harmonic generation measurement.* Chemical Physics Letters, 2013. **572**(Supplement C): p. 150-153.
165. Ahmad, J., K. Bazaka, and M. Jacob, *Optical and Surface Characterization of Radio Frequency Plasma Polymerized 1-Isopropyl-4-Methyl-1,4-Cyclohexadiene Thin Films.* Electronics, 2014. **3**(2): p. 266-281.
166. Kim, M., et al., *High-rate deposition of plasma polymerized thin films using PECVD method and characterization of their optical properties.* Surface and Coatings Technology, 2003. **169**: p. 595-599.
167. Ahmad, J., et al., *Wetting, solubility and chemical characteristics of plasma-polymerized 1-isopropyl-4-methyl-1, 4-cyclohexadiene thin films.* Coatings, 2014. **4**(3): p. 527-552.
168. Jacob, M. and K. Bazaka, *Fabrication of Electronic Materials from Australian Essential Oils*. 2010: Australian Government: Rural Industries Research and Development Corporation.
169. Bazaka, K., et al., *Plasma-assisted surface modification of organic biopolymers to prevent bacterial attachment.* Acta biomaterialia, 2011. **7**(5): p. 2015-2028.
170. Al-Jumaili, A., et al., *Review on the Antimicrobial Properties of Carbon Nanostructures.* Materials, 2017. **10**(9): p. 1066.
171. Kumar, A., et al., *Plasma Polymerization: Electronics and Biomedical Application*, in *Plasma Science and Technology for Emerging Economies*. 2017, Springer. p. 593-657.
172. Hegemann, D., et al., *Macroscopic description of plasma polymerization.* Plasma Processes and Polymers, 2007. **4**(3): p. 229-238.
173. De Masi, L., et al., *Assessment of agronomic, chemical and genetic variability in common basil (Ocimum basilicum L.).* European Food Research and Technology, 2006. **223**(2): p. 273.
174. Mastromatteo, M., et al., *Combined effects of thymol, carvacrol and temperature on the quality of non conventional poultry patties.* Meat science, 2009. **83**(2): p. 246-254.
175. Turek, C. and F.C. Stintzing, *Stability of essential oils: a review.* Comprehensive Reviews in Food Science and Food Safety, 2013. **12**(1): p. 40-53.
176. Friedman, M., N. Kozukue, and L.A. Harden, *Cinnamaldehyde Content in Foods Determined by Gas Chromatography−Mass Spectrometry.* Journal of Agricultural and Food Chemistry, 2000. **48**(11): p. 5702-5709.
177. Bäcktorp, C., et al., *Theoretical investigation of linalool oxidation.* The Journal of Physical Chemistry A, 2006. **110**(44): p. 12204-12212.

178. Selvaag, E., J.Ø. Holm, and P. Thune, *Allergic contact dermatitis in an aroma therapist with multiple sensitizations to essential oils.* Contact dermatitis, 1995. **33**(5): p. 354-355.
179. Bleasel, N., B. Tate, and M. Rademaker, *Allergic contact dermatitis following exposure to essential oils.* Australasian Journal of Dermatology, 2002. **43**(3): p. 211-213.
180. Edris, A.E., *Pharmaceutical and therapeutic potentials of essential oils and their individual volatile constituents: a review.* Phytotherapy research, 2007. **21**(4): p. 308-323.
181. Uter, W., et al., *Contact allergy to essential oils: current patch test results (2000–2008) from the Information Network of Departments of Dermatology (IVDK).* Contact dermatitis, 2010. **63**(5): p. 277-283.
182. Brand, C., et al., *Tea tree oil reduces the swelling associated with the efferent phase of a contact hypersensitivity response.* Inflammation Research, 2002. **51**(5): p. 236-244.
183. Herman, A., K. Tambor, and A. Herman, *Linalool Affects the Antimicrobial Efficacy of Essential Oils.* Current Microbiology, 2016. **72**(2): p. 165-172.
184. Karbach, J., et al., *Antimicrobial effect of Australian antibacterial essential oils as alternative to common antiseptic solutions against clinically relevant oral pathogens.* Clin Lab, 2015. **61**(1-2): p. 61-8.
185. Maddocks-Jennings, W., *Critical incident: idiosyncratic allergic reactions to essential oils.* Complementary Therapies in Nursing and Midwifery, 2004. **10**(1): p. 58-60.
186. Friedrich, J., *Pulsed-Plasma Polymerization*, in *The Plasma Chemistry of Polymer Surfaces*. 2012, Wiley-VCH Verlag GmbH & Co. KGaA. p. 377-456.

Chapter III

The Fundamental Properties of Geranium Plasma Polymer Thin Films

The thin film fabrication method and the details of geranium oil-based plasma polymers were described in this chapter. The optical, mechanical, topographical and chemical properties of geranium polymers were studied. In addition, the antibacterial activity of geranium polymers were demonstrated against important human pathogens.

This chapter was published as: Al-Jumaili, A., K. Bazaka, and M.V. Jacob, *Retention of Antibacterial Activity in Geranium Plasma Polymer Thin Films.* Nanomaterials, 2017. 7(9): p. 270.

Abstract

Bacterial colonisation of biomedical devices demands novel antibacterial coatings. Plasma-enabled treatment is an established technique for selective modification of physicochemical characteristics of the surface and deposition of polymer thin films. We investigated the retention of inherent antibacterial activity in geranium based plasma polymer thin films. Attachment and biofilm formation by *Staphylococcus aureus*, *Pseudomonas aeruginosa*, and *Escherichia coli* was significantly reduced on the surfaces of samples fabricated at 10 W radio frequency (RF) power, compared to that of control or films fabricated at higher input power. This was attributed to lower contact angle and retention of original chemical functionality in the polymer films fabricated under low input power conditions. The topography of all surfaces was uniform and smooth, with surface roughness of 0.18 and 0.69 nm for films fabricated at 10 W and 100 W, respectively. Hardness and elastic modules of films increased with input power. Independent of input power, films were optically transparent within the visible wavelength range, with the main absorption at ~290 nm and optical band gap of ~3.6 eV. These results suggest that geranium extract-derived polymers may potentially be used as antibacterial coatings for contact lenses.

III.1. Introduction

Medical devices are a critical part of the current healthcare system. However, their usage has led to the emergence of device-associated infections. Contamination of medical devices by microorganisms is associated with substantial morbidity, as well as substantial healthcare costs [1,2]. Abiotic surfaces are vulnerable to microbial attachment and growth, and eventually, biofilm

formation; as such, these surfaces may act as a reservoir of chronic infection [3]. Indeed, 64% of hospital-acquired infections worldwide are attributed to attachment of viable bacteria to medical devices and implants [4], and a reported 80% of the global impact of surgical site infections involve microbial biofilms [5]. When protected by the biofilm, bacterial cells are *significantly less susceptible* to antibiotics and host immune responses than planktonic bacteria of the same strain, and as such, biofilms are more difficult to clear [6]. Emergence of microbial strains resistant to one or more of the available synthetic antibiotics creates further challenges for the treatment of implant-associated infections. Significant examples include methicillin-resistant *Staphylococcus aureus*, NDM-1 producing *Klebsiella pneumoniae*, vancomycin-resistant *Enterococcus*, and multidrug-resistant *Mycobacterium tuberculosis* [7].

To substantially alleviate pathogenic infections, the development of effective self-disinfecting surface coatings for medical devices is vital. Several surfaces have been adapted to inhibit and/or reduce microbial adhesion and proliferation via antibiofouling and/or bactericidal activity, depending on the effect the surface exerts on the microorganism [8]. Antibiofouling materials may resist the initial attachment of microorganisms, due to the existence of unfavourable surface micro-features and/or surface chemistry. On the other hand, bactericidal surfaces may impede colonisation by killing the microorganisms on contact, via surface-immobilised antimicrobial macromolecules, or by releasing biocidal molecules, e.g., polymeric biocides [9]. However, self-disinfecting surfaces often suffer from significant drawbacks, such as uncontrolled material degradation, premature mechanical failure, and limited biocompatibility [10].

In recent years, there has been an increasing interest in the use of plant-derived compounds as natural antimicrobials [11,12]. Essential oils and plant extracts are rich sources of biologically-active compounds with mechanisms that are distinct from those of currently used synthetic antibiotics, which should limit the emergence of bacterial resistance [13]. Among these natural antimicrobial agents, geranium (*Pelargonium graveolens*) essential oil exhibits strong activity against a broad spectrum of bacterial strains [14,15]. When used in solution or as an aerosol, geranium oil was effective against clinically-significant human pathogens, such as gram-positive *S. aureus* and *Enterococcus faecalis*, and gram-negative *P. aeruginosa*, *Proteus mirabilis*, and *Escherichia coli*, and the fungi *Candida albicans* [16,17]. However, until recently, essential oils have rarely been used for fabrication of biologically-active coatings, due to a complex, multi-component nature of essential oils and extracts, which may vary with season and geographic location [18]. Recent advances in cold plasma polymerisation have enabled the conversion of essential oils and their derivatives into thin, highly-adherent and defect-free optically-transparent coatings, whose biological activity and degradation kinetics can be controlled by controlling the chemical structure of the precursor and the plasma processing conditions [19–21].

This paper investigates the synthesis, material properties, and antibacterial activity of geranium oil-based polymers fabricated using plasma polymerisation. To our knowledge, this is the first report on the use of polymers derived from geranium oil as an antibacterial coating.

III.2. Methods

III.2.1. Materials

A precursor material was selected because of its strong antibacterial activity against gram-negative and gram-positive bacteria, and compatibility with the plasma polymerisation process [14,22]. The geranium essential oil was procured from Australian Botanical Products (ABP, Victoria, Australia), and was used without further modification. According to the manufacturer, the main compounds include citronellol (32%), geraniol (15%), linalool (6%), isomenthone (6%), geranyl formate (2.5%), tiglate (2%), citronellyl formate (6%), guaia-6,9-diene, and 10-epi-γ eudesmol (5%). Citronellol ($C_{10}H_{20}O$) and geraniol ($C_{10}H_{18}$) are aromatic acyclic monoterpene alcohols, and are considered to be very potent bactericides responsible for the biological action of geranium oil [23–25]. From a processing point of view, geranium oil is compatible with plasma polymerisation (plasma-enhanced chemical vapour deposition), as this oil is highly volatile at room temperature, and so no external heating nor carrier gas is required to deliver the precursor units to the site of deposition. Geranium oil has a density of 1.044 g/mL at 25 °C, a boiling point of 250–258 °C, and refractive index of 1.53 at 20 °C.

III.2.2. Polymer Synthesis

Microscope glass slides (76 mm × 26 mm) and cover glass No.5 (19 mm) were cleaned with commercial decon, washed extensively with distilled water, then sonicated in distilled water for 20 min. Thereafter, substrates were rinsed with acetone, subjected to propan-2-ol bath for 15 min, and finally dried by air. Plasma synthesis was carried out in a custom-made cylindrical glass chamber (*l*: 90 cm, *d*: 5 cm). The reactor chamber was evacuated to pressure of 0.2 mbar using a double stage rotary pump (JVAC–DD150, Victoria, Australia). Radio frequency (RF) generator model ACG-3B (MKS Instruments, Andover, MA, USA) was run in the continuous mode at 13.56 MHz to provide input power through a matching network. Two external parallel copper rings were utilised as electrodes, separated by a distance of 9 cm. Substrates were placed at equal distance from both electrodes. The distance between the substrate and the monomer inlet was 20 cm. Deposition times ranged from 30 min to 120 min, yielding films with thicknesses ranging from ~450 nm to 1500 nm. In each experiment, the monomer vial was loaded with 0.5 g (~12 drops) of geranium oil. The monomer flow rate (*F*) was calculated using the relation 1, derived from the ideal gas equation [26]:

$$F = \frac{dp}{dt} \times 16172 \, \frac{V}{T} \quad (1)$$

where p is the pressure inside the chamber (mbar), and t is time (s), V is the volume of the chamber (L), and T is the ambient temperature (K).

Initially, the chamber was evacuated to 0.2 mbar, then the precursor gas was released into the chamber until the pressure reached a stable value, at which point the outlet valve was closed, and the pressure was measured every 5 s for 1 min. It was estimated that the geranium flow rate during the polymerisation process was 16.22 cm^3/min.

III.3. Polymer Characterisation

III.3.1. Chemical Properties

Perkin Elmer Spectrum 100 Fourier transform infrared (FTIR) spectrometer (Perkinelmer Inc., Boston, MA, USA) was employed in the transmission mode to identify components and chemical properties of fabricated films. Films were deposited on potassium bromide pellets (KBr), and the spectra were acquired from 4000 to 500 cm^{-1} with resolution of 4 cm^{-1} averaged across 32 scans.

III.3.2. Optical Properties

Optical constants and film thickness were identified using Variable Angle Spectroscopic Ellipsometry (JA Woollam-M2000 D, Lincoln, NE, USA). Ellipsometry measures a change in polarisation as light is reflected from the surface of a film. The polarisation change is represented as an amplitude ratio (Ψ), and the phase difference (Δ). The ellipsometric parameters Ψ and Δ were acquired at three different angles (55°, 60° and 65°, in addition to transmission data) to measure the refractive index (n), extinction co-efficient (k), and film thickness at wavelength range of 200–1000 nm. The software package (WVASE32, Lincoln, NE, USA) was used for modelling. First, to estimate film thickness, a three-layer model consisting of a previously modelled substrate layer, a Cauchy layer (to represent the film), and a surface roughness layer were applied to the data within the 400–1000 nm region where the film is optically transparent. After point-by-point approximation, optical constants were obtained by converting the Cauchy layer to GenOsc layer and applying Gaussian oscillator to obtain the best fit to the data. UV–vis data were collected using an Avantes spectrophotometer (Avaspec-2048, Apeldoorn, The Netherlands) fitted with an Avalight-DHc light source. Tauc equation was applied to calculate the optical band gap.

III.3.3. Surface Topography and Mechanical Properties

Surface morphology was examined using a low-noise scanning and high-resolution atomic force microscope AFM (NT-MDT NTEGRA, Moscow, Russian) with a scanning area of 10 μm × 10 μm and 3 μm × 3 μm. AFM was operated in the tapping mode, where the cantilever oscillated directly above the surface to acquire data. This mode was preferable, as it decreased the inelastic deformations of the investigated surface, as well as reduced the effective forces applied to the sample. All measurements were done under ambient conditions. Software Nova (Version 1.0.26, Moscow, Russian) was used to analyse the data with the fitting correction value (polynomial order of 4).

A Berkovich Triboscope indenter (Hysitron, Minneapolis, MN, USA) was interfaced with the AFM Tribo head for the determination of mechanical properties. Berkovich indenter has the geometry of a three-sided pyramid (70.3° equivalent semi-opening angle). To obtain accurate data, the cantilever sensitivity was calibrated prior to measurements using fused silica, then, drift correction was applied. Typical loads ranged from 300 to 1000 μN with a fixed loading time of 3 s, holding time of 3 s, and unloading time of 5 s. Figure III.1 shows loading (unloading) versus indenter displacement, illustrating the elastic/plastic response of geranium oil-derived films.

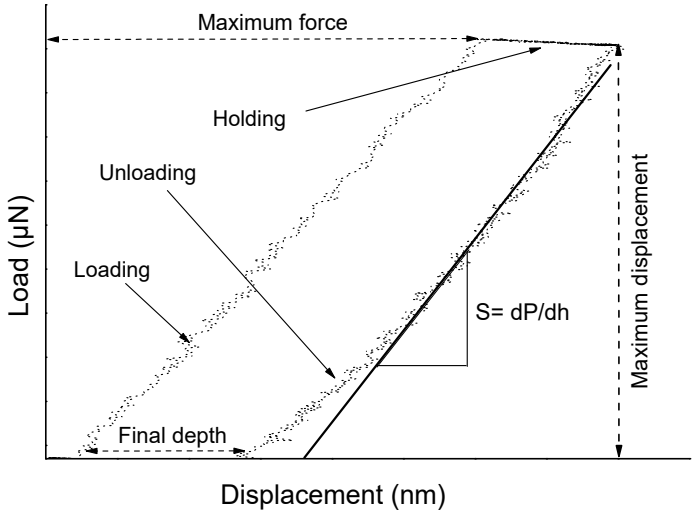

Figure III.1. Schematic of the nano-indentation test for hardness and the modulus measurement.

III.3.4. Contact Angle, Surface Tension, and Solubility

Contact angle measurements were used to determine the hydrophobicity of geranium oil-derived thin films deposited on glass. Sessile drop contact angle was measured using goniometer (KSV

CAM 101, Helsinki, Finland) and three liquids, namely distilled water, diiodomethane (DIM) and glycerol. Young–Laplace fitting was performed to estimate the contact angle, as a minimum of five measurements per sample.

The calculated values of the contact angle were used to estimate surface tension (also known as surface energy) parameters and solubility of geranium oil-derived polymer films employing van Oss, Chaudhury, and Good (VCG) method [27]:

$$(1 + cos\theta)\gamma_L = 2\sqrt{\gamma_S^{LW} + \gamma_L^{LW}} + \sqrt{\gamma_S^+ + \gamma_L^-} + \sqrt{\gamma_S^- + \gamma_L^+} \quad (2)$$

where θ is the contact angle, γ_L the surface tension of the liquid in contact with the solid (mJ/m^2), γ_L^{LW} the apolar component of the surface tension of the liquid (mJ/m^2), γ_S^{LW} the apolar component of the surface energy of the solid (mJ/m^2), γ_S^+ the electron-acceptor parameter of the solid (mJ/m^2), γ_S^- the electron-donor parameter of the solid (mJ/m^2), γ_L^+ the electron-acceptor parameter of the liquid (mJ/m^2), and γ_L^- the electron-donor parameter of the liquid (mJ/m^2).

The VCG method requires a minimum of three liquids, an apolar liquid such as DIM (where $\gamma^+ = \gamma^- = 0$), as well as two polar liquids, like water and glycerol. The surface tension parameters of the used liquids are commonly presented in the literature [28], and are summarised in Table III.1.

Table III.1. Surface tension parameters for water, diiodomethane (DIM), and glycerol used in experiments.

Solvent	Surface Tension Parameters, mJ/m^2				
	γ	γ^{LW}	γ^{AB}	γ^+	γ^-
Water	72.8	21.8	51.0	25.5	25.5
DIM	50.8	50.8	0.0	0.0	0.0
Glycerol	64.0	34.0	30.0	3.9	57.4

Once the surface tension values for the solid and liquid are determined, the interfacial tension γ_{SL} can be calculated from the individual surface tension parameters as:

$$\gamma_{SL} = \left(\sqrt{\gamma_S^{LW}} - \sqrt{\gamma_L^{LW}}\right)^2 + 2\left(\sqrt{\gamma_S^+\gamma_S^-} + \sqrt{\gamma_L^+\gamma_L^-} - \sqrt{\gamma_S^+\gamma_L^-} - \sqrt{\gamma_S^-\gamma_L^+}\right) \quad (3)$$

The solubility of the geranium oil-based polymer films (ΔG) in different solvents is then estimated from the values of the interfacial tension as:

$$\Delta G_{121} = -2\,\gamma_{SL} \quad (4)$$

III.3.5. Bacterial Studies

III.3.5.1. Cell Cultures

Among clinically-significant pathogenic bacteria, infections due to the Staphylococci, particularly gram-positive *S. aureus*, and gram-negative *P. aeruginosa* and *E. coli*, are most frequently associated with the use of implants [8,29]. Given their significance, in this study, *S. aureus* CIP 65.8, *P. aeruginosa* ATCC 9025, and *E. coli* K12 were acquired from the American Type Culture Collection (ATCC, Manassas, VA, USA) and Culture Collection of the Institut Pasteur (CIP, Paris, France). For each experiment, a fresh suspension was prepared by first refreshing the frozen stock culture on nutrient agar (Oxoid), then growing them overnight in 100 mL of nutrient broth at 37 °C, while shaking at 100 rpm. Cells were harvested at the logarithmic stage of growth, and their density adjusted to OD_{600} = 0.3 to ensure uniform starting culture. A haemocytometer was used to quantify cell numbers in suspension prior to seeding onto polymer surfaces.

III.3.5.2. Incubation

Sterile polymer-coated glass slides and uncoated glass slides (as control) were placed into 24 well plates, and an aliquot of 100 µL of bacterial suspension was carefully placed on the sample surface. Samples were then allowed to incubate at 37 °C and 5% CO_2 for 18 h. The experiment was run in triplicate. After incubation, the media was aspirated, and the unattached cells were removed by gently rinsing the surfaces of the samples with copious amounts of double-distilled water. Samples were then allowed to dry at 22 °C for 30 min at 55% humidity to maintain cells in a semi-hydrated state for microscopy.

III.3.5.3. Visualisation

The retained bacteria were visualised by scanning electron microscopy. Prior to imaging, samples were coated with a thin layer of gold using Sputter Coater (Leica EM-SCD005, Wetzlar, Germany). High-resolution images of the attached cells were obtained using the Scanning Electron Microscope (JEOL 7001F, Tokyo, Japan) at 1000, 5000, and 20,000× magnifications.

To differentiate viable cells among the attached bacteria and quantify the amount of extracellular polysaccharides produced by the attached cells, SYTO® 17 Red (Molecular Probes™/Invitrogen, Thermo Fisher, Carlsbad, MA, USA) and Alexa Fluor® 488 (Molecular Probes™/Invitrogen, Thermo Fisher Scientific, Carlsbad, MA, USA) stains were used to stain the bacterial cell red and extracellular polymeric substances (EPS) green, respectively. The dyes were applied following the protocol outlined in [30]. The images were obtained using a confocal scanning laser

microscope (CSLM) (Nikon A1R Confocal Microscope, New York, NY, USA). The CSLM images were processed to construct 3D images, and to quantitatively describe the images in terms of the overall volume of the biofilm per unit area of substrate (termed “biovolume”, and inclusive of both cells and EPS), and the average biofilm thickness.

III.4. Results and Discussion

III.4.1. Polymer Synthesis

The polymer thin films were successfully fabricated on substrates, including microscope glass slides, cover glass, and KBr disks, at input powers of 10, 25, 50, 75, and 100 W. Spectroscopic ellipsometry was used to estimate the polymer thicknesses. The thickness of the polymer increased linearly with time, yielding ~10.6 nm/min at 10 W. Also, the thickness of the polymer was found to be increasing with an increase in the input power.

III.4.2. Chemical Properties

Geranium essential oil is a complex, multi-component mixture of monoterpenic alcohols (geraniol, citronellol, linalool, etc.), esters (citronellyl tiglate, citronellyl formate, geranyl tiglate, etc.), monoterpenic ketones (isomenthone and menthone), monoterpenic aldehydes (geranial and neral), sesquiterpenic hydrocarbons (guaia-6,9-diene, etc.), sesquiterpenic alcohol (10-epi-γ-eudesmol), and several aromatic and oxide components [31]. Citronellol and geraniol are considered the key components, while linalool is present in a much smaller portion (for more detail on oil composition see Section 2: Materials).

Principally, the organic molecules are held together via covalent bonds, which are relatively strong, while creating a solid material via fairly weak van der Waals forces [32]. During plasma polymerisation, plasma-generated electrons gain sufficient energy to break chains of the precursor molecules, creating a rich assortment of highly reactive chemical species. The degree of fragmentation is directly related to the amount of applied energy. Thus-created precursor fragments then undergo recombination in the gas phase and on the surface of the substrate, giving rise to a highly crosslinked polymer, with a structure that is irregular and unlike that of a conventional polymer.

Figure III.2 shows the FTIR spectra obtained for geranium oil (precursor) and geranium oil-based polymer thin films. Table III.2 summarises the key bands and corresponding bond vibrations. In the precursor spectrum, a very broad and strong peak of around 3367 cm^{-1} was related to the stretch vibrations of (O–H) bonds of the alcohol. In the film spectrum, this band reduced in intensity and appeared at 3436 cm^{-1}. The very strong peaks formed at 2962 and 2872 cm^{-1} can be

attributed to the asymmetric stretching vibration modes (CH_2 and CH_3, respectively) of the methyl group. In the polymer, these peaks also decreased in intensity and occurred at 2961 and 2875 cm^{-1}, respectively. A very strong stretch vibration of the CH_3 bond appeared at 2926 cm^{-1}, and related to the methylene group, shifted slightly in the polymer spectrum towards a higher wave number at about 2933 cm^{-1}. A very weak peak at 2728 cm^{-1}, related to C=O bond stretching, vanished completely, and was not observed in the polymer spectrum. Strong peaks at 1730 and 1713 cm^{-1}, possibly linked to the symmetric starching vibrations of C=O bonds, and a medium peak at 1671 cm^{-1}, probably related to the vibration of (C=C) were observed in the precursor spectrum. These bands merged, decreased in strength, and appeared as a broad band in the polymer spectrum at about 1708 cm^{-1}. Sharp peaks at 1452 and 1377 cm^{-1} were attributed to the asymmetric and symmetric bending vibrations of C–H bonds, respectively. These vibrations were retained in reduced form and observed in the polymer at 1453 and 1376 cm^{-1}, respectively. Furthermore, peaks observed in the fingerprint region of the precursor at 1267, 1174, 1058, and 1008 cm^{-1}, combined and radically reduced in the polymer spectrum, and were detected as very weak and united broad bands.

The reduction in the peak intensities and disappearance of some peaks in the polymer can be interpreted as the precursor molecules being partially dissociated as a result of being subjected to the RF plasma field [33]. However, the absorption band of C=O asymmetric stretching observed in the 1800−1600 cm^{-1} region was possibly due to the post oxidation of the trapped free radicals, confined during film formation [34]. The emergence of a strong methyl peak at 1452 cm^{-1}, and relatively weaker methylene band at 1377 cm^{-1}, confirms that geranium oil-derived films comprise a large quantity of short unsystematically-branched chains, rather than long linear backbone structures, a structure typically associated with plasma polymer [26].

Table III.2. . FTIR spectra assignments for geranium essential oil and geranium oil-based polymer.

Assignment	Group Frequency, cm^{-1}	
	Precursor	Polymer
Stretching (OH)	3367	3436
Asymmetric stretching, methyl ($–CH_2$)	2962	2961
Symmetric stretching, methylene ($–CH_3$)	2926	2933
Asymmetric Stretching methyl ($–CH_3$)	2872	2875

Stretching aldehyde (C=O)	2728	-
Stretching (C=O), aldehyde	1730	1708
Stretching (C=O) carbonyl	1713	-
Alkenyl (C=C)	1671	1625
Asymmetric bend methyl (C–H)	1452	1453
Symmetric bend methyl (C–H)	1377	1376
In-plane bending (O–H)	1267	
Skeletal (C=C)	1174	Merged in broad band
Stretching, alcohol (C–O)	1058 and 1008	

Comparison of the resulting films at different deposition powers (10 W and 100 W) revealed that with increasing input power, the crosslinking of the fabricated polymers increases. This is possibly owing to the higher fragmentation rate that occurs in higher density plasmas, due to an increase in inelastic collisions among high energetic electrons and precursor species, which could cause the overlapping of electronic orbitals [34].

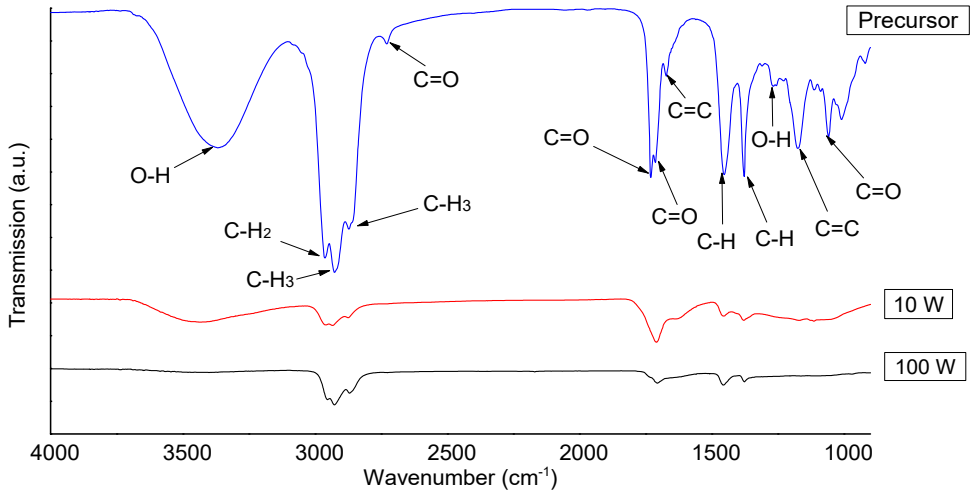

Figure III.2. . FTIR spectra of geranium essential oil (precursor) and geranium oil-based polymer fabricated at 10 W and 100W.

III.4.3. Optical Properties

Determination of material optical properties, including transparency, the spectral dependence of the refractive index and extinction coefficient, and optical band gap energy, are essential in optics-

related industries [35,36]. Independent of applied power, geranium oil-derived polymer films were revealed to be optically transparent within the visible wavelength range.

Refractive index (n), a measure that describes how light propagates through the medium, was found to be not significantly dependent on the RF power, with all curves characterised by a similar shape (Figure III.3.). At a short wavelength of 200 nm, the variation in the refractive index between polymers fabricated at applied powers of 10 W and 100 W was approximately ~0.0097. At wavelengths above 900 nm, the variation in the refractive index was ~0.0069. This result agrees with previous studies that showed a variation of less than 1% for thin films derived from other essential oil precursors, e.g., γ-terpinene and linalyl acetate [37,38]. In contrast, Cho et al. found that the refractive index of ethyl-cyclohexane films increased when the RF power was increased [39].

The extinction coefficient (k), a measure of how a medium absorbs light at a specified wavelength, also showed very little dependence on the applied power, especially in the high wavelength region (above 900 nm), as the variation was 0.0013. At a short wavelength of 200 nm, the variation in the refractive index for polymers fabricated at applied powers of 10 W and 100 W was ~0.0268. As the films have optical constants similar to glass and good transparency in the visible region, it is suggested they are suitable candidates for integration into protective coatings in optical and biomedical devices, such as lenses [38,40].

Figure III.4 shows UV–vis spectra of geranium oil-derived polymer thin films deposited on glass with increasing RF powers, from 10 to 100 W. The maximum absorption peak was observed at approximately 290 nm, which possibly relates to π–π* transitions [41]. The absorption peak width increased slightly with an increase in the RF power. This could be associated with an increase in the length of the conjugated π-system, which usually shifts the absorption maximum peak to a longer wavelength [42]. However, no significant shift in location or variation in magnitude of the absorbance peak was detected with respect to RF power. This was also observed in films fabricated from linalyl acetate by plasma polymerisation [38]. The findings show that the absorption spectra are repeatable under similar deposition conditions (RF power, pressure, temperature, etc.). The optical absorbance results strongly suggest that geranium films can be used as encapsulating (protective) layers for organic electronics to extend the lifetime and preserve efficiency of oxygen- and water-sensitive organic materials [40].

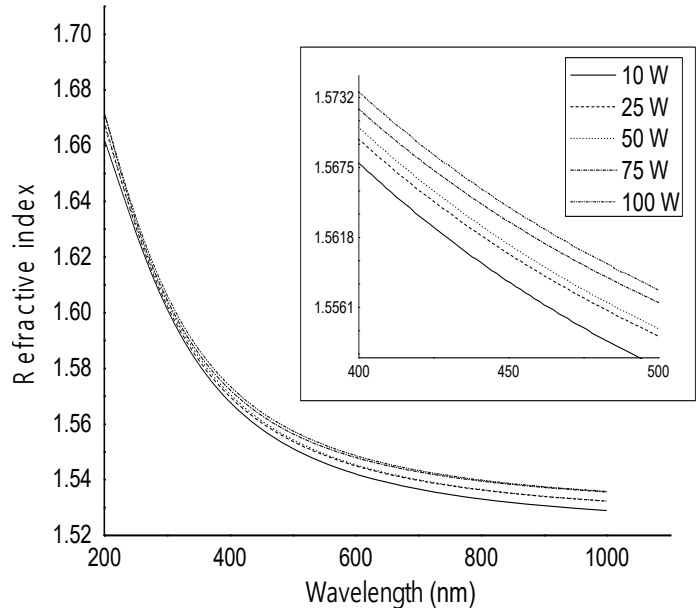

(a)

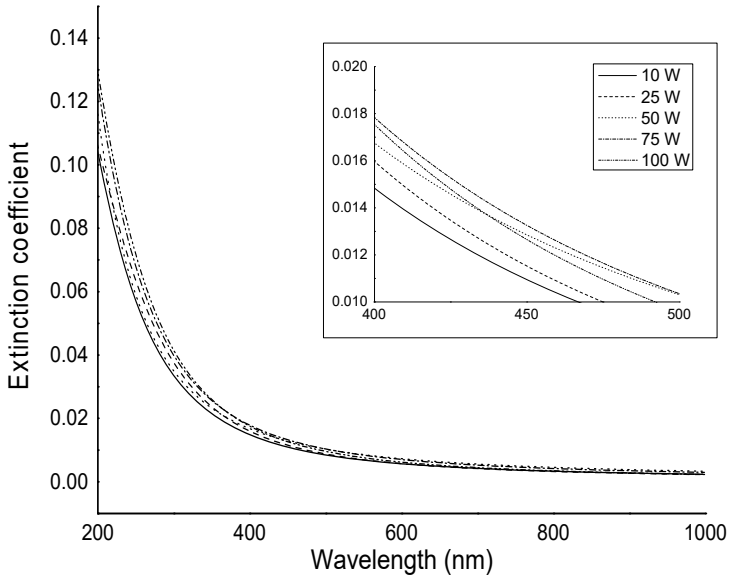

(b)

Figure III.3. Optical constants of geranium oil-derived polymer films fabricated at various deposition powers; (a) Refractive index; (b) Extinction coefficient.

The energy gap of geranium oil-derived polymer films was determined using the optical absorption coefficient data acquired from UV–vis spectroscopy measurements. The optical energy gap was calculated using Tauc relation $\alpha E = A(E - E_g)^{1/n}$, where E is the photon energy, A is a constant, and $n(1/r)$ is related to the density-of-states distribution in the transport gap, and equal to 1/2, 3/2, 2, or 3 for direct or indirect transitions [43]. The MATLAB program was used

to convert UV–vis spectroscopy data to a Tauc plot, determine the linear portion of the high energy region, and extrapolate the line until it intersected with *x*-axis to estimate the optical band gap (Figure III.4). The best fit was observed at $n = 1/2$, which is related to directly allowed transitions.

A very small decrease of optical band gap with an increase in the input power was observed in the films. Samples fabricated at 10, 25, 50, 75, and 100 W had $E_g \approx 3.67$, 3.65, 3.60, 3.61, and 3.60 eV, respectively. The optical properties of plasma polymerisation films significantly relied on the structure of the p-conjugated chains in both the ground and the excited levels, and on the inter-chain orientation [44]. The narrowing of E_g is possibly owed to dangling bonds created in the polymer structure during the fabrication. At low RF power, there was low concentration of dangling bonds because of their saturation with hydrogen atoms, while higher RF power increased the fragmentation rate in the plasma field that accelerated deposition of chains with unsaturated bonds [45]. The unsaturated bonds were expected to be reason for the foundation of structural defects and/or created some intermediate energy levels due to structural reorganisations enhancing the density of localised states in the band structure that end in low values of E_g.

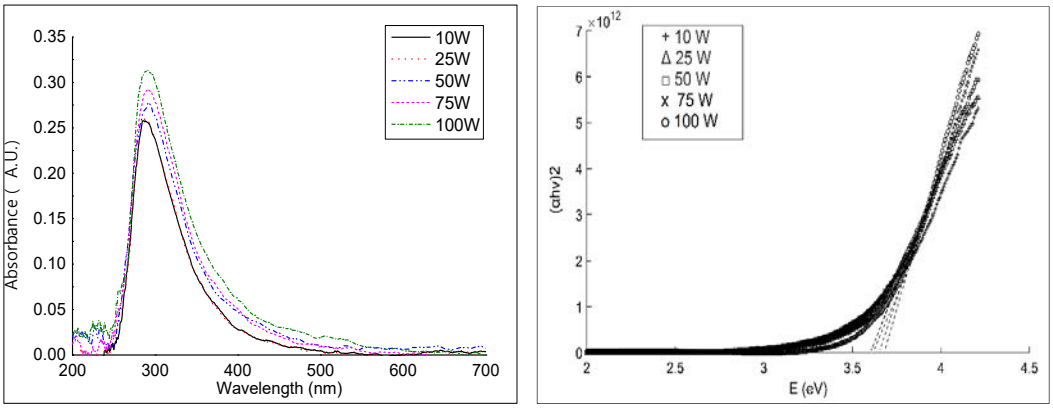

(a) (b)

Figure III.4. (a) UV–vis absorption spectrum of geranium oil-derived films; (b) The optical energy gap of geranium oil-derived films fabricated at various radio frequency (RF) powers.

III.4.4. Surface Topography

Topological and biochemical characteristics of a surface in part determine the rate of microbial adhesion. Bacterial growth and proliferation are highly associated with the size of the micro/nano-features of the surface. There is an ongoing debate among scientists regarding preferential attachment of bacteria to rougher surfaces. Proponents of the theory attribute increased cell adhesion to three main factors, namely higher surface area available for attachment, protection from shear forces, and chemical changes in cells that cause preferential physicochemical

interactions [46]. At the microscale, where the cell is much smaller than surface features, the roughness would indeed provide “hiding places”. While at nanoscale, where the features are smaller than the size of the cell, rougher surfaces would provide less points of attachment than smooth surfaces. Also, the distribution of the features on the surface is important. It has been reported that *Pseudomonas aeruginosa* and *S. aureus* cells preferentially attached to surfaces constructed of regularly spaced pits of 1 µm and 2 µm in size, but not those constructed of irregularly spaced pits of 0.2 µm and 0.5 µm [47].

In this study, AFM images were obtained to determine information regarding the surface properties. Several parameters were used to describe the surfaces, including maximum height (S_{max}), average roughness (S_a), root mean square (S_q), skewness (S_{sk}), and kurtosis (S_{ka}). S_{max}, S_a, and S_q were used to estimate the topographical characteristics of geranium oil-derived polymer films, while S_{sk} and S_{ka} were referred to when describing the surface regularity. Representative images of the surfaces of geranium oil-derived films are shown in Figure III.5. and roughness parameters for the films are summarised in table III.3.

The maximum peak height of 8.30 nm was observed on the surface of the sample fabricated at the highest deposition power (100 W) with a scanning area of 3 µm × 3 µm. S_a and S_q increased slightly as a result of an increase in the input RF power. At powers of 10, 25, and 50 W, S_a values were 0.18, 0.21, and 0.29 nm, respectively, with higher S_a values reported for the samples deposited at 75 and 100 W, at 0.63 and 0.69 nm, respectively. The increase in the roughness may be related to more energetic ions at higher RF power causing more surface bombardment and etching [48]. Irrespective of fabrication power, the average roughness values remained below 0.7 nm, confirming the smooth and uniform nature of plasma polymers from geranium oil.

Surface skewness measures the symmetry of the deviations of a surface profile about the mean line. Its value can be positive or negative, and it is sensitive to the irregularity of deep valleys or high peaks [49]. The skewness parameter can be employed to distinguish between surfaces with similar root mean square roughness or arithmetic average height values, but different shapes [50]. The maximum value of skewness for geranium oil-derived plasma polymer films was found to be 0.75 nm on the sample deposited at 75 W (10 µm × 10 µm). Another parameter frequently used to describe surfaces, surface kurtosis (S_{ka}), describes the distribution of the protrusions with respect to the mean line. For a mesokurtic distribution that is similar to or identical to normal distribution, the kurtosis is zero. Distributions with positive kurtosis are leptokurtic, and are characterised by high peaks, whereas platykurtic distributions have negative kurtosis, and are characterised by flat-topped curves [51]. All investigated samples exhibited S_{sk} and S_{ka} values falling fairly close to 0 and 3, respectively, suggesting surfaces with a symmetrical distribution

of peaks and valleys [29]. It has been observed that skewness and kurtosis parameters of geranium oil-derived films are independent of the RF deposition power.

Independent of deposition power, the topographical features appeared to be uniform, smooth, and pinhole free. The uniformity indicates that polymerisation reactions occurred essentially on the surface of the substrate, instead of in the gas phase. The variances in the sample profiles, and both scanning areas, were not statistically significant. Besides possessing considerable smooth surfaces, films fabricated by the plasma polymerisation process reveal high spatial uniformity and good adhesion to the substrate [52]. AFM results also revealed that the films' entropy, or the level of disorder or randomness in a system, increased as a result of fabrication power. The entropy increases are possibly related to the surface flatness decreases [53].

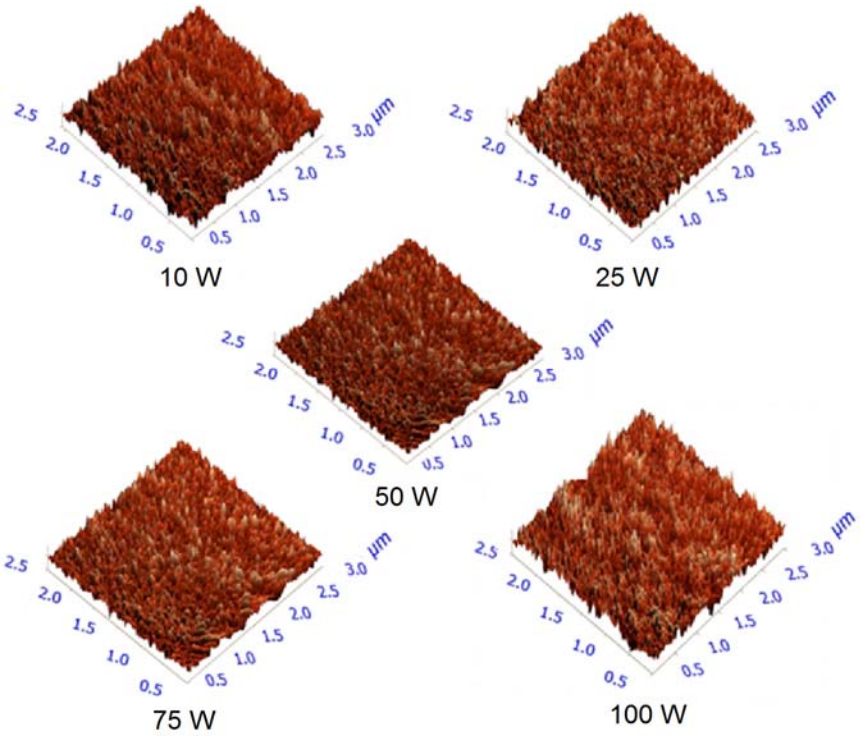

Figure III.5. Typical three-dimensional atomic force microscope images of 3 µm × 3 µm scanning area of geranium oil-derived film surfaces fabricated at various RF power.

Table III.3. Surface profiles of 3 µm × 3 µm and 10 µm × 10 µm of geranium oil-derived film surfaces fabricated at various RF power.

Sample	**10 W**		**25 W**		**50 W**		**75 W**		**100 W**	
Scanning area (µm)	3 ×3	10 × 10	3 × 3	10 × 10	3 × 3	10 × 10	3 × 3	10 × 10	3 × 3	10 × 10

Max, S_{max} (nm)	1.93	3.75	2.39	4.21	3.07	3.52	6.59	6.02	8.07	8.30
Average roughness, S_a (nm)	0.18	0.23	0.21	0.23	0.29	0.30	0.63	0.58	0.69	0.60
Root mean square, S_q (nm)	0.23	0.30	0.27	0.30	0.36	0.38	0.81	0.74	0.89	0.77
Surface skewness, S_{sk}	0.02	0.08	0.17	0.03	0.04	0.04	0.56	0.75	0.59	0.67
Coefficient of kurtosis, S_{ka}	0.06	0.55	0.05	0.81	0.01	0.03	0.54	1.37	0.69	1.07
Entropy	3.09	3.45	3.28	3.44	3.72	3.80	4.84	4.70	4.98	4.75

III.4.5. Mechanical Properties

In order to determine the mechanical properties of geranium oil-derived thin films, a nano-indentation test was performed. The AFM was activated in the force mode that brought the tip into contact with the tested film, pushed to a maximum load, held for a period of time, and then withdrawn. While the indenter was being pushed into the polymer, the load and displacement were identified continuously, drawing a load versus displacement curve, as presented in Figure III.6. A. For very thin polymer films, the quality of the data is limited by a number of factors. It has been discussed that creep effects on elastic modulus at higher loads are significant, even though this influence could be a result of higher unloading stiffness [54]. Thermal drift, caused by inconsistency in ambient temperature, complicates nano-indentation measurements. Peaks and valleys can affect how the indenter contacts the sample. Furthermore, the pile up and sink in phenomena are related to plastic deformation in the films, as seen in Figure III.6. B. During the holding time, it is possible that the tip would continue to move into the surface of the sample as a result of the viscous creep. Therefore, six indents were randomly located on the films to reduce the inaccuracy due to creep or roughness effects. The loading forces of 300, 400, 500, 600, 700, and 1000 μN were applied, with indentations separated by at least 5 μm, as presented in Figure III.6 C, D. In order to minimise the effect of the substrate on the measurement, films with thickness of >1500 nm were tested to keep indentation depths within 10% of the film thickness, thus collecting data within the plastic response of the film only.

The hardness of geranium oil-derived thin films increased with the increase of power deposition, as shown in Table III.4. This could be associated with the increase in crosslinking in the polymers deposited at higher RF power, which potentially results in an increase in resistance against

deformation [55,56]. Similarly, an increase in elastic modulus and a decrease of contact depth with increasing RF power, have been observed. This may be attributed to the transition from spherical contact to conical contact that occurs for the Berkovich indenter used in the investigation at h_c = indenter radius/4 [37]. Liu et al. argued that the Berkovich indenter (complex shape) has higher hardness and lower elastic modulus compared to the conical indenter [57]. It is not uncommon to observe the stress relaxation at the maximum load when unloading just takes place, since the strain beneath the indenter is relatively large, and the strain rate is also very large at this point [58]. Besides, the sudden withdrawal of the indenter leads to oscillations, which may affect the measurements.

The elastic modulus and the hardness were calculated using the Oliver–Pharr nonlinear curve, which is based on the equation $P = A(h - h_f)^m$, where A and m are power law fitting parameters, h is the depth variable, and h_f is the final depth. In light of what has been written on measurement limitations, the hardness and elastic modules values presented in Table III.4 may quantitatively differ from the actual properties of geranium oil-derived thin polymer films.

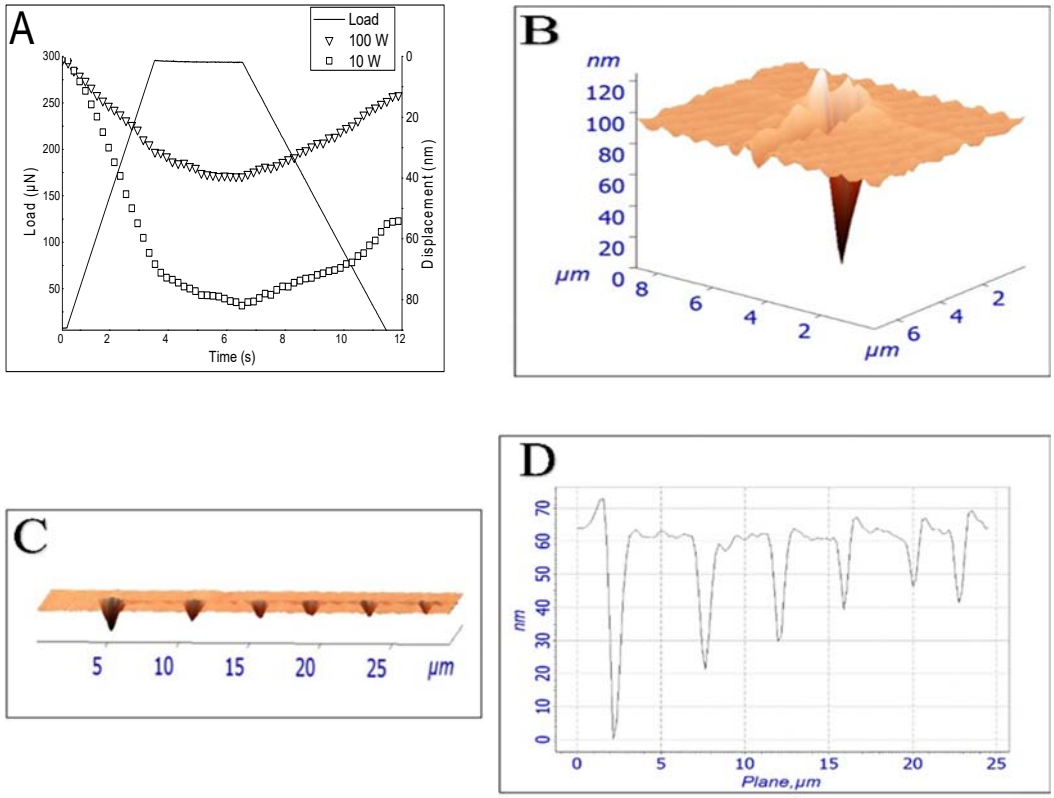

Figure III.6. (A) Load displacement versus time curve of geranium oil-derived film fabricated at 10 W and 100 W. (B) Pile up and sink in phenomena in the film. (C) AFM image of plastic impressions left behind in geranium oil-derived thin polymer fabricated at 50 W after indentations. (D) Profile plane of the investigated surface.

Table III.4. Mechanical properties of geranium oil-derived thin polymer films fabricated at various power.

Power Deposition (W)	Hardness (GPa)	Elastic Modulus (GPa)	Contact Depth (nm)	Contact Stiffness (μN/nm)	Final Depth (nm)	Contact Area (nm^2)× 10^5
10	0.63	9.39	141.88	10.44	179.87	8.24
25	0.74	11.55	123.72	12.18	156.81	8.02
50	0.74	12.51	127.03	12.79	154.28	7.29
75	0.81	16.78	105.25	16.21	127.74	6.21
100	0.85	20.61	103.78	18.28	124.08	6.16

III.4.6. Contact Angle and Wettability

The wettability of plasma polymerised films was assessed using the sessile liquid drops system. A liquid drop was gently placed on a horizontal solid substrate, where the drop formed the shape of a sphere section due to its interaction with the surface. The angle at the triple-phase contact line between the sphere and the surface was measured to determine the wettability of the surface. Theoretically, the adhesive forces between a liquid drop and a substrate are a local reaction, which is influenced by the interactions of the actual drop and the surrounding vapour with the substrate, thereby necessitating independence of the drop volume [59]. However, it has been argued that larger drops are more subject to errors as a result of gravity effects, causing sagging near the contact line, and deformations to the drop [60]. In contrast, smaller drops can cause errors due to evaporation and the interference of contact line tension, triggering deviations in measurements [61]. Further, the atmospheric conditions play a substantial role in the control of contact angles, where the partial pressure of oxygen influences the equilibrium and uniformity of the formed drop [62]. Besides, the homogeneity of the chemical composition of the surface may affect droplet symmetry [63,64]. The topography is a parameter that has to be considered, as in some cases, contact angles can be increased owing to the roughness [65]. However, contact angle measurements provide details about the character of a top surface in the range of 0.5–1.0 nm [66].

For the above reasons, the size of the droplet was carefully chosen to minimise inaccuracies in the acquired data for the test liquids. In the case of the water, a droplet volume (V) of approximately 3 μL was used, yielding dimensions of area (A) ≈ 9 mm^2, height (H) ≈ 0.90 mm, and base diameter ($2a$) ≈ 3 mm upon contact with polymer surface. For DIM (CH_2I_2), a smaller droplet of V ≈ 1.3 μL was used, producing dimensions of A ≈ 6.9 mm^2, H ≈ 0.39 mm, and $2a$ ≈

2.8 mm upon contact with polymer surfaces. For glycerol ($C_3H_8O_3$), an average droplet volume of $V \approx 1.6$ µL was used, resulting in contact droplet dimensions of $A \approx 5.7$ mm^2, $H \approx 0.66$ mm, and $2a \approx 2.33$ mm. For these dimensions, the relative error was ~1%.

In each experiment, the drop profile was recorded by video camera and solved numerically. Static contact angle data were acquired for each sample on a minimum of five points. Table III.5 presents average contact angles of geranium oil-derived polymer films fabricated at various RF power levels. At the higher power of 100 W, water contact angle was 65.6°, while at the lower power of 10 W, the contact angle value was notably lower, at 55.5°. An increase in the contact angle with an increase in the fabrication power may be attributed to a decrease in the oxygen content in the resultant polymer films. This conclusion is supported by FTIR data, which show the hydroxyl group peak reduced in intensity as RF power increased, which in turn led to a decrease in the polarity of the surfaces of films fabricated at higher RF power [67,68].

Examination of the evolution of contact angle with time (Figure III.7) provides further evidence for the dependence of contact angle on the degree of crosslinking, with a relatively high rate of change in the case of polymers fabricated at lower RF power. This behaviour is indicative of the reorientation of functionalities at the solid–liquid interface in the films fabricated at low power, which is difficult in more crosslinked films synthesised under high RF power conditions [27]. The formation of highly crosslinked structures in films is probably owing to more fragmentation of precursor molecules as the applied power increases [27]. The resultant films become more rigid because of an increase in the bonding interconnection and dense packing. An increase in the water contact angle, with respect to input power of polyterpenol coatings deposited by plasma polymerisation, has also been reported [69].

Table III.5. Contact angles θ for geranium oil-derived thin polymer films deposited at varied RF powers.

Solvent	**Contact Angle**				
	10 W	25 W	50 W	75 W	100 W
Water	54.0	59.8	61.7	64.1	65.6
DIM	38.0	34.6	34.2	33.0	32.4
Glycerol	35.6	54.1	57.2	56.7	57.2

Geranium oil-derived polymer films revealed contact angles ranging from ~50° to 60°. Moderately hydrophilic surfaces are generally considered well-suited for biological applications,

as they facilitate and promote adhesion of multiple cell lines, and hence can be used as coatings to enhance biocompatibility of implantable and extracorporeal biomaterials [68,70]. Once the equilibrium contact angle was reached, the contact angle remained stable, indicating chemical stability of geranium oil-derived films while in contact with water. The contact angle for diiodomethane decreased with increasing RF power, whereas contact angle for glycerol showed similar behaviour with increasing RF power, to that of water.

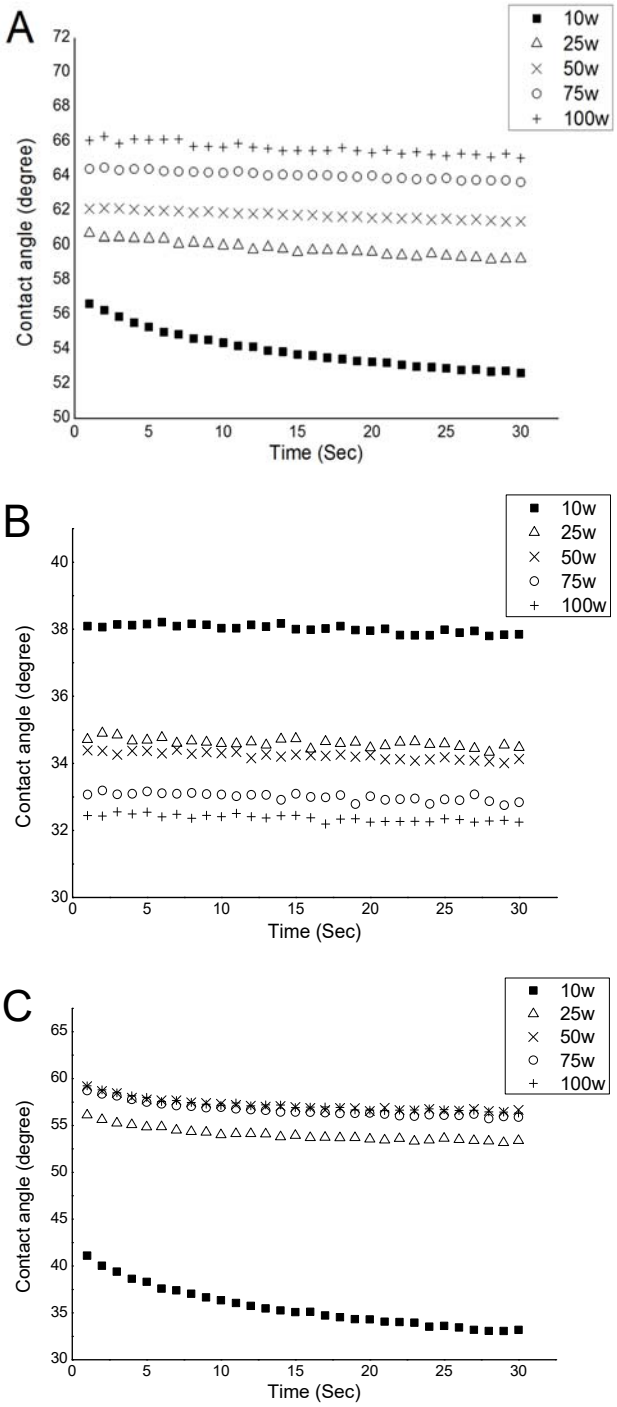

Figure III.7. Evolution of contact angle with contact time: (A) water, (B) DIM, and (C) glycerol.

III.4.7. Surface Tension Parameters and Solubility

There are several approaches to estimate the surface tension through contact angle, such as the methods by Berthelot, by Fowkes, and by van Oss, Chaudhury, and Good (VCG) [27,71,72]. It should be noted that there are unique limitations for using each of these methods. Nevertheless, the VCG three-liquid approach has been widely studied and successfully employed for determining surface tension parameters [73], and thus, was selected to estimate the surface tension values in this study. The VCG method considers the total surface tension γ of a solid surface is a summation of interfacial Lifshitz–van der Waals forces γ^{LW} (dispersive and polar) and acid–base interactions γ^{AB} (electron donor–acceptor), where $\gamma^{AB} = 2\sqrt{\gamma^{+}\gamma^{-}}$ [67].

The acquired contact angle data were used to determine the surface tension parameters summarised in Table III.6. The results indicate that an increase in RF power had a slight influence on the total surface tension of the geranium oil-derived polymer films. In particular, samples fabricated at 10 W revealed relatively high surface tension compared to samples fabricated at other RF powers. The dispersive parameter γ^{LW} showed a consistent decrease with increasing RF power. This may be because the higher power samples contained less polar moieties, such as –OH group [28]. The surface tension parameters calculated from polar liquid data, i.e., water and glycerol contact angles, decreased for increasing RF deposition power, due to an increase in the polarity of these surfaces, while the surface tension parameters estimated from contact angles for apolar liquid (DIM) displayed the opposite trend.

The highest value of γ^{+} for geranium oil-derived polymer films was 5.88 mJ/m^2, calculated for 10 W samples, and the lowest value was 0.87 mJ/m^2 for 50 W samples. The maximum value of γ^{-}, 29.82 mJ/m^2, was obtained for films deposited at 10 W, and the lowest value was 15.85 mJ/m^2, calculated for samples fabricated at 100 W. All samples displayed $\gamma^{-} > \gamma^{+}$, indicating that the tested films have monopolar surfaces, of which most are water soluble [67]. To evaluate the minimum value for γ^{-} parameter at which the polymer becomes soluble in the water, the van Oss formula (Equation. 2) was solved for γ^{LW}= 42.26 mJ/m^2. It was found that geranium oil-derived plasma polymer films become water-soluble at $\gamma^{-} > 28.96$ mJ/m^2. Thus, samples fabricated at 10 W are expected to be soluble in water, while samples fabricated at higher RF power (25, 50, 75, and 100 W) are expected to resist solubility, since their $\gamma^{-} < 28.96$ mJ/m^2.

The determination of polymer solubility (ΔG_{121}) is vital for biomaterial applications, since the material deals mainly with aqueous media, as well as for solution processing in electronics. Physically, ΔG_{121} represents the free energy change, so when $\Delta G_{121} >> 0$, the material is

solvophilic in the used liquid; while for $\Delta G_{121} << 0$, the material is solvophobic in the used liquid; for $\Delta G_{121} \approx 0$, the material is partially dissolved in the given solvent. Solubility of geranium oil-derived films in different solvents are reported in Table III.6. The polymer films were found to be solvophobic for all solvents, except for 10 W sample. The solvophobicity behaviour of geranium oil-derived films increased with input power for water and glycerol (polar solvents), while they decreased slightly for DIM (apolar solvent). This is possibly related to the increase in the polarity of the polymer surfaces, as discussed previously. The solubility results showed that the stability of fabricated polymers is influenced by both fabrication conditions, namely RF power, and the choice of the solvents. However, it is important to note that the solubility values may be quantitatively different when using another approach in the calculations of surface tension.

Table III.6. Surface tension parameters and corresponding solubility for geranium oil-derived thin polymer films deposited at varied RF powers.

Sample	**Surface Parameters**				**Interfacial Surface Tension Between Solute and Solvent**			**Surface/Liquid Solubility**		
	γ^{LW}	γ^{+}	γ^{-}	γ	γ^{SL}_{water}	$\gamma^{SL(DIM)}$	$\gamma^{SL,Glycerol}$	ΔG^{water}	ΔG^{DIM}	$\Delta G^{Glycerol}$
10 W	40.68	5.82	29.82	67.08	0.75	27.05	−1.61	−1.5	−54.10	3.22
25 W	42.21	1.21	22.06	52.54	6.134	10.72	5.48	−12.26	−21.45	−10.96
50 W	42.39	0.87	20.33	50.80	7.84	8.79	6.85	−15.68	−17.58	−13.70
75 W	42.93	1.07	17.33	51.54	10.67	8.94	6.94	−21.34	−17.88	−13.88
100 W	43.19	1.03	15.85	51.27	12.24	8.38	7.45	−24.49	−16.76	−14.90

III.4.8. Cell Attachment

The attachment and biofilm formation of *S. aureus*, *P. aeruginosa*, and *E. coli* on the surfaces of geranium oil-derived polymer films after 18 h of incubation were visualised by SEM and CSLM imaging (Figure III.8), and quantified (Table III.7). Comparison of attachment patterns revealed

notable differences for samples fabricated at different RF powers, regardless of the pathogen tested. Films fabricated at 10 W RF power displayed significant antifouling activity, preventing the attachment of bacterial cells, as well as limiting the formation of biofilm. Bacterial cells produced significantly more EPS when attached to glass control or polymer film fabricated at 50 W RF power, forming double-layer morphology, indicative of the biofilm formation. The morphologies of the cells were also different between the surfaces, with smaller cells being present on the surface of the 10 W sample compared to that of cells attached to 50 W sample or glass control. There was no significant difference between the number of cells, biovolume, or biofilm thickness obtained for the 50 W sample and control.

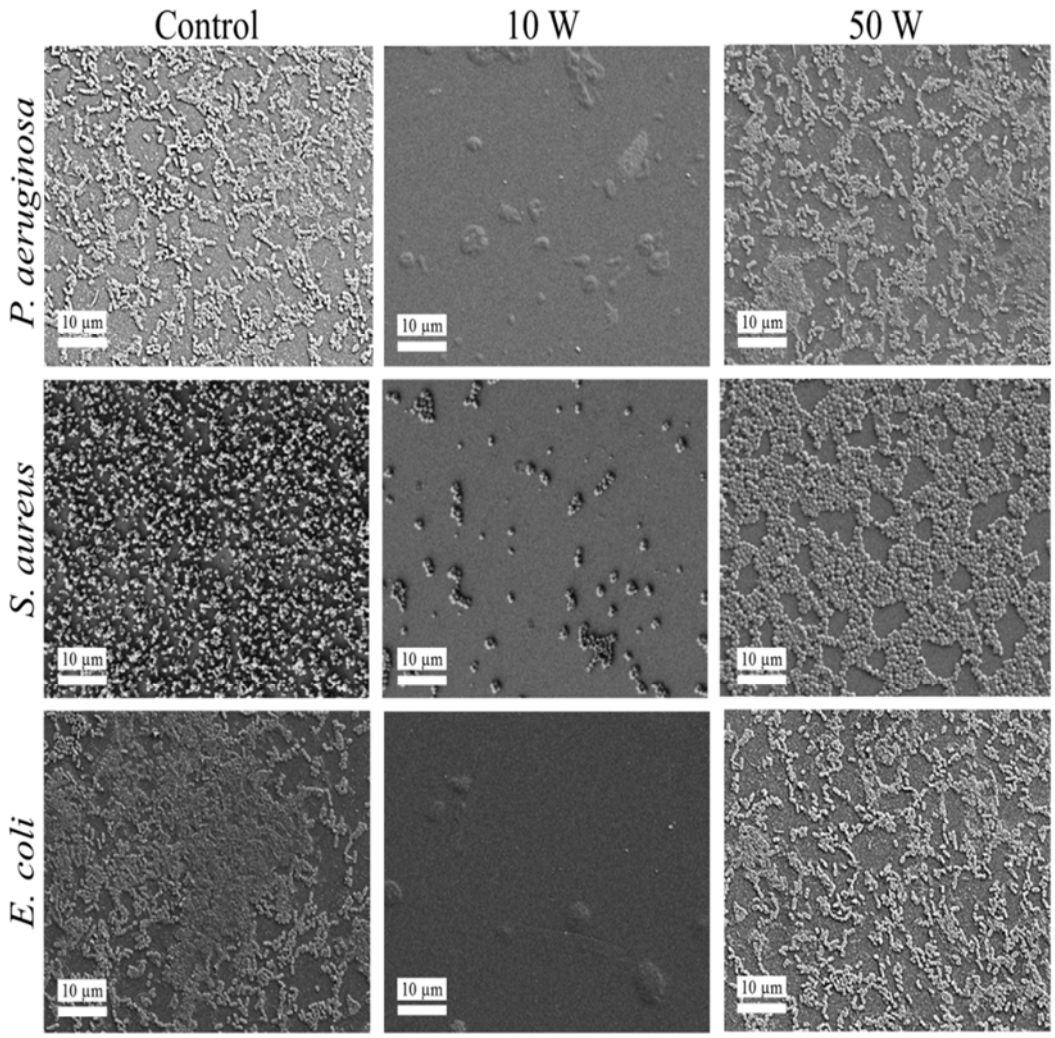

Figure III.8. Representative *P. aeruginosa*, S. *aureus*, and *E. coli* attachment patterns on the surfaces of the control glass, and geranium oil-derived polymer film samples fabricated at 10 W and 50 W after 18 h incubation. SEM images represent an overview of the attachment pattern.

These results are very similar to that reported for polyterpenol thin films, which were synthesised using plasma polymerisation from terpinene-4-ol, a broad-spectrum antimicrobial plant secondary metabolite and a major constituent of *Melaleuca alternifolia* essential oil [69]. There, low input power conditions (i.e., 7–10 W) were also found to favour the partial preservation of biochemical activity of the original monomer unit, and resulted in a substantial antimicrobial and antibiofouling activity of polyterpenol thin films. Similarly to this study, those *S. aureus* cells that managed to attach to the surface of polyterpenol were of smaller size than those attached to control or polyterpenol films fabricated at high input power. At 0.6 μm, they were also smaller than those cells attached to the surfaces of geranium oil films fabricated at the same input power conditions (at 0.8 μm). The biofilm formation was also reduced on polyterpenol samples deposited at 10 W, at an average thickness of 0.30 ± 0.04 μm, and biovolume of 0.09 ± 0.002 $\mu m^3/\mu m^2$, which is similar to the respective values of 0.35 ± 0.03 μm and 0.28 ± 0.03 $\mu m^3/\mu m^2$ observed on geranium thin films. With a similar level of activity, geranium oil presents a more attractive alternative, considering that it contains multiple constituents, and thus, may potentially target different cellular components and processes within the bacterium, thus contributing to the efficacy of the coating and potentially reducing the likelihood of bacterial resistance.

Table III.7. Comparative evaluation of bacterial attachment and retention on geranium oil-based polymer film surfaces fabricated at different RF powers.

Quantification	*S. aureus*	*P. aeruginosa*	*E. coli*
Initial cell density × 10^6, cfu mm^{-2}	19.6 ± 2.1	15.0 ± 0.9	9.2 ± 1.7
Zeta potential, mV	−33.1 ± 2.0	−15.1 ± 1.1	−39.5 ± 0.6
Cell dimensions, μm			
Control	0.9 × 0.5 × 0.3	2.2 × 1.2 × 0.4	2.7 × 1.2 × 0.3
10 W	0.8 × 0.4 × 0.2	1.7 × 1.1 × 0.3	2.3 × 1.1 × 0.2
50 W	0.9 × 0.6 × 0.4	2.1 × 1.1 × 0.4	2.6 × 1.4 × 0.2
Percentage of attached cells, %			
Control	0.39 ± 0.15	0.42 ± 0.11	0.49 ± 0.19
10 W	0.040 ± 0.002	0.070 ± 0.003	0.030 ± 0.001
50 W	0.33 ± 0.09	0.41 ± 0.15	0.35 ± 0.18
Retained cells 10^5, number of cells per mm^2			

Control	7.64 ± 1.32	6.3 ± 1.62	4.51 ± 1.29
10 W	0.78 ± 0.02	1.05 ± 0.03	0.28 ± 0.02
50 W	6.45 ± 1.45	6.15 ± 1.38	3.22 ± 1.15
Biovolume, $\mu m^3/\mu m^2$			
Control	8.92 ± 0.79	7.39 ± 0.62	8.01 ± 0.97
10 W	0.28 ± 0.03	0.23 ± 0.03	0.27 ± 0.01
50 W	7.63 ± 1.13	7.08 ± 1.02	6.03 ± 0.95
Average biofilm thickness, μm			
Control	17.19 ± 2.05	13.2 ± 1.62	11.5 ± 1.62
10 W	0.35 ± 0.03	0.42 ± 0.01	0.28 ± 0.02
50 W	15.32 ± 1.05	6.15 ± 1.38	9.22 ± 1.08

The nature of cell–surface interactions is dependent on the properties of both the pathogen cell and the surface the pathogen is trying to colonise [74]. It is well-established that the mechanism of bacterial attachment is multi-stage, involving reversible and irreversible components. When bacterial cells are separated from the surface by the distance of more than 50 nm, the interactions between the cells and the surface are nonspecific, and are determined by both the separation distance and the free energy of both entities, in particular, their respective dispersive components. Attractive forces promote cell attachment, whereas repulsive forces impede the ability of the cell to approach the surface and engage in more specific molecular or cellular interactions. Those cells that manage to successfully approach the surface (where the distance is below 5 nm) have the ability to engage in hydrogen bonding, ionic and dipole interactions, and hydrophobic interactions. These interactions are more difficult to break. To assist attachment, bacterial cells can actively express a wide range of surface-bound and free-floating polymeric structures, such as capsules, fimbriae, pili, and slime, which may facilitate cell movement toward the surface and the establishment of specific, irreversible molecular bonds with the colonised surfaces.

S. aureus cells are moderately hydrophobic, with a typical water contact angle of ~70°, whereas *P. aeruginosa* and *E. coli* cells are moderately hydrophilic, with a water contact angle of ~45° and
~35°, respectively. The surfaces of the three pathogens are negatively charged, with *E. coli* exhibiting the largest negative zeta potential ζ of −39.5 mV, followed by *S. aureus* (ζ = −33.1

mV), with *P. aeruginosa* cells characterised by the least negative zeta potential of −15.1 mV. Given that geranium oil-derived polymer films tend to donate electrons rather than accept them, some electrostatic repulsion would be expected to take place between the bacterial cells and the negatively charged polymer surface, with the strongest repulsion, and hence, weakest cell attachment, expected for *E. coli* cells. Interestingly, independent of the pathogen species, geranium oil-derived polymer surfaces were susceptible to bacterial colonisation and some biofilm formation. Conversely, polymer samples fabricated at 10 W actively repelled cell attachment irrespective of bacterial species, suggesting a more complex mechanism of antibacterial activity.

Exposure of the precursor to the highly reactive plasma environment initiates a wide range of reactions that include fragmentation, rearrangement, oligomerisation, and polymerisation. The extent of precursor fragmentation is highly dependent on the amount of energy delivered into the plasma chamber, which is in turn, directly related to the applied RF power. The dissociation is initiated by highly energetic electrons, rather than by means of thermal excitation or chemical reaction, giving rise to a unique assortment of chemically reactive species that may not be obtainable under other processing conditions. These reactive species can undergo recombination inside and outside of the plasma region, e.g., at the surface of the substrate, enabling the formation of the polymer thin film on its surface. Given the abundance of chemically-diverse species, and the presence of functional groups typically associated with conventional polymerisation, the polymerisation process follows multiple pathways, including conventional polymerisation, as well as fragment-recombination triggered by the plasma-generated and surface-attached reactive ions, and free radicals. This gives rise to a more complex polymer structure, potentially rich in free radicals trapped in a three dimensional network. The surface topography of the thus-formed polymer is influenced by the intensity of plasma-generated ion bombardment, which is again linked to the applied RF energy.

Considering the intimate link between biological activity of the surface and its surface chemistry and nanoscale topography, it is possible that the combination of these properties in polymer films fabricated at 10 W prevent bacterial fouling. Chemical characterisation showed that these surfaces bared a larger proportion of hydroxyl functional groups compared to the samples fabricated at 50 W. It has previously been shown that *S. aureus* cells preferentially attached to surfaces bearing carboxylic and methyl functional groups than those containing –OH functionality [75]. This is also supported by the thermodynamically predicted preference of hydrophobic cells for hydrophobic substrates.

III.5. Conclusions

We have synthesised and investigated the properties of geranium extract-derived polymer thin films at various fabrication powers. With increasing input power, the crosslinking of the fabricated polymers increased. The refractive index, extinction coefficient, and optical band gap were found to be not significantly dependent on the RF power. AFM images indicated that the topographical features appeared to be uniform, smooth, and pinhole free for all samples, and the surface roughness increased with an increase in the input power. The nano-indentation test revealed that the hardness and elastic modulus of the films increased with RF power deposition. The wettability of the polymer improved with input power and the polymer became more resistant to solubility in water.

Geranium extract-derived bioactive coatings have the potential to reduce and eradicate the bacterial adhesion and biofilm formation of important human pathogens. Noteworthy is that RF, in particular, played a significant role in changing the surface chemical functionality, and substantially improved the biological activity of the resulted polymer. Sample fabricated at 10 W demonstrated a remarkable reduction in the number of cells, biovolume, or biofilm thickness, while there was no significant difference in the bacterial growth between samples fabricated at 50 W and control.

Geranium plasma polymer thin films showed several advantages, including cost-effectiveness, low density, good adhesion, uniform coverage, and considerable physical stability, besides significant antibacterial properties. This data recommends that the resultant polymer coatings could be efficiently integrated as antibacterial material into medical relevant devices, to mainly minimise bacterial adhesion, and consequently, substantially reduce hospital-acquired infections.

References

1. Tamayo, L.; Azócar, M.; Kogan, M.; Riveros, A.; Páez, M. Copper-polymer nanocomposites: An excellent and cost-effective biocide for use on antibacterial surfaces. *Mater. Sci. Eng. C* **2016**, *69*, 1391–1409.
2. Knetsch, M.L.W.; Koole, L.H. New strategies in the development of antimicrobial coatings: The example of increasing usage of silver and silver nanoparticles. *Polymers* **2011**, *3*, 340–366.
3. Wu, S.; Liu, X.; Yeung, A.; Yeung, K.W.; Kao, R.Y.; Wu, G.; Hu, T.; Xu, Z.; Chu, P.K. Plasma-modified biomaterials for self-antimicrobial applications. *ACS Appl. Mater. Interfaces* **2011**, *3*, 2851–2860.
4. Lichter, J.A.; Van Vliet, K.J.; Rubner, M.F. Design of antibacterial surfaces and interfaces: Polyelectrolyte multilayers as a multifunctional platform. *Macromolecules* **2009**, *42*, 8573–8586.
5. Edmiston, C.E., Jr.; McBain, A.J.; Roberts, C.; Leaper, D. Clinical and microbiological aspects of biofilm-associated surgical site infections. In *Biofilm-Based Healthcare-Associated Infections*, 1st ed.; Springer International Publishing: Cham, Switzerland, 2015; pp. 47–67.
6. Pradeep, K.S.; Easwer, H.; Maya, N.A. Multiple drug resistant bacterial biofilms on implanted catheters—A reservoir of infection. *J. Assoc. Phys. India* **2013**, *61*, 702–707.
7. Laxminarayan, R.; Duse, A.; Wattal, C.; Zaidi, A.K.; Wertheim, H.F.; Sumpradit, N.; Vlieghe, E.; Hara, G.L.; Gould, I.M.; Goossens, H. Antibiotic resistance—The need for global solutions. *Lancet Infect. Dis.* **2013**, *13*, 1057–1098.
8. Hasan, J.; Crawford, R.J.; Ivanova, E.P. Antibacterial surfaces: The quest for a new generation of biomaterials. *Trends Biotechnol.* **2013**, *31*, 295–304.
9. Al-Jumaili, A.; Alancherry, S.; Bazaka, K.; Jacob, M. Review on the antimicrobial properties of carbon nanostructures. *Materials* **2017**, *10*, 1066.
10. Bazaka, K.; Jacob, M.V.; Crawford, R.J.; Ivanova, E.P. Plasma-assisted surface modification of organic biopolymers to prevent bacterial attachment. *Acta Biomater.* **2011**, *7*, 2015–2028.
11. Bazaka, K.; Jacob, M.; Chrzanowski, W.; Ostrikov, K. Anti-bacterial surfaces: Natural agents, mechanisms of action, and plasma surface modification. *RSC Adv.* **2015**, *5*, 48739–48759.
12. Castro, D.; Tabary, N.; Martel, B.; Gandini, A.; Belgacem, N.; Bras, J. Effect of different carboxylic acids in cyclodextrin functionalization of cellulose nanocrystals for prolonged release of carvacrol. *Mater. Sci. Eng. C* **2016**, *69*, 1018–1025.

13. Hammami, I.; Triki, M.A.; Rebai, A. Chemical compositions, antibacterial and antioxidant activities of essential oil and various extracts of *Geranium sanguineum* L. Flowers. *Sch. Res. Libr.* **2011**, *3*, 135–144.
14. Prabuseenivasan, S.; Jayakumar, M.; Ignacimuthu, S. In vitro antibacterial activity of some plant essential oils. *BMC Complement. Altern. Med.* **2006**, *6*, 39.
15. Ghannadi, A.; Bagherinejad, M.; Abedi, D.; Jalali, M.; Absalan, B.; Sadeghi, N. Antibacterial activity and composition of essential oils from *Pelargonium graveolens* L'Her and *Vitex agnus-castus* L. *Iran. J. Microbiol.* **2012**, *4*, 171–176.
16. Rosato, A.; Vitali, C.; De Laurentis, N.; Armenise, D.; Milillo, M.A. Antibacterial effect of some essential oils administered alone or in combination with norfloxacin. *Phytomedicine* **2007**, *14*, 727–732.
17. Carmen, G.; Hancu, G. Antimicrobial and antifungal activity of pelargonium roseum essential oils. *Adv. Pharm. Bull.* **2014**, *4*, 511–514.
18. Bazaka, K.; Bazaka, O.; Levchenko, I.; Xu, S.; Ivanova, E.; Keidar, M.; Ostrikov, K.K. Plasma-potentiated small molecules–possible alternative to antibiotics? *Nano Futures* **2017**.
19. Vasilev, K.; Griesser, S.S.; Griesser, H.J. Antibacterial surfaces and coatings produced by plasma techniques. *Plasma Process. Polym.* **2011**, *8*, 1010–1023.
20. Lischer, S.; Körner, E.; Balazs, D.J.; Shen, D.; Wick, P.; Grieder, K.; Haas, D.; Heuberger, M.; Hegemann, D. Antibacterial burst-release from minimal ag-containing plasma polymer coatings. *J. R. Soc. Interface* **2011**, *8*, 1019–1030.
21. Bazaka, K.; Jacob, M.V.; Ostrikov, K. Sustainable life cycles of natural-precursor-derived nanocarbons. *Chem. Rev.* **2015**, *116*, 163–214.
22. Edwards-Jones, V.; Buck, R.; Shawcross, S.G.; Dawson, M.M.; Dunn, K. The effect of essential oils on methicillin-resistant staphylococcus aureus using a dressing model. *Burns* **2004**, *30*, 772–777.
23. Hierro, I.; Valero, A.; Perez, P.; Gonzalez, P.; Cabo, M.; Montilla, M.; Navarro, M. Action of different monoterpenic compounds against *Anisakis simplex* sl L3 larvae. *Phytomedicine* **2004**, *11*, 77–82.
24. Bigos, M.; Wasiela, M.; Kalemba, D.; Sienkiewicz, M. Antimicrobial activity of geranium oil against clinical strains of *Staphylococcus aureus*. *Molecules* **2012**, *17*, 10276–10291.
25. Friedman, M.; Henika, P.R.; Levin, C.E.; Mandrell, R.E. Antibacterial activities of plant essential oils and their components against *Escherichia coli* o157: H7 and salmonella enterica in apple juice. *J. Agric. Food Chem.* **2004**, *52*, 6042–6048.
26. Jacob, M.V.; Olsen, N.S.; Anderson, L.J.; Bazaka, K.; Shanks, R.A. Plasma polymerised thin films for flexible electronic applications. *Thin Solid Films* **2013**, *546*, 167–170.

27. Ahmad, J.; Bazaka, K.; Oelgemöller, M.; Jacob, M.V. Wetting, solubility and chemical characteristics of plasma-polymerized 1-isopropyl-4-methyl-1, 4-cyclohexadiene thin films. *Coatings* **2014**, *4*, 527–552.
28. Bazaka, K.; Jacob, M.V. Solubility and surface interactions of rf plasma polymerized polyterpenol thin films. *Mater. Express* **2012**, *2*, 285–293.
29. Ivanova, E.P.; Truong, V.K.; Webb, H.K.; Baulin, V.A.; Wang, J.Y.; Mohammodi, N.; Wang, F.; Fluke, C.; Crawford, R.J. Differential attraction and repulsion of staphylococcus aureus and pseudomonas aeruginosa on molecularly smooth titanium films. *Sci. Rep.* **2011**, *1*, 165.
30. Bazaka, K.; Jacob, M.V.; Ivanova, E.P. *A Study of a Retention of Antimicrobial Activity by Plasma Polymerized Terpinen-4-ol Thin Films*; Materials Science Forum; Trans Tech Publications: Zurich, Switzerland, 2010; Volume 654, pp. 2261–2264, ISBN 978-3-319-11037-0.
31. Lis-Balchin, M. *Geranium and Pelargonium: History of Nomenclature, Usage and Cultivation*; CRC Press: London, UK, 2003.
32. Fox, A.M. *Optical Properties of Solids*; Oxford University Press: New York, NY, USA, 2001; Volume 3.
33. Ahmad, J.; Bazaka, K.; Whittle, J.D.; Michelmore, A.; Jacob, M.V. Structural characterization of γ-terpinene thin films using mass spectroscopy and x-ray photoelectron spectroscopy. *Plasma Process. Polym.* **2015**, *12*, 1085–1094.
34. Matin, R.; Bhuiyan, A. Infrared and ultraviolet–visible spectroscopic analyses of plasma polymerized 2, 6 diethylaniline thin films. *Thin Solid Films* **2013**, *534*, 100–106.
35. Zhao, X.-Y.; Wang, M.-Z.; Xiao, J. Deposition of plasma conjugated polynitrile thin films and their optical properties. *Eur. Polym. J.* **2006**, *42*, 2161–2167.
36. Alias, A.; Zabidi, Z.; Ali, A.; Harun, M.; Yahya, M. Optical characterization and properties of polymeric materials for optoelectronic and photonic applications. *Int. J. Appl. Sci. Technol.* **2013**, *3*.
37. Ahmad, J.; Bazaka, K.; Jacob, M.V. Optical and surface characterization of radio frequency plasma polymerized 1-isopropyl-4-methyl-1, 4-cyclohexadiene thin films. *Electronics* **2014**, *3*, 266–281.
38. Anderson, L.; Jacob, M. Effect of RF power on the optical and morphological properties of RF plasma polymerised linalyl acetate thin films. *Appl. Surf. Sci.* **2010**, *256*, 3293–3298.
39. Cho, S.-H.; Park, Z.-T.; Kim, J.-G.; Boo, J.-H. Physical and optical properties of plasma polymerized thin films deposited by pecvd method. *Surf. Coat. Technol.* **2003**, *174*, 1111–1115.

40. Bazaka, K.; Jacob, M. Synthesis of radio frequency plasma polymerized non-synthetic Terpinen-4-ol thin films. *Mater. Lett.* **2009**, *63*, 1594–1597.
41. Easton, C.; Jacob, M. Optical characterisation of radio frequency plasma polymerised lavandula angustifolia essential oil thin films. *Thin Solid Films* **2009**, *517*, 4402–4407.
42. Kabir, H.; Rahman, M.M.; Roy, T.S.; Bhuiyan, A. Structural and optical properties of plasma polymerized pyromucic aldehyde thin films. *Int. J. Mech. Mechatron. Eng.* **2012**, *12*, 30–34.
43. Nechache, R.; Harnagea, C.; Li, S.; Cardenas, L.; Huang, W.; Chakrabartty, J.; Rosei, F. Bandgap tuning of multiferroic oxide solar cells. *Nat. Photonics* **2015**, *9*, 61–67.
44. Kim, M.; Cho, S.; Han, J.; Hong, B.; Kim, Y.; Yang, S.; Boo, J.-H. High-rate deposition of plasma polymerized thin films using pecvd method and characterization of their optical properties. *Surf. Coat. Technol.* **2003**, *169*, 595–599.
45. Vassallo, E.; Cremona, A.; Ghezzi, F.; Dellera, F.; Laguardia, L.; Ambrosone, G.; Coscia, U. Structural and optical properties of amorphous hydrogenated silicon carbonitride films produced by PECVD. *Appl. Surf. Sci.* **2006**, *252*, 7993–8000.
46. Araújo, E.A.; de Andrade, N.J.; da Silva, L.H.M.; de Carvalho, A.F.; de Sá Silva, C.A.; Ramos, A.M. Control of microbial adhesion as a strategy for food and bioprocess technology. *Food Bioprocess Technol.* **2010**, *3*, 321–332.
47. Whitehead, K.A.; Colligon, J.; Verran, J. Retention of microbial cells in substratum surface features of micrometer and sub-micrometer dimensions. *Colloids Surf. B Biointerfaces* **2005**, *41*, 129–138.
48. Kuo, S.-Y.; Liu, K.-C.; Lai, F.-I.; Yang, J.-F.; Chen, W.-C.; Hsieh, M.-Y.; Lin, H.-I.; Lin, W.-T. Effects of RF power on the structural, optical and electrical properties of Al-doped zinc oxide films. *Microelectron. Reliab.* **2010**, *50*, 730–733.
49. Thirumoorthi, M.; Prakash, J.T.J. Structure, optical and electrical properties of indium tin oxide ultra thin films prepared by jet nebulizer spray pyrolysis technique. *J. Asian Ceram. Soc.* **2016**, *4*, 124–132.
50. Gadelmawla, E.; Koura, M.; Maksoud, T.; Elewa, I.; Soliman, H. Roughness parameters. *J. Mater. Process. Technol.* **2002**, *123*, 133–145.
51. Kim, H.-Y. Statistical notes for clinical researchers: Assessing normal distribution (2) using skewness and kurtosis. *Restor. Dent. Endod.* **2013**, *38*, 52–54.
52. Bazaka, K.; Jacob, M.V.; Bowden, B.F. Optical and chemical properties of polyterpenol thin films deposited via plasma-enhanced chemical vapor deposition. *J. Mater. Res.* **2011**, *26*, 1018–1025.
53. Tien, C.-L.; Lyu, Y.-R.; Jyu, S.-S. Surface flatness of optical thin films evaluated by gray level co-occurrence matrix and entropy. *Appl. Surf. Sci.* **2008**, *254*, 4762–4767.

54. Volinsky, A.A.; Moody, N.R.; Gerberich, W.W. Nanoindentation of au and Pt/Cu thin films at elevated temperatures. *J. Mater. Res.* **2004**, *19*, 2650–2657.
55. Jacob, M.V.; Bazaka, K.; Taguchi, D.; Manaka, T.; Iwamoto, M. Electron-blocking hole-transport polyterpenol thin films. *Chem. Phys. Lett.* **2012**, *528*, 26–28.
56. Bazaka, K.; Jacob, M.V.; Taguchi, D.; Manaka, T.; Iwamoto, M. Investigation of interfacial charging and discharging in double-layer pentacene-based metal-insulator-metal device with polyterpenol blocking layer using electric field induced second harmonic generation. *Chem. Phys. Lett.* **2011**, 503, 105–111.
57. Liu, M.; Lu, C.; Tieu, K.; Yu, H. Numerical comparison between berkovich and conical nano-indentations: Mechanical behaviour and micro-texture evolution. *Mater. Sci. Eng. A* **2014**, *619*, 57–65.
58. Zhao, M.; Xiang, Y.; Xu, J.; Ogasawara, N.; Chiba, N.; Chen, X. Determining mechanical properties of thin films from the loading curve of nanoindentation testing. *Thin Solid Films* **2008**, *516*, 7571–7580.
59. Srinivasan, S.; McKinley, G.H.; Cohen, R.E. Assessing the accuracy of contact angle measurements for sessile drops on liquid-repellent surfaces. *Langmuir* **2011**, *27*, 13582–13589.
60. Stalder, A.F.; Melchior, T.; Müller, M.; Sage, D.; Blu, T.; Unser, M. Low-bond axisymmetric drop shape analysis for surface tension and contact angle measurements of sessile drops. *Colloids Surf. A Physicochem. Eng. Asp.* **2010**, *364*, 72–81.
61. Rupp, F.; Gittens, R.A.; Scheideler, L.; Marmur, A.; Boyan, B.D.; Schwartz, Z.; Geis-Gerstorfer, J. A review on the wettability of dental implant surfaces I: Theoretical and experimental aspects. *Acta Biomater.* **2014**, *10*, 2894–2906.
62. Tandjaoui, A.; Cherif, M.; Carroz, L.; Sanchez, J.; Reboud, R.; Garnier, C.; Duffar, T. Investigation of liquid oxide interactions with refractory substrates via sessile drop method. *J. Mater. Sci.* **2016**, *51*, 1701–1712.
63. De Souza, E.; Brinkmann, M.; Mohrdieck, C.; Crosby, A.; Arzt, E. Capillary forces between chemically different substrates. *Langmuir* **2008**, *24*, 10161–10168.
64. Wang, Y.; Sang, D.K.; Du, Z.; Zhang, C.; Tian, M.; Mi, J. Interfacial structures, surface tensions, and contact angles of diiodomethane on fluorinated polymers. *J. Phys. Chem. C* **2014**, *118*, 10143–10152.
65. Belibel, R.; Avramoglou, T.; Garcia, A.; Barbaud, C.; Mora, L. Effect of chemical heterogeneity of biodegradable polymers on surface energy: A static contact angle analysis of polyester model films. *Mater. Sci. Eng. C* **2016**, *59*, 998–1006.

66. Fahmy, A.; Mix, R.; Schönhals, A.; Friedrich, J. Surface and bulk structure of thin spin coated and plasma-polymerized polystyrene films. *Plasma Chem. Plasma Process.* **2012**, *32*, 767–780.
67. Easton, C.D.; Jacob, M.V. Solubility and adhesion characteristics of plasma polymerized thin films derived from lavandula angustifolia essential oil. *J. Appl. Polym. Sci.* **2010**, *115*, 404–415.
68. Bhattacharyya, D.; Xu, H.; Deshmukh, R.R.; Timmons, R.B.; Nguyen, K.T. Surface chemistry and polymer film thickness effects on endothelial cell adhesion and proliferation. *J. Biomed. Mater. Res. Part A* **2010**, *94*, 640–648.
69. Bazaka, K.; Jacob, M.V.; Truong, V.K.; Crawford, R.J.; Ivanova, E.P. The effect of polyterpenol thin film surfaces on bacterial viability and adhesion. *Polymers* **2011**, *3*, 388–404.
70. Arima, Y.; Iwata, H. Effect of wettability and surface functional groups on protein adsorption and cell adhesion using well-defined mixed self-assembled monolayers. *Biomaterials* **2007**, *28*, 3074–3082.
71. Wang, S.; Zhang, Y.; Abidi, N.; Cabrales, L. Wettability and surface free energy of graphene films. *Langmuir* **2009**, *25*, 11078–11081.
72. Wu, S.; Shanks, R. Solubility study of polyacrylamide in polar solvents. *J. Appl. Polym. Sci.* **2004**, *93*, 1493–1499.
73. Weng, M.; Shen, Q. Solid surface tension components and their error limits induced by contact angle measurement in application of the van Oss–Chaudhury–Good approach. *J. Adhes. Sci. Technol.* **2013**, *27*, 2571–2591.
74. Crawford, R.J.; Ivanova, E.P. *Superhydrophobic Surfaces*. Elsevier: Amsterdam, The Netherlands, 2015; ISBN:978-0-12-801109-6.
75. Tegoulia, V.A.; Cooper, S.L. *Staphylococcus aureus* adhesion to self-assembled monolayers: Effect of surface chemistry and fibrinogen presence. *Colloids Surf. B Biointerfaces* **2002**, *24*, 217–228.

Chapter IV

Nanocomposite Films Derived From Geranium Oil and Zinc Oxide

This chapter reports the fabrication and characterizations of nanocomposite films manufactured from geranium essential oil and the thermal decomposition of $Zn(acac)_2$ in one step hybrid-plasma system. The chemical composition, surfaces characteristics, antimicrobial performance and metal release of the fabricated nanocomposite are systematically investigated.

This chapter was published as:

Al-Jumaili, A.; Mulvey, P.; Kumar, A.; Prasad, K.; Bazaka, K.; Warner, J.; Jacob, M.V. Eco-friendly nanocomposites derived from geranium oil and zinc oxide in one step approach. *Scientific Reports* **2019**, *9*, 5973.

Abstract

Nanocomposites offer attractive and cost-effective thin layers with superior properties for antimicrobial, drug delivery and microelectronics applications. This work reports single-step plasma-enabled synthesis of polymer/zinc nanocomposite thin films via co-deposition of renewable geranium essential oil-derived polymer and zinc nanoparticles produced by thermal decomposition of zinc acetylacetonate. The chemical composition, surfaces characteristics and antimicrobial performance of the designed nanocomposite were systematically investigated. XPS survey proved the presence of ZnO in the matrix of formed polymers at 10 W and 50 W. SEM images demonstrated that the average size of ZnO nanoparticle slightly increased with an increase in the power of deposition from approximately 60 nm at 10 W to approximately 80 nm at 50 W. Confocal scanning laser microscopy images showed that viability of *S. aureus* and *E.coli* cells significantly reduced on surfaces of ZnO/composites compare to pristine polymers. The release of ZnO nanoparticle from the composite thin films was confirmed using ICP measurements, and can be further controlled by coating the film with thin polymeric layer. These eco-friendly nanocomposite films could be employed as encapsulation coatings to protect relevant medical devices surfaces from microbial adhesion and colonization.

IV.1. Introduction

There has been an increased interest in the functionalizing of sustainable resources-derived polymers via incorporation of metallic nanoparticles, where the intrinsic properties of the nanoparticles are contributed into that polymer[1]. The resultant 'eco-friendly composites' combine the advantages of low-dimensional organic layers with an enormous specific surface area of nanoparticles, creating a wide range of promising applications in science and manufacturing[2]. These composites are versatile, potentially biodegradable, and their polymer

can be derived from a wide variety of possible renewable precursors such as oxygen-rich monomers, and hydrocarbon-rich monomers[3, 4]. Intelligent use of eco-friendly nanocomposites have the potential to reduce the growing impact of modern day technology on ecosystems (e.g. pollution and waste disposal) while sustaining the development of nanotech-driven applications.

The potential to modify chemical, physical and/or bio-responsive properties of solid surfaces (e.g. medical devices and implants) without affecting their bulk properties is the key utilization of composite thin films in electronics, biomaterials, and other relevant industries [5, 6]. In particular, nanocomposites could be effectively employed as antibacterial coatings, where the metal nanoparticles are incorporated into a thin layer of polymer, providing a high platform for active particles to interact with microorganisms. The main benefit of these composites is the extremely low quantity of selected nanoparticles required to achieve desired outcomes due to powerful antimicrobial properties of metal nanoparticles [7].

Plasma polymerization is one of the rapidly advancing techniques for deposition of smooth, uniform, organic thin films from naturally-available alternatives (e.g. essential oils and herb extracts) on different substrates [8]. Essential oil-based coatings prepared by plasma polymerization display a wide range of desired properties, such as impart biocompatibility, optical transparency, moderate hydrophilicity and low post-annealing retention [9]. These films have found a host of applications in biomaterials (e.g. biocompatible and antimicrobial surfaces) and electronics (e.g. superior organic and hybrid devices)[10, 11]. However, plasma systems can be adapted to introduce inorganic particles in the structure of the polymer matrix as the latter is formed [12, 13], where the chemical reaction in the gas-phase and the nucleation/growth of nanoparticles take place simultaneously. Consequently, plasma-formed composite materials comprise inorganic particles and their clusters trapped within a highly cross-linked polymer matrix consisting of short polymeric chains that are randomly branched and terminated. Nevertheless, it is interesting to note that there is no systematic study, in the literature, investigates nanocomposite plasma films derived from essential oils and inorganic nanoparticles.

Among various metals, zinc oxide nanoparticles have an attractive set of properties that include a powerful antibacterial performance against a variety of pathogenic microorganisms, high luminous transmittance chemical/physical stability and excellent catalytic activity [14-16]. Furthermore, zinc oxide is relatively low cost, available in commercial quantities and can take several morphological forms (e.g. spherical particles, nano-rode, etc). While there are various physical/chemical methods to produce nano-sized zinc oxide, thermal decomposition of zinc acetylacetonate ($Zn(acac)_2$) is known to generate zinc oxide nanoparticles of different size and morphology [17-20]. This process can be integrated with a plasma polymerization system to enable *in situ* functionalization of the polymer (during chains formation) in the absence of

catalyst. Also, it allows for a wide variety of metals and organic precursors to be combined, and guarantees a minimum contamination rate.

This paper reports the fabrication and characterizations of nanocomposite films produced using a single-step approach that combines simultaneous plasma polymerization of renewable geranium essential oil with thermal decomposition of $Zn(acac)_2$. To best of our knowledge, this is first study on the functionalization of geranium plasma thin polymers with inorganic nanoparticles toward producing eco-friendly materials.

IV.2. Materials and methods

IV.2.1. Precursors

Geranium essential oil was nominated because it is highly volatile at room temperature, where no external heating system nor carrier gases are required to transport the precursor molecules to the spot of fabrication. Moreover, geranium oil possesses strong antibacterial activity toward gram-negative and gram-positive bacteria, which under certain polymerization conditions can be retained in the fabricated films.

Geranium essential oil was obtained from Australian Botanical Products (ABP, Victoria, Australia). As mentioned by the manufacturer, this geranium oil is extracted through steam distillation process from leaves of *Pelargonium graveolens.* The oil contains citronellol (32%), geraniol (15%), linalool (6%), isomenthone (6%), geranyl formate (2.5%), tiglate (2%), citronellyl formate (6%), guaia-6,9-diene, and 10-epi-γ eudesmol (5%), as well as trace amounts of other secondary plant metabolites. Geranium oil was used without further modification in all experiments.

Zinc acetylacetonate hydrate powder obtained from Sigma-Aldrich (Germany) was used (without further purification) as zinc precursor. $Zn(acac)_2$ was selected due to its relatively low decomposition temperature, which made it possible to integrate gas-phase catalyst-free nanoparticle nucleation and synthesis with plasma polymerisation. By comparing with other procedures, for example, Ao et al heated $ZnCl_2$ and Na_2CO_3 from 400 to 800 °C to create ZnO NPs varying from 18 m to 36 nm, respectively [21]. Yao et al used thermal evaporation process of ZnO powder to produces several ZnO-nanostructures at 500 to 800 °C [22]. Paéz et al operated thermal treatment of zinc acetate dihydrate precipitates at 320°C, creating ZnO NPs ranging around □50 nm of [23].

IV.2.2. Thin films synthesis

Microscope glass slides (76 mm × 26 mm) and round cover-glass sheets (d = 19 mm) were sonicated in a solution of water and commercial decon for 20 min, then washed with distilled

water and rinsed in acetone and propan-2-ol, and finally dried using an air gun. Plasma polymerization was carried out in a cylindrical glass tube (*l*: 80 cm, *d*: 5 cm) fitted with two external parallel copper rings, which were used as electrodes connected to a generator through a matching network. A radio frequency generator model ACG-3B (MKS Instruments, Andover, MA, USA) was operated in a continuous wave mode (13.56 MHz) to create a glow discharge. The distance between electrodes and the distance between monomer and the electrodes were optimized to achieve the optimum plasma stability. Prior to each fabrication, the reactor tube was evacuated to pressure of 0.2 mbar utilizing a double stage rotary pump (JVAC–DD150, Victoria, Australia). Furthermore, the monomer flow rate (*F*) was estimated using the relation 1, derived from the ideal gas formula [24]:

$$F = \frac{dp}{dt} \times 16172 \ \frac{V}{T} \text{.....(1)}$$

where *p* is the pressure inside the plasma tube (mbar), *t* is time (s), *V* is the volume of the plasma tube (L), and *T* is the ambient temperature (K). In the beginning, the tube was evacuated to 0.2 mbar, then the monomer gas was released into the tube until the pressure reached a stable value, at which point the outlet valve was locked, and the pressure was measured every 5 s for 1 min. It was calculated the geranium flow rate to be 16.22 cm^3/min. The input radio frequency power used for the deposition of pristine polymers were 10 W and 50 W for 20 minutes, with the resulting films abbreviated as Ge 10 W and Ge 50 W, respectively.

In the case of composite fabrication, the plasma polymerization tube was supplemented with an external ceramic fiber heater, where $Zn(acac)_2$ powder (0.05 g) was placed in a ceramic boat inside the plasma tube and heated up to 200°C, as seen in fig IV.1. The $Zn(acac)_2$ vapor was carried into the fabrication zone (i.e. where substrates were located) by the flow of geranium vapors in the direction from the flask to the pump outlet. ZnO nanoparticles were formed in the gas phase and imbedded into the polymer matrix during the growth of the latter. The input power used for the deposition of all composites were 10 W and 50 W for 20 minutes, and the resulting composite structures were abbreviated as Zn/Ge 10 W and Zn/Ge 50 W, respectively.

The coating thickness of pristine and composites films were around 500 nm, yet the thickness of composites my slightly varied due to presence of nanoparticles on the surface.

In order to investigate the release of zinc from the composites, ultra-layers of 25 nm and 50 nm were coated on the surface of Zn/Ge 10 W and Zn/Ge 50 W. The films were fabricated substrates, and coatings thickness were identified using Variable Angle Spectroscopic Ellipsometry (JA Woollam-M2000 D, Lincoln, NE, USA). The thickness was controlled by optimizing the time of deposition, where 60 sec and 100 sec yield approximately 25 nm and 50 nm. The flow rate of geranium oil was kept 16.22 cm^3/min during the ultra-layers coating.

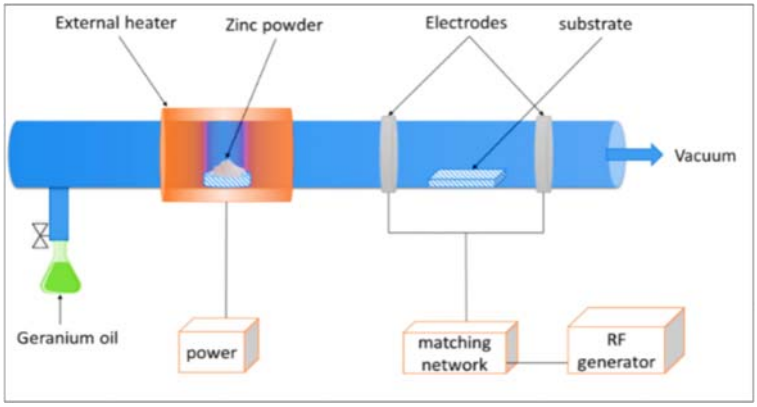

Figure IV.1. Plasma polymerization system equipped with an external heater for thermal decomposition of metallic powders.

IV.3. Material Characterization

IV.3.1. Chemical composition

X-ray photoelectron spectroscopy (XPS) spectrum was obtained by Specs SAGE 150 spectroscope supplemented with a monochromatic Al Kα X-ray source ($h\upsilon$ = 1486.6 eV). The measurements were collected at a take-off angle 90° from a circular area of a diameter of ~ 5 mm. With the intention to reduce X-ray-induced polymer degradation, the exposure time was adjusted to the minimum required to achieve a sufficient signal-to-noise ratio. Surface charging effects of the samples were addressed by a reference value of 285.0 eV, which is the binding energy of C1s peak originating from neutral hydrocarbon (CH_x). The elements concentrations were estimated using Casa XPS software.

IV.3.2. Surface characteristics

Scanning Electron Microscopy (SEM) (SU5000, Hitachi, Canada) with Energy Dispersive X-ray Spectroscopy (EDS) were used to study surface properties of the fabricated films. Films were fabricated on nickel foil, a conductive substrate, to avoid the scattering from glass substrates. Data were acquired at Vacc = 3.0kV, EC= 115K nA, WD=6.1mm, and high vacuum atmosphere.

Surface characteristics were also investigated by employing a low-noise scanning/high-resolution atomic force microscope AFM (NT-MDT NTEGRA, Moscow, Russian Federation) in the tapping mode, with a scanning area of 10 μm × 10 μm. For all samples, data were acquired under ambient conditions. Then, the data were analyzed using Nova software (Version 1.0.26, Moscow, Russia), with the fitting correction value (polynomial order of 4).

Static contact angle measurements were recorded to determine the wettability of resultant films. A drop of double distilled water was gently dispensed onto the surface of samples with a micro-syringe. Water drop contact angles were calculated using data collected by means of a goniometer (KSV CAM 101, Helsinki, Finland), where a minimum of five measurements per sample were collected. In order to reduce inaccuracies in the obtained data, the size of the droplet was carefully selected in the range of: volume (V) ≈ 2.5 μL, area (A) ≈ 9.0 mm^2, height (H) ≈ 0.85 mm, and diameter (2a) ≈ 3.0 mm.

IV.3.3. Bacterial Studies

The antibacterial activity of the pristine and composite films was determined by Live/Dead staining method using gram-negative *Escherichia coli* and gram-positive *Staphylococcus aureus*. These pathogens are a well-known source of infections in hospitals and implantable devices.

For each experiment, a fresh suspension was prepared by first refreshing the frozen stock culture (1 mL) in Oxoid nutrient broth (10 mL) at 37 °C and shaking at 120 rpm. A spectrometer (The SPECTROstar Nano, BMG labtech, Germany) was employed to calculate cell numbers in a bacterial suspension prior to placing them onto polymer surfaces. The cell density was adjusted to (OD_{600} = 0.1) to ensure uniform starting culture (2 ×10^5 CFU/mL).

The experiment was run in triplicate. Polymer-coated glass slides (d = 19 mm) and controls (uncoated glass slides) were placed into 12-well plates, and an aliquot of 2 ml of bacterial suspension at concentration of 2 ×10^5 CFU/mL was placed onto the sample surface. All samples were incubated at 37 °C and 5% CO_2 for 24 h.

After the incubation time, a staining kit (SYTO™ Invitrogen, Thermo Fisher, USA) was used to study live/dead bacterial cells. The dyes were applied following the protocol outlined in[25]. Prior to imaging, bacterial suspensions were removed from the samples. Then, 90 μl of the stain were placed on top of each sample and kept in the dark. After 20 min, samples were gently washed with 2 ml of distilled water to remove unattached cells. From that moment, fluorescent images were obtained with a confocal scanning laser microscope (LSM 800, ZEISS, Germany), where green and red colors were indicative of live and non-viable cells, respectively. Viability was calculated as the percentage of viable, adhering bacteria relative to the total number of attached bacteria to the surface.

All data were acquired with a minimum of three replicates each. The standard error of the mean was calculated to define variance about the mean. Statistical analysis of numerical data was determined using a paired t-test. Statistical significance (*) was considered at $p < 0.05$. Furthermore, a confidence interval (95%) was given at each time point, and was used as an additional pathway to ensure statistical differences between experimental and control data.

IV.3.4 Zinc release in aquatic medium

In order to adjust the zinc release, Zn/Ge composite films were coated by an extra thin layer (25 ± 5 and 50 ± 5 nm) of geranium film, as seen in fig IV.2. The releasing rate was measured using inductively coupled plasma-mass spectrometer (ICP-MS 820, Varian, USA). Films were fabricated on glass cover slips and immersed into water. In order to stay well below saturation, the volume of water added to all samples was set to be 5 ml, and incubation took place at 22 °C in a dark condition. After coatings with the extra layer, samples were incubated with water for 1, 4, 8, 16, 20, 24, 28, 32, 36, and 40 h, and afterwards analyzed by ICP. The calibration was performed using double distilled water as a reference, and zinc concentration <=5 µg /L.

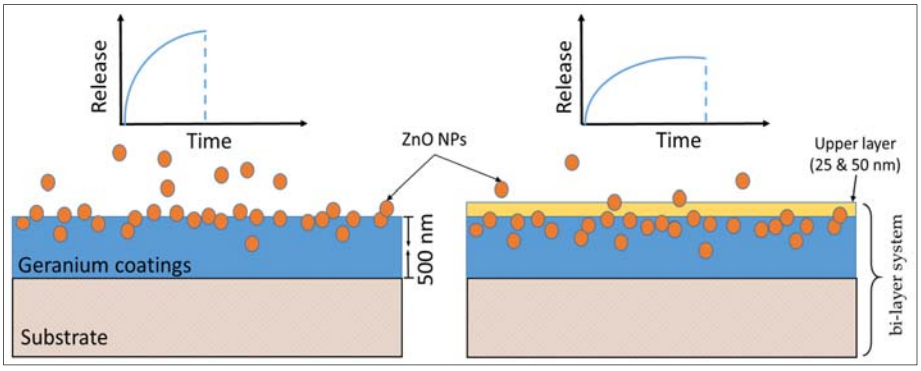

Figure IV.2. Schematic of the cross-section of the ZnO/geranium plasma polymer composite films.

IV.4. Results and discussion

IV.4.1. Compositional studies

Full scan XPS spectra of pristine and composite thin films are presented in fig IV.3. The binding energies were calibrated within an accuracy of 0.1 eV using C1s (284.6 eV). The obtained peaks were resolved using the CasaXPS software. The spectrum for pristine polymer shown in fig IV.3 (a) displays the presence of carbon and oxygen at strong peaks at 282 and 531 eV, respectively. The C 1s peaks for geranium polymers were fitted with four peaks, which can be ascribed to major hydrocarbon C–C/C–H (BE = 284.9 eV), and other functional groups, such as ether C–O

(BE = 286.2 eV), carbonyl C=O (BE = 287.5 eV), and ester O–C=O (BE = 288.9 eV), as seen in fig IV.3 (c).

The spectrum in fig IV.3 (b) demonstrates the presence zinc in the composite structure, along with carbon, oxygen, and nitrogen. No major chemical shifts or asymmetry in the C 1s and O 1s peaks could be observed for the composite when compared to pristine polymers. Nevertheless, the presence of 2p ($2p_{3/2}$ and $2p_{1/2}$) symmetrical zinc oxide binding energies (at 1021.32 and 1044.60 eV) is apparent. Zinc oxide had significantly split spin-orbit components Δ_{metal}=23 eV, as seen in fig IV.3 (d). Furthermore, a minor peak was also observed at 400.08 eV, attributed to nitrogen. This peak most likely originates from impurities within the $Zn(acac)_2$ precursor, as noted in previous studies[26].

Atomic fractions were also calculated and presented in table IV.1, where carbon was identified to be the main element which contributed up to 85 % of the total atomic concertation for samples. Oxygen was identified as a second most abundant element in the films. No impurities were identified for any of the pristine polymers.

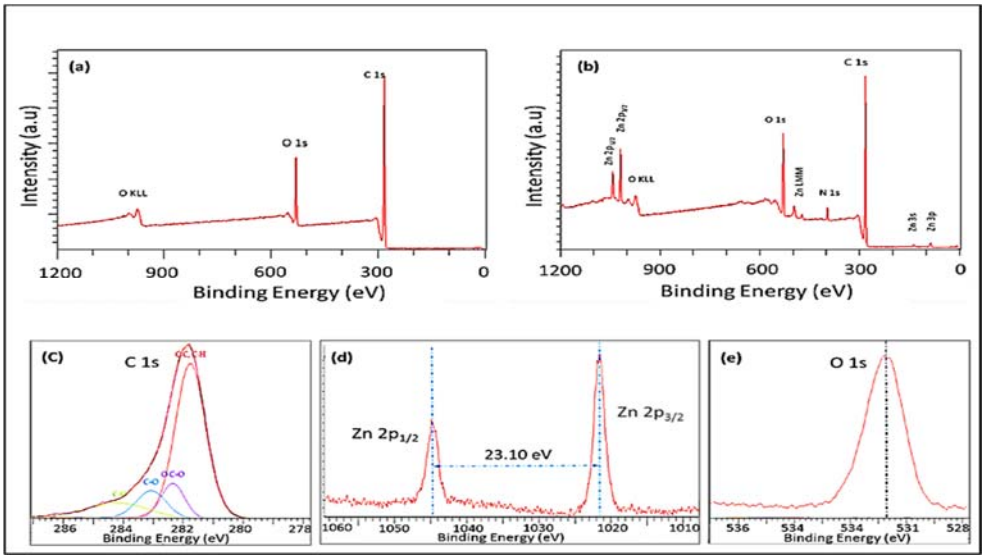

Figure IV.3. Full scan XPS spectrum of pristine polymer (a) and composite (b) thin films. The carbon C 1s binding energy of the pristine polymer is given in (c). The 2p symmetrical zinc oxide binding energies are shown in (d). O 1s binding energy for the composite is presented in (e).

On the other hand, the atomic concentrations for the composites were slightly varied. Carbon was identified to be around 80 %, while oxygen was above 13.00 %. Zinc was shown 0.79 % and 1.57% for samples fabricated at 10 W and 50 W, respectively. It is evident that carbon percentage in the composites decreased with an increase in the power of deposition, which was in contrast to the trend observed in the pristine counterparts. The most rational elucidation for this observation is that the higher input power resulted in a higher fragmentation/dissociation of the zinc

acetylacetonate, accompanied by the loss of hydrocarbon groups owing to increased ion bombardment, causing a relative increase in oxygen, nitrogen and zinc quantities.

As geranium oil vapor has various chemical components, it is possible that the resulting plasma polymer structures will contain a trace amount of un-fragmented geranium molecules and/or radicals. Those un-fragmented molecules, especially occur at low plasma power, trapped within the polymer may elute over time with the potential to retard microbial attachment on the surface[27]. In addition, un-fragmented geranium molecules (involving aromatic acyclic monoterpene alcohols) different reactions with adjacent zinc nanoparticles could be occurred. For example, formation of zinc oxidants during polymerization can result in oxidation of alcohol moieties to ketones. The presence of long chains of alcohols may marginally increase the size of formed ZnO[28].

Zinc could also exist in the form of zinc ions complexed with acetylacetonate moieties[29]. It is known that the presence of metallic particles with large surface areas would change the local stress state of the surrounding matrix. Thus, the polymer chain dynamics in the vicinity of particles could be significantly altered compared to the pristine counterparts owing to specific nanoparticle–polymer interactions[30].

Table IV.1. Atomic percentages of pristine and zinc-polymer composite materials fabricated at 10 W and 50 W.

Sample	**Atomic percentages (%)**			
	C 1s	O 1s	N 1s	Zn 2p
Ge 10 W	85.46	14.45	-	-
Ge 50 W	87.80	12.20	-	-
Zn/Ge 10 W	83.35	13.00	2.87	0.79
Zn/Ge 50 W	78.33	16.86	3.29	1.57

IV.4.2. Surface characteristics

IV.4.2.1. Scanning electron microscopy

Typical scanning electron microscope (SEM) images were obtained in order to determine the size and morphology of the formed nanoparticles in the polymer matrix, as seen in the fig IV.4. It is known that at relatively high temperatures typical of solid–vapor deposition methods, the growth conditions play a crucial role in the properties of resultant nanoparticles, where the morphology, shape and size could be significantly varied by altering parameters of the process[31, 32]. The growth conditions of this study created ball-like nanoparticles that are clearly seen in all composites. ZnO particles were evenly distributed in the polymer medium. No significant

morphological differences were observed between composites fabricated at 10 W and 50 W. However, the size of ZnO particles slightly increased with an increasing power of deposition. The average particle size increased with the input power from approximately 60 nm at 10 W to approximately 80 nm at 50 W. The increase in particle size is in agreement with other studies on plasma polymers and metallic nanoparticles[33, 34]. This indicates that a greater quantity of zinc can be incorporated into the polymer films at higher power of deposition, agreeing well with the XPS data.

It is known that the cohesive energy of metals is typically higher (by two orders of magnitude) than the cohesive energy of polymers, which promote a tendency for physical aggregations of metal atoms present within polymers[35]. These aggregations further increase by the very weak interaction between metals and polymers compared to strong metal–metal binding forces[1]. When active metal atoms insert attach to the polymer, they go through various events, such as diffusion into the bulk, random rolling on the surface, or desorption. In the process of their diffusion across the polymer surface, metal atoms could be captured by surface cracks or encounter other metal atoms or particles, thereby forming aggregations and stable metal clusters. These accumulations are presented in the polymer structure during formation of the nanocomposite film. Here, we observed some of these unavoidable particle aggregations, representing less than 10 % of the total number of nanoparticles. The EDX data in fig IV.4 (e) further confirmed the presence of zinc in all composites, at peaks of 1.01, 8.63, and 9.57 keV. Peaks attributed to carbon and oxygen appeared at 0.27 and 0.52 keV, respectively. Nickel peaks were detected at 0.84 and 7.48 keV, representing the underlying substrate.

It is worth to mention that thermal decomposition of zinc acetylacetonate hydrate (Zn $(C_5H_7O_2)_2 \cdot xH_2O$) was also reported to form metallic zinc[26], and zinc oxide[36, 37]. The quantity, chemical state, particle size, and morphology of the formed zinc nanoparticles could vary considerably depending on the fabrication conditions[38]. However, this decomposition approach has a complex mechanism, with the bulk of transformations taking place when the material is heated above 130 °C. Indeed, the presence of H_2O molecules in $Zn(acac)_2$ structure, makes the breakdown process more complicated[39]. Water probably enhances the thermal decomposition by attacking oxygen of the carbonyl groups in acetylacetonate, and/or starting a direct reaction with zinc[39]. Arii *et al.* suggested that the thermal process is initiated with a single-step dehydration at ~110°C, followed by complex sequential and parallel reactions, including phase transition, fusion, evaporation, and breakdown of anhydrous zinc acetylacetonate. The following formula describes thermal decomposition of acetylacetonate hydrate [40]:

$$Zn(CH_3COCHCOCH_3)_2 . H_2O \rightarrow ZnO + 2CH_3COCH_2COCH_3$$

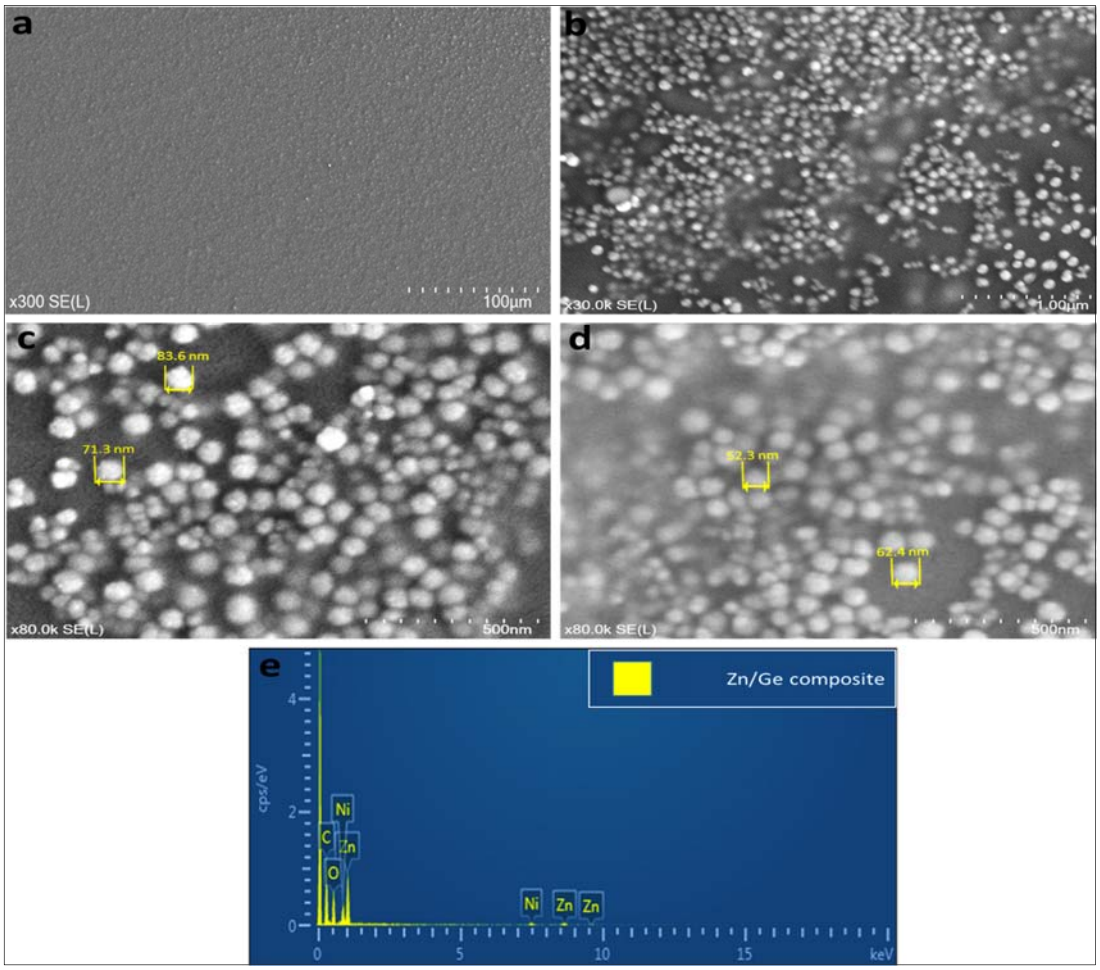

Figure IV.4. Typical SEM images of Zn/Ge 10 W composites at different magnifications, (a) is x300; and (b) is x30K. SEM images of (c) and (d) represent Zn/Ge 50 W and Zn/Ge 10 W, respectively; (e) shows EDX spectrum of the composite fabricated on Nickle substrates. SEM images were acquired at conditions of: Vacc = 3.0kV, EC= 115K nA, and WD=6.1mm.

IV.4.2.2 Atomic force microscopy

The surface morphology of the pristine and composite films was inspected by atomic force microscopy (AFM) using tapping mode atomic force microscopy (due to soft geranium polymer surface) and the results are summarized in table IV.2. As can be clearly observed in fig IV.5 (a), the surface of the pristine polymer was smooth and uniform, with an average particle roughness of around 0.25 nm. As might be expected, the average roughness parameter significantly increased upon incorporation of zinc material, measuring at 33.7 ± 2.1 and 37.2 ± 2.4 nm for 10 W and 50 W respectively. The rather high surface roughness in fig IV.5 (b) in comparison with the pristine film indicates that the composite exposes porous surface with random distribution of ZnO particles. The symmetry of the deviations of a surface profile can be well-defined by using surface skewness parameter, since it is sensitive to the irregularity of high peaks or deep grooves.

A clear increase in the values of the surface skewness can be observed in composite films comparing to pristine films. This probably relates to the presence of zinc nanoparticles on the surfaces of the films in the form of protrusions. In order to describe the distribution of these protrusions with respect to the mean line, surface kurtosis value can be employed. For an identical protrusion distribution, the kurtosis is zero. The positive values of kurtosis indicates a high peak-type distribution (leptokurtic), while negative kurtosis refers to a flat-topped distribution (platykurtic). All composites showed high positive kurtosis values (coefficient of kurtosis ~ 2) indicating that the surfaces were dominated by high peaks.

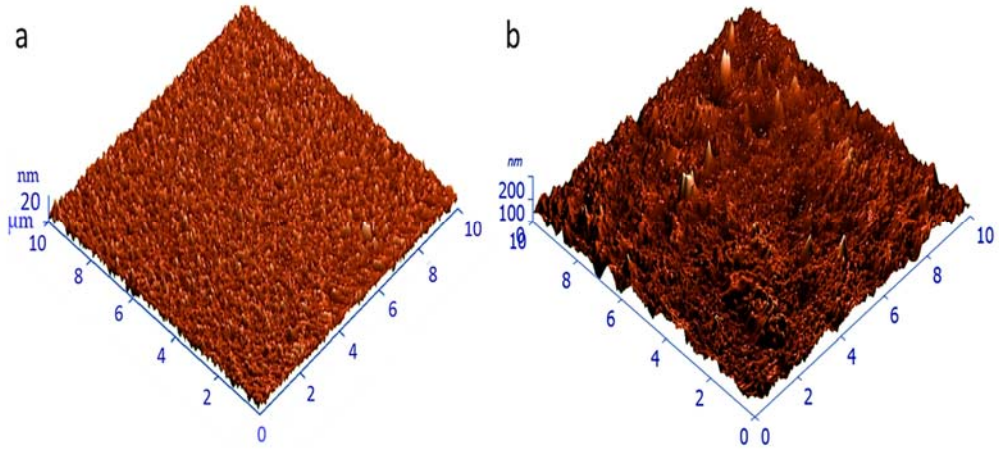

Figure IV.5. Three-dimensional AFM image of (a) pristine geranium polymer films, and (b) zinc/composites films. The scanning area of both images is 10 µm × 10 µm.

Table IV.2. Surface profiles of 10 µm × 10 µm of pristine geranium film surfaces and zinc/composite films fabricated at various 10 W and 50 W power.

Sample	**Ge 10 W**	**Ge 50 W**	**Zn/Ge 10 W**	**Zn/Ge 50 W**
Max, (nm)	3.75	3.52	363.3	385.1
Average Roughness, (nm)	0.23	0.30	33.7	37.2
Root Mean Square, (nm)	0.30	0.38	45.5	44.7
Surface skewness,	0.08	0.04	1.00	0.94
Coefficient of kurtosis	0.55	0.03	2.12	2.04
Entropy	3.45	3.80	1.54	2.70

IV.4.2.3. Water contact angle

Wettability of the polymeric surface is an essential property that is mainly determined by the chemical composition and morphological structure of the surface. The static water contact angles of pristine and composite geranium films are shown in fig IV.6. An increase in the main contact angle from 54.0 ° to 61.2 ° can be observed for pristine samples fabricated in 10 W and 50 W respectively.

In the case of pristine polymers, plasma fabrication at higher input power conditions produces polymers with highly crosslinked structures due to more fragmentation/dissociation of precursor molecules. This results in the formation of relatively more-rigid polymers as a result of an increase in the bonding interconnection and dense packing of polymer chains within the matrix, minimizing the absorption of water on the surface. This may lead to an increase in the contact angle value, verifying the dependence of contact angle on the degree of crosslinking. Moreover, the increase in the input power affects surface chemistry of the polymers, specifically a decrease in the oxygen content, resulting in a decrease in the polarity of the polymers surfaces. XPS data showed a reduction in oxygen quantity in the films produced at a higher RF power. Studies in the literature reported an increase in the contact angle values when the input power was increased [41, 42].

In the case of composite Zn/Ge films, samples fabricated at 50 W revealed higher contact angle values, at approximately 73.4 °, compared to that of samples fabricated at 10 W, at approximately 66.4 °. This probably is related to the difference in the size of formed nanoparticles at a different power of deposition. It had been previously reported that contact angles of ZnO nanoparticles are higher for larger particle sizes and lower as the particle size is reduced[43]. This agreed well with our findings, where composites fabricated at 50 W comprise larger nanoparticles, while composites fabricated at 10 W showed nanoparticles of smaller sizes. Furthermore, an increase in the contact angle can be understood in terms of a difference in the surface roughness parameters. As known, nanoparticles deposited in vacuum consist of a number of small crystallites, which contain a number of nano- and micro-scale air pockets. The impact of these air pockets can be cumulative once they interface with the droplet of liquid, efficiently supporting the weight of the droplet and effectively increasing the macroscopic contact angle. According to the Cassie-Baxter theory, the higher the section of the area of air that is under the droplet, the higher is the value of the contact angle[44]. Our results are in agreement with other studies that reported an increase in the contact angle when ZnO nanoparticles were incorporated into polymers [45-47].

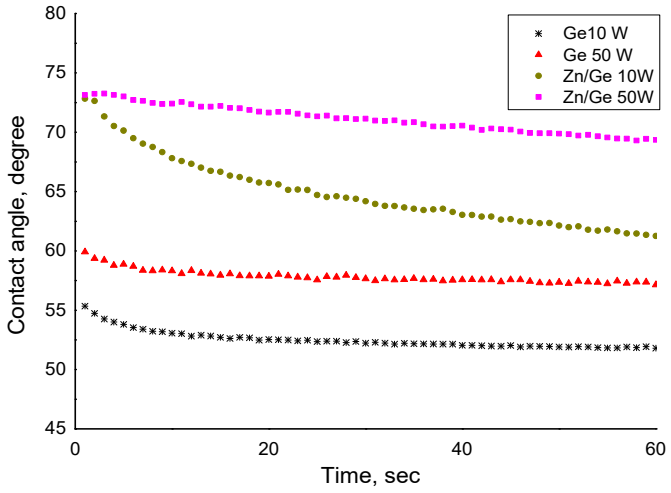

Figure IV.6. Water contact angle values for pristine and zinc/composite films fabricated at 10 W and 50 W. The data represent means of five replicates, with standard deviations are ± 4˚.

IV.4.3. In vitro antimicrobial performance

Figure IV.7 shows the bacterial viability of gram-positive *S. aureus* on surfaces of control, Ge 10 W, Ge 50 W, Zn/Ge 10 W and Zn/Ge 50 W. The Confocal scanning laser microscopy (CLSM) imaging evidently showed a much higher average number of cells adhered to the control surface compared to all polymers and composites samples. Figure IV.8 indicates that approximately, 80% of *S. aureus* were alive on the control, while the viability of cells were 53%, 50%, 31% and 42% on Ge 10 W, Ge 50 W, Zn/Ge 10 W and Zn/Ge 50 W, respectively. Similarly, figure IV.9 display the bacterial viability of gram-negative *E. coli* cells on the control, pristine and composite films. On the control, 81% of *E. coli* were viable on the surface, while the viability of cells were approximately 60%, 76%, 33% and 44% on Ge 10 W, Ge 50 W, Zn/Ge 10 W and Zn/Ge 50 W, respectively, as seen in figure IV.10.

The bio-activity of essential oils is often linked to their chemical structure, mainly to functionalities that govern solubility in water and lipophilicity, as these characteristics allow the oils to approach, disturb and pass through bacterial membrane[48]. These disruptions then initiate membrane expansion, increase of membrane permeability, disorder of membrane embedded proteins, inhibition of respiration, and impact ion transport processes in microbial cell. Carvacrol oil, for example, was found to make the cell membrane permeable to K+ and H+, dissipating the proton motive force and reducing ATP production[49]. Despite the fact the relation between chemical structure and bio-activity is not fully understood, it is generally accepted that oils with –OH group are more biologically effective than their similarly-structured OH-lacking counterparts[27, 50]. However, introducing essential molecules oil in to plasma environment

created oxygen species, light and heat leads to their isomerization, oxidation, polymerization, dehydrogenation and thermal re-arrangements[4]. This results in the formation of a wide variety of biologically-active derivative monomers, dimers and polymers, reactive oxygen species and a wide range of oxidation ions. The degree of molecules dissociation is highly reliant on the processing parameters of the applied plasma. Thus-created oil-fragments then undergo recombination in the gas phase and on the surface of the given substrate, resulting in a highly crosslinked polymer, with a structure that is irregular. Perhaps, plasma would weaken/deteriorate the antimicrobial activity of the original oil, as a lot of molecules cross-linked and as such unable to interact with cellular membranes[48].

The antibacterial performance of pristine polymers derived from essential oils is largely associated with the surface chemistry and nanoscale topography of the films[51]. The cellular and enzymatic activities of the adhered bacteria could be inhibited by the presence of bio-active functional groups (e.g. hydroxyl, carboxylic, methyl) disturbing the microbial growth and/or preventing a proper attachment of microbial cells[42].

Although pristine polymers showed weak or moderate antibacterial activity against both gram-positive and gram-negative microorganisms, composites revealed enhanced bactericidal performance. It is obvious that zinc nanoparticles were directly involved in the inhibition of the pathogens. As shown in fig IV.7 and fig IV.9, the antibacterial performance of Zn/Ge 10W were greater compared to Zn/Ge 50 W. This observation can be linked to the influence of RF power on the size of the formed nanoparticles, where lower power created smaller particles. It is known that, in many cases, smaller nanoparticles reveal much higher antibacterial action in compare to larger nanoparticles under the same conditions [52, 53].

However, the antimicrobial mechanisms of metallic nanoparticles are principally different from pristine polymers, providing further strategies for targeting various microorganisms, as well as to decrease the possible microbial resistance. For example, physicochemical changes often take place in cell membranes when nanoparticles anchor to the outer surface of the bacterial body causing large variation in the permeability of cell walls[54]. Nanoparticles are also capable to enter, in a distinct way, inside the cell due to the ultra-small size of these particles. The precipitation of NPs may gather in the cytoplasm, or in the periplasm space, disrupting the cellular activities causing membranes disturbance and disorder. Brayner *et al.* reported that the interaction between *E. coli* and ZnO-NPs led to a significant damage to the bacteria (e.g. disorganized cell walls) and penetration of NPs into the cell, followed by intracellular content leakage[55]. Furthermore, upon interaction with bacterial cells, ZnO may generate reactive oxygen species (ROS), such as hydrogen peroxide (H_2O_2), hydroxyl radicals ($OH^{\bullet}$), superoxide radicals (O^{-}_2), and singlet oxygen ($O^{\square}_2$). At high rate, these chemically-reactive species can be ruthlessly

damaging to a bacterial cell owing to deterioration of proteins, peptidoglycan, ribosomes, DNA, as well as inhibition of enzymatic activities and amino acid production, ultimately leading to cell lysis [56, 57]. So, we believe that Zn/Ge 10 W samples have shown higher performance as a result of a combination of different bactericidal mechanisms.

Many reports showed that gram-positive bacteria appear to be more resistant against ZnO NPs [58, 59]. This linked to the specific thick and negatively charged peptidoglycan layer in the bacterial cell wall that can resist ZnO penetration. In contrast, other findings have found that gram-negative bacteria are more resistant to NPs activities [60-62]. In addition, more experiments showed that ZnO had almost similar effect on both bacterial strains [63]. It can be understood that contradictory results in which bacteria are more resistant. Indeed, ZnO NPs are currently manufactured with different dimensions, morphologies, concentrations, modifications, surface defects, surface charges, crystallographic orientation etc. The antibacterial mechanisms vary based on the physicochemical properties of nanoparticles and their microenvironment conditions. For example, in different media, the dissolving profile of Zn may varies according to the medium components, and accordingly have potential influence upon the follow-on toxicity mechanism[64]. However, in our experimental conditions, attached bacterial cells on the Zn/Ge composites did not expose to only ZnO nanoparticles, but rather they were affected by both released-ZnO and geranium polymer surfaces at the same time. Geranium polymers contains chemical groups (e.g. hydroxyl and carboxyl), which proved in a previous study to reveal moderate antibacterial and anti-biofouling activities. The inhibitory effects of Zn/Ge composite films were observed to be very similar on *S. aureus* and *E. coli*. Furthermore, we expect that interactions between the geranium oil vapors (contain alcohols) and ZnO NPs occurred during composites fabrication. Here, more desired functional groups are presented on ZnO surface, which is modify. Surface modifications of the ZnO NPs in oxidizing environments had been demonstrated to cause an impotent change in the antibacterial activity[65], which can be utilized in biomaterials. For example, Galindo et al. modified the surface of ZnO NPs by chemical components including di-functional alcohol, where these metallic particles can be used in antimicrobial medical devices [66].

The antimicrobial performance of Zn/Ge composites is governed by a wide range of intrinsic factors. Given the close interconnection between fundamental polymer characteristics (e.g. surface chemistry, wettability, degree of cross-linking and topography) and NPs properties (e.g. shape, size, particle charge, concentration and crystallinity), it is possible that the synergistic outcomes of these factors inhibited bacterial viability. For example, Potara et al syntheses bio-nanocomposites from silver nanoparticles and chitosan, which act synergistically against[67]. Similarly, Prasad et al found that nanocomposites (made from graphene and silver nanoparticles) are significantly more effective against pathogens than either individual components[68].

Furthermore, other factors, such as temperature, UV/light, pH, species of the microorganism could influence the antibacterial performance of these composites [69, 70].

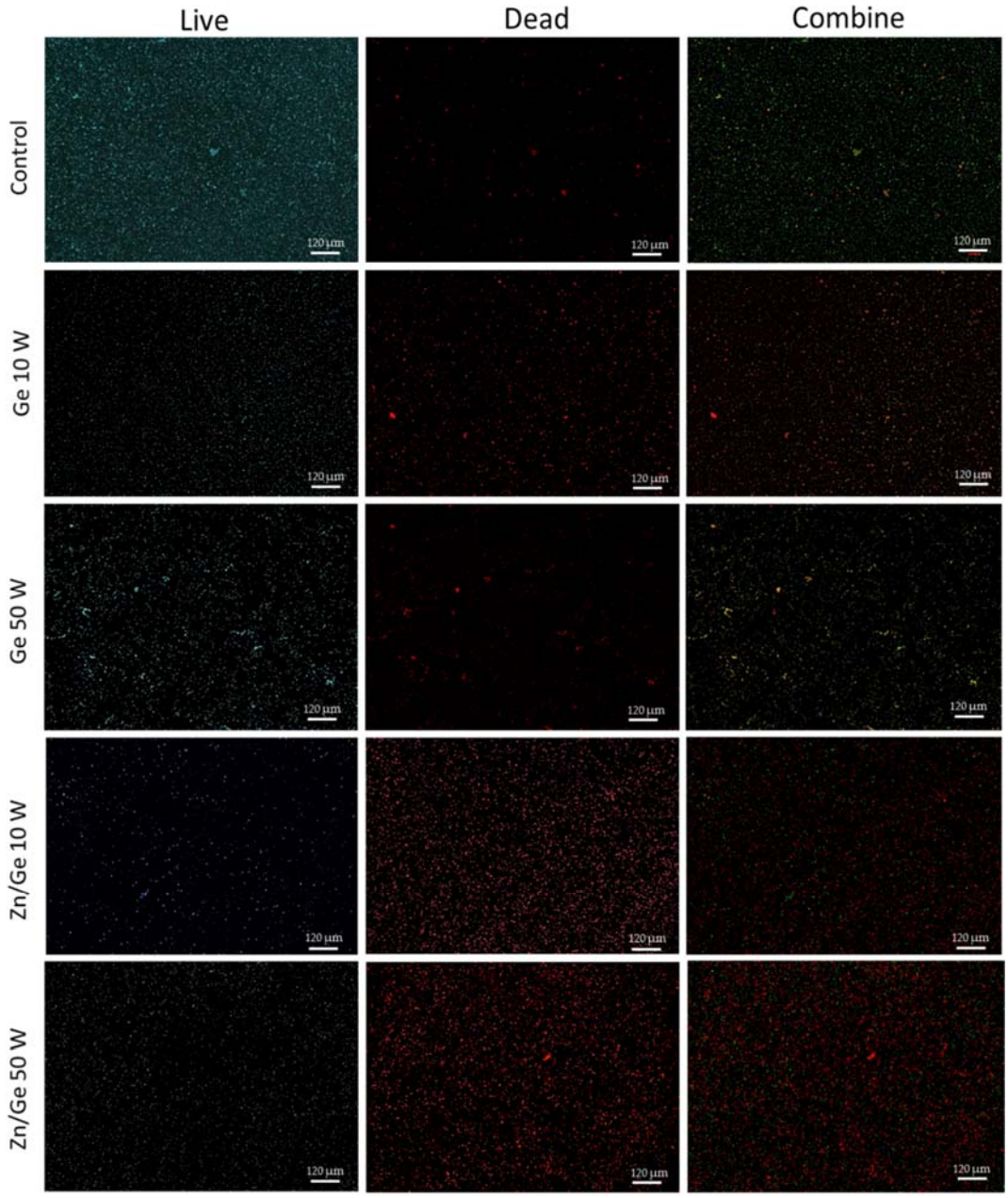

Figure IV.7. Confocal scanning laser microscopy images of *S. aureus* on control, Ge 10 W, Ge 50 W, Zn/Ge 10 W and Zn/Ge 50 W visualize viable cells stained green and dead cells stained red with Invitrogen Dead/Live Kit, with their combined images.

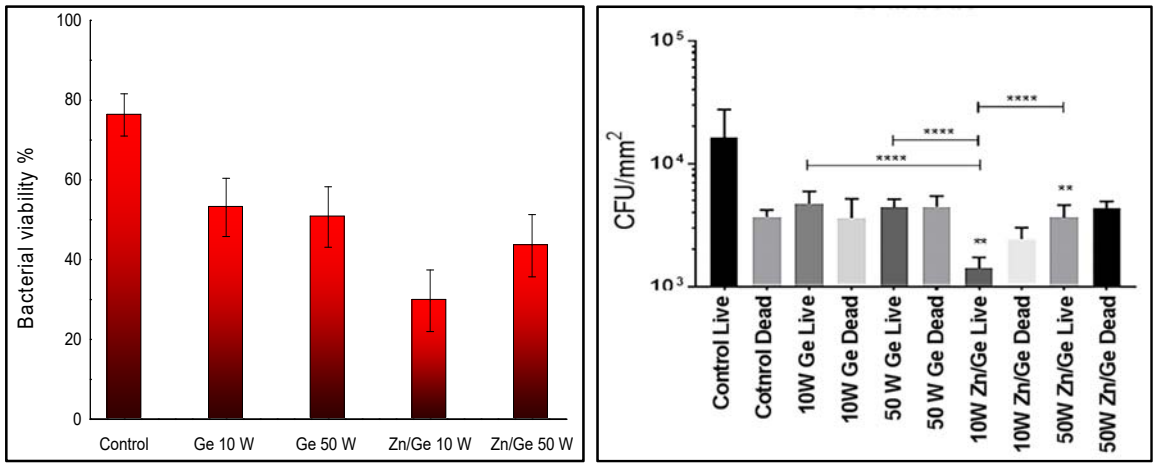

Figure IV.8. The bar chart (left) shows *S. aureus* viability on the samples. The statistical analysis chart (right) displays the antibacterial performance of all samples. Data shown represent means ± SD (n = 3). The statistical significance is given in terms of * ($P < 0.05$).

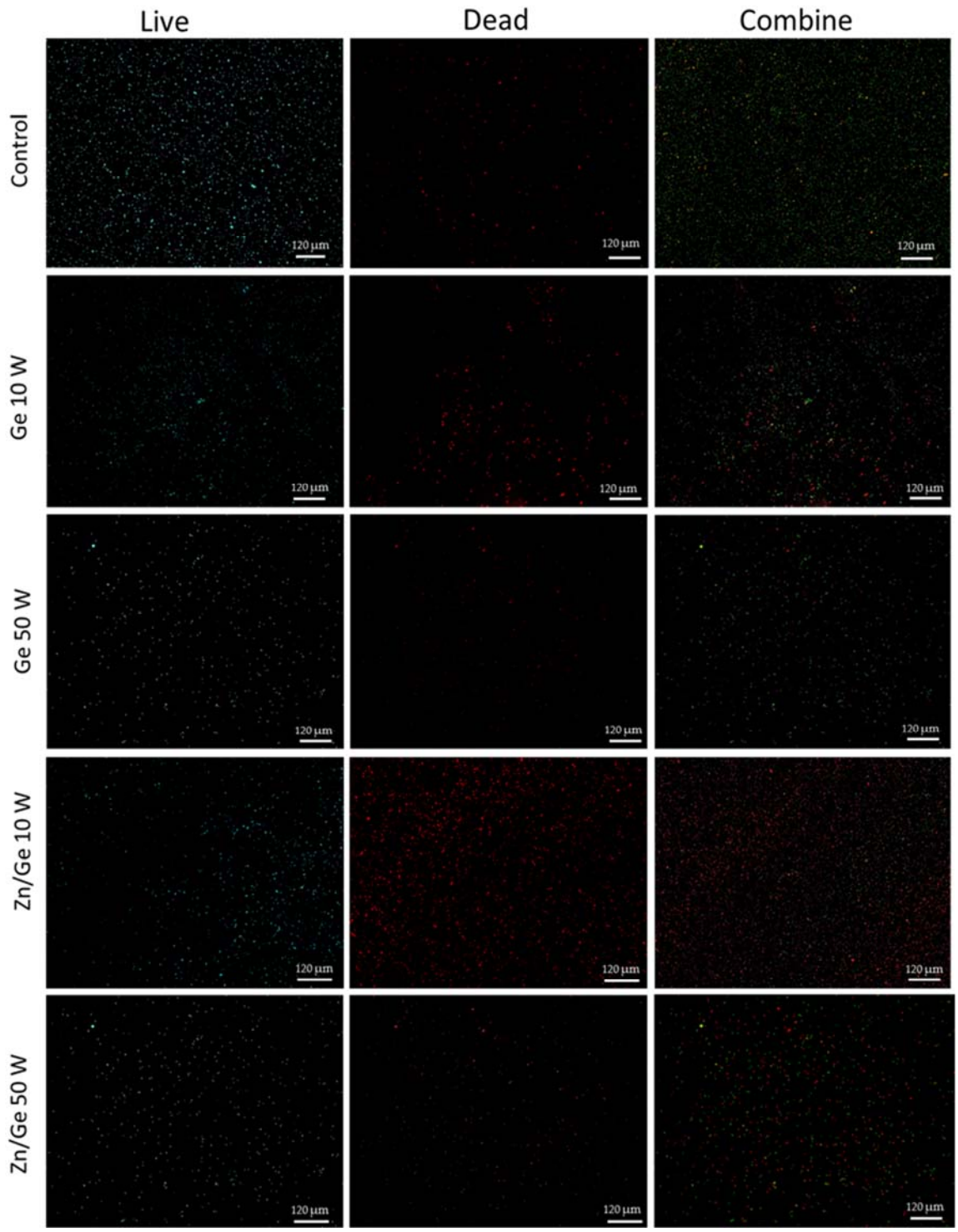

Figure IV.9. Confocal scanning laser microscopy images of *E.coli* on control, Ge 10 W, Ge 50 W, Zn/Ge 10 W and Zn/Ge 50 W visualize viable cells stained green and dead cells stained red with Invitrogen Dead/Live Kit.

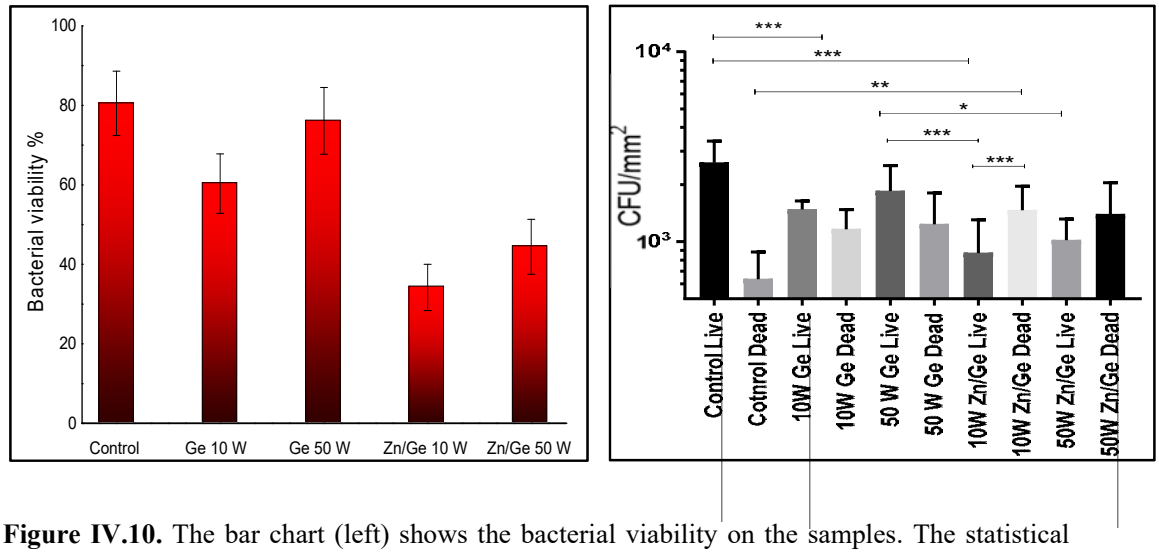

Figure IV.10. The bar chart (left) shows the bacterial viability on the samples. The statistical analysis chart (right) displays the antibacterial performance of all samples. Data shown represent means ± SD (n = 3). The statistical significance is given in terms of * ($P < 0.05$).

IV.4.4. Zinc release profile

The release of zinc from Zn/Ge 10 W was confirmed using ICP measurements showing a relatively quick and sharp release profile of ZnO NPs within less than 24 h, as seen in fig IV.11. A high rate of nanoparticle release could be preferred in various medical applications. For example, a rapid release offers powerful antibacterial activity during the early post-operation period that inhibit the possible development of microbial resistance[71]. Nevertheless, for other applications, such as implanted synthetic devices, surfaces should preserve their antibacterial performance until integration with the surrounding tissues, with sustained prevention of microbial colonization and subsequent biofilms formation[72]. Thus, it is vital to adjust the releasing rate to match a specific application. In this regard, a recent approach to control the release of zinc oxide nanoparticles from coatings is to use a bi-layer polymeric system. Zn/Ge 10 W and Zn/Ge 50 W composites were coated by an extra thin layer (25 ± 5 and 50 ± 5 nm) of geranium film to reduce the releasing rate of zinc, which consequently increases the performance time. The measurements showed that the rate of release decreased, extending the time up to 40 and 60 h for Zn/Ge 10 W and Zn/Ge 50 W composites, respectively. The slowest release rate was observed for composites coated with a 50 nm-think top layer.

It had been shown in previous report that metallic nanoparticles (size of 15 nm and 70 nm) can pass through a thin upper layer of plasma polymer (thickness of 30 nm) upon immersion in aqueous solvents[73]. A one more study demonstrated that increasing in the thickness of the upper

polymeric layer achieves a reduction of the rate of release of metal ions compared to composites without such an upper plasma film [74]. Same study proved that the upper layer coatings (thicknesses of 6, 12, and 18 nm) did not affect the antibacterial activities of the nanoparticles [74]. In our Zn/Ge composites, we observed similar trend as a thicker geranium upper layer would provide more robust polymers that further reduce the releasing rate of nanoparticles, without major variations in the biological performance for samples fabricated at 10 W. This indicates that the rate of release can be adjusted via the thickness of the thin barrier plasma polymer. The upper layer polymeric layer may function as both a 3-D matrix for protection the nanoparticles from the medium, and to delay the release of zinc, giving the potential to yield a variety of release profiles. Obviously, the thickness of the upper layer should be selected carefully to ensure the maximum release of the nanoparticles, where bulk of nanoparticles could be trapped inside the upper layer, which will be comprehensively investigated in an upcoming study.

ICP results in figure IV.11 shows that composites fabricated at higher input power (50 W) possess a considerable lower releasing rate compare to composites fabricated at 10 W. This can be linked to the cross-linking degree of the material. It is well known that fabricating geranium plasma polymers at higher power leads to increase in cross-linking degree, and potentially rise resistance against deformation[41]. The resultant polymers become harder and more rigid owing to the increase in the bonding interconnection and chains dense packing[75]. Here, we assume that the increase in the bonding interconnection degree would curb/restrain the freeing of nanoparticles from the films fabricated at 50 W. ICP data suggested that a higher concentration of ZnO was released from surfaces of ZnO/Ge 10 W, making it significantly more antibacterial effective than ZnO/Ge 50 W that showed low releasing degree; and hence much less antibacterial activities.

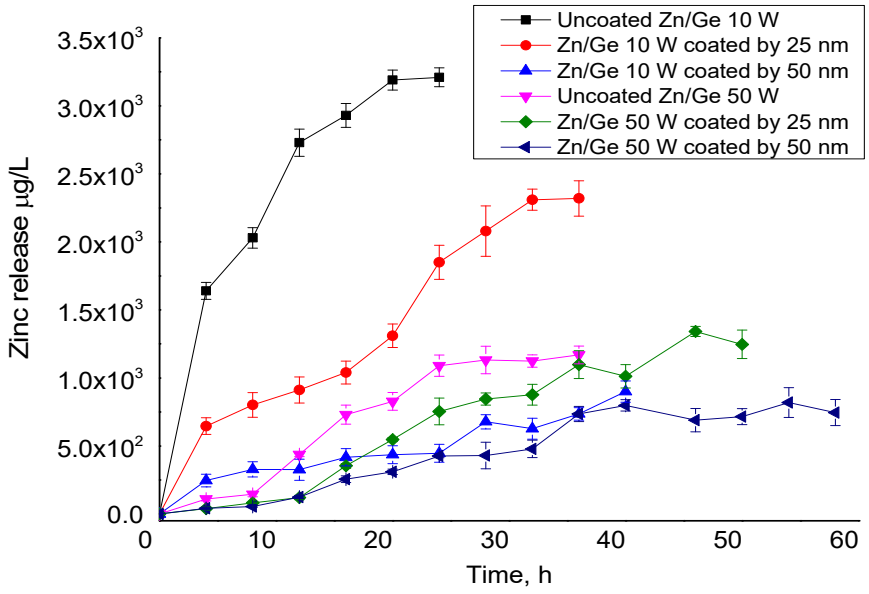

Figure IV.11. The release profile of zinc nanoparticles from Zn/Ge 10 W and Zn/Ge 50 W nanocomposite and its bi-layer system. The data were acquired in 5 ml of double distillated water in dark conditions using inductive coupled plasma measurements.

IV.5. Conclusion

We successfully developed a nanocomposite material from geranium essential oil and the thermal decomposition of zinc acetylacetonate in one step plasma system. XPS survey confirmed the presence of ZnO in the fabricated polymers at 10 W and 50 W. SEM images showed that the average size of ZnO nanoparticle increased with an increase in the power of deposition from approximately 60 nm at 10 W to approximately 80 nm at 50 W. AFM data showed a significant increase in surface roughness of the composites compared to pristine samples. The antibacterial activity of ZnO-NPs incorporated into geranium films toward both gram-positive (*S. aureus*) and gram-negative (*E. coli*) bacteria were demonstrated. The release of nanoparticles was confirmed using ICP measurements, and can be further controlled through a bi-layer system. These coatings were confirmed to be a promising candidate for protecting material surface from bacterial attachment and colonization for relevant medical devices and implants.

References

1. Hanisch, C., et al., *Fast electrical response to volatile organic compounds of 2D Au nanoparticle layers embedded into polymers.* Journal of Materials Science, 2011. **46**(2): p. 438-445.

2. Zhang, R.-C., et al., *Gold nanoparticle-polymer nanocomposites synthesized by room temperature atmospheric pressure plasma and their potential for fuel cell electrocatalytic application.* Scientific Reports, 2017. **7**: p. 46682.

3. Heilmann, A., *Polymer films with embedded metal nanoparticles.* Vol. 52. 2013: Springer Science & Business Media.

4. Al-Jumaili, A., et al., *Plant Secondary Metabolite-Derived Polymers: A Potential Approach to Develop Antimicrobial Films.* Polymers, 2018. **10**(5): p. 515.

5. Drábik, M., et al., *Long-term aging of Ag/aC: H: O nanocomposite coatings in air and in aqueous environment.* Science and technology of advanced materials, 2015. **16**(2): p. 025005.

6. Di Mauro, A., et al., *Novel synthesis of ZnO/PMMA nanocomposites for photocatalytic applications.* Scientific Reports, 2017. **7**: p. 40895.

7. Palza, H., *Antimicrobial polymers with metal nanoparticles.* International journal of molecular sciences, 2015. **16**(1): p. 2099-2116.

8. Al-Jumaili, A., et al., *Plasma Treatment of Polymeric Membranes*, in *Non-Thermal Plasma Technology for Polymeric Materials*. 2019, Elsevier. p. 211-240.

9. Bazaka, K., et al., *Plasma-assisted surface modification of organic biopolymers to prevent bacterial attachment.* Acta biomaterialia, 2011. **7**(5): p. 2015-2028.

10. Jacob, M. and K. Bazaka, *Fabrication of Electronic Materials from Australian Essential Oils*. 2010: Australian Government: Rural Industries Research and Development Corporation.

11. Chan, Y.W., et al., *Plasma polymerized carvone as an antibacterial and biocompatible coating.* Materials Science and Engineering: C, 2016. **68**: p. 861-871.

12. Hlídek, P., et al., *Behavior of polymeric matrices containing silver inclusions, 2–Oxidative aging of nanocomposite Ag/C: H and Ag/C: H: O films.* Plasma Processes and Polymers, 2009. **6**(1): p. 34-44.

13. Körner, E., et al., *Formation and distribution of silver nanoparticles in a functional plasma polymer matrix and related Ag+ release properties.* Plasma Processes and Polymers, 2010. **7**(7): p. 619-625.

14. Wang, Z.L., *Zinc oxide nanostructures: growth, properties and applications.* Journal of Physics: Condensed Matter, 2004. **16**(25): p. R829-R858.

15. Liu, Y., et al., *Antibacterial activities of zinc oxide nanoparticles against Escherichia coli O157: H7.* Journal of Applied Microbiology, 2009. **107**(4): p. 1193-1201.

16. Tayel, A.A., et al., *Antibacterial Action of Zinc Oxide Nanoparticles against Foodborne Pathogens.* Journal of Food Safety, 2011. **31**(2): p. 211-218.

17. Petrović, Ž., et al., *Nano/microstructure and optical properties of ZnO particles precipitated from zinc acetylacetonate.* Journal of Molecular Structure, 2015. **1090**: p. 121-128.

18. Fauteux, C., et al., *Fast synthesis of ZnO nanostructures by laser-induced decomposition of zinc acetylacetonate.* Inorganic chemistry, 2007. **46**(26): p. 11036-11047.

19. Ambrožič, G., et al., *The synthesis of zinc oxide nanoparticles from zinc acetylacetonate hydrate and 1-butanol or isobutanol.* Journal of colloid and interface science, 2010. **346**(2): p. 317-323.

20. Liu, J., et al., *Synthesis of relatively monodisperse ZnO nanocrystals from a precursor zinc 2, 4-pentanedionate.* Materials Letters, 2007. **61**(13): p. 2837-2840.

21. Ao, W., et al., *Mechanochemical synthesis of zinc oxide nanocrystalline.* Powder Technology, 2006. **168**(3): p. 148-151.

22. Yao, B., Y. Chan, and N. Wang, *Formation of ZnO nanostructures by a simple way of thermal evaporation.* Applied Physics Letters, 2002. **81**(4): p. 757-759.

23. Rodríguez-Paéz, J.E., et al., *Controlled precipitation methods: formation mechanism of ZnO nanoparticles.* Journal of the European Ceramic Society, 2001. **21**(7): p. 925-930.

24. Jacob, M.V., et al., *Plasma polymerised thin films for flexible electronic applications.* Thin Solid Films, 2013. **546**: p. 167-170.

25. Scientific, T.F. *LIVE/DEAD® BacLight Bacterial Viability Kits*. 2004; Available from: https://assets.thermofisher.com/TFS-Assets/LSG/manuals/mp07007.pdf.

26. Lotz, A., et al., *Antimicrobial efficacy and optimized cell adhesion from defined plasma polymerised multilayer structures involving zinc acetylacetonate and allylamine.* Journal of Materials Chemistry, 2012. **22**(37): p. 19455.

27. Bazaka, K., et al., *Anti-bacterial surfaces: natural agents, mechanisms of action, and plasma surface modification.* RSC Advances, 2015. **5**(60): p. 48739-48759.

28. Kołodziejczak-Radzimska, A. and T. Jesionowski, *Zinc Oxide—From Synthesis to Application: A Review.* Materials, 2014. **7**(4): p. 2833.

29. Malzahn, K., et al., *Antimicrobial Activity and Cyto-Compatibility of Plasma Polymerized Zinc Acetylacetonate Thin Films.* Plasma Processes and Polymers, 2013. **10**(3): p. 243-249.

30. Tjong, S.C., *Structural and mechanical properties of polymer nanocomposites.* Materials Science and Engineering: R: Reports, 2006. **53**(3): p. 73-197.

31. Wang, Z.L., *Nanostructures of zinc oxide.* Materials Today, 2004. **7**(6): p. 26-33.

32. Dai, Z.R., Z.W. Pan, and Z.L. Wang, *Novel nanostructures of functional oxides synthesized by thermal evaporation.* Advanced Functional Materials, 2003. **13**(1): p. 9-24.

33. Lischer, S., et al., *Antibacterial burst-release from minimal Ag-containing plasma polymer coatings.* Journal of the Royal Society Interface, 2011. **8**(60): p. 1019-1030.

34. Balazs, D.J., et al., *Multi-Functional Nanocomposite Plasma Coatings—Enabling New Applications in Biomaterials.* Plasma Processes and Polymers, 2007. **4**(S1): p. S380-S385.

35. Vanithakumari, S.C. and K.K. Nanda, *A universal relation for the cohesive energy of nanoparticles.* Physics Letters A, 2008. **372**(46): p. 6930-6934.

36. Soofivand, F., M. Salavati-Niasari, and F. Mohandes, *Novel precursor-assisted synthesis and characterization of zinc oxide nanoparticles/nanofibers.* Materials Letters, 2013. **98**: p. 55-58.

37. Schneider, J.r.J., et al., *Synthesis, characterization, defect chemistry, and FET properties of microwave-derived nanoscaled zinc oxide.* Chemistry of Materials, 2010. **22**(7): p. 2203-2212.

38. Duque, L. and R. Förch, *Plasma Polymerization of Zinc Acetyl Acetonate for the Development of a Polymer-based Zinc Release System.* Plasma Processes and Polymers, 2011. **8**(5): p. 444-451.

39. Music, S., A. Šarić, and S. Popović, *Formation of nanosize ZnO particles by thermal decomposition of zinc acetylacetonate monohydrate.* Ceramics International, 2010. **36**(3): p. 1117-1123.

40. Arii, T. and A. Kishi, *Humidity controlled thermal analysis: the effect of humidity on thermal decomposition of zinc acetylacetonate monohydrate.* Journal of thermal analysis and calorimetry, 2006. **83**(1): p. 253-260.

41. Al-Jumaili, A., K. Bazaka, and M.V. Jacob, *Retention of Antibacterial Activity in Geranium Plasma Polymer Thin Films.* Nanomaterials, 2017. **7**(9): p. 270.

42. Bazaka, K., et al., *The effect of polyterpenol thin film surfaces on bacterial viability and adhesion.* Polymers, 2011. **3**(1): p. 388-404.

43. Chinnam, J., et al., *Measurements of the contact angle of nanofluids and development of a new correlation.* International Communications in Heat and Mass Transfer, 2015. **62**: p. 1-12.

44. Blossey, R., *Self-cleaning surfaces—virtual realities.* Nature materials, 2003. **2**(5): p. 301.

45. Jin, X., et al., *Study of tetrapodal ZnO-PDMS composites: A comparison of fillers shapes in stiffness and hydrophobicity improvements.* PLoS One, 2014. **9**(9): p. e106991.

46. González, N., et al., *Influence of ZnO and TiO2 Particle Sizes in the Mechanical and Dielectric Properties of Vulcanized Rubber.* Materials Research, 2017(AHEAD): p. 0-0.

47. Augustine, R., N. Kalarikkal, and S. Thomas, *Effect of zinc oxide nanoparticles on the in vitro degradation of electrospun polycaprolactone membranes in simulated body fluid.*

International Journal of Polymeric Materials and Polymeric Biomaterials, 2016. **65**(1): p. 28-37.

48. Bazaka, K., et al., *Plasma-potentiated small molecules—possible alternative to antibiotics?* Nano Futures, 2017. **1**(2): p. 025002.

49. Ultee, A., E. Kets, and E. Smid, *Mechanisms of action of carvacrol on the food-borne pathogen Bacillus cereus.* Applied and environmental microbiology, 1999. **65**(10): p. 4606-4610.

50. Daglia, M., *Polyphenols as antimicrobial agents.* Current Opinion in Biotechnology, 2012. **23**(2): p. 174-181.

51. Bazaka, K., et al., *Efficient surface modification of biomaterial to prevent biofilm formation and the attachment of microorganisms.* Applied microbiology and biotechnology, 2012. **95**(2): p. 299-311.

52. Raghupathi, K.R., R.T. Koodali, and A.C. Manna, *Size-dependent bacterial growth inhibition and mechanism of antibacterial activity of zinc oxide nanoparticles.* Langmuir, 2011. **27**(7): p. 4020-8.

53. Padmavathy, N. and R. Vijayaraghavan, *Enhanced bioactivity of ZnO nanoparticles—an antimicrobial study.* Science and Technology of Advanced Materials, 2016.

54. Al-Jumaili, A., et al., *Review on the Antimicrobial Properties of Carbon Nanostructures.* Materials, 2017. **10**(9): p. 1066.

55. Brayner, R., et al., *Toxicological impact studies based on Escherichia coli bacteria in ultrafine ZnO nanoparticles colloidal medium.* Nano Letters, 2006. **6**(4): p. 866-870.

56. Pelgrift, R.Y. and A.J. Friedman, *Nanotechnology as a therapeutic tool to combat microbial resistance.* Advanced Drug Delivery Reviews, 2013. **65**(13–14): p. 1803-1815.

57. Naddeo, J., et al., *Antibacterial Properties of Nanoparticles: A Comparative Review of Chemically Synthesized and Laser-Generated Particles.* Advanced Science, Engineering and Medicine, 2015. **7**(12): p. 1044-1057.

58. Sinha, R., et al., *Interaction and nanotoxic effect of ZnO and Ag nanoparticles on mesophilic and halophilic bacterial cells.* Bioresource Technology, 2011. **102**(2): p. 1516-1520.

59. Arakha, M., et al., *The effects of interfacial potential on antimicrobial propensity of ZnO nanoparticle.* Scientific reports, 2015. **5**: p. 9578.

60. Premanathan, M., et al., *Selective toxicity of ZnO nanoparticles toward Gram-positive bacteria and cancer cells by apoptosis through lipid peroxidation.* Nanomedicine: Nanotechnology, Biology and Medicine, 2011. **7**(2): p. 184-192.

61. Azam, A., et al., *Antimicrobial activity of metal oxide nanoparticles against Gram-positive and Gram-negative bacteria: a comparative study.* International journal of nanomedicine, 2012. **7**: p. 6003.

62. Emami-Karvani, Z. and P. Chehrazi, *Antibacterial activity of ZnO nanoparticle on gram-positive and gram-negative bacteria.* Afr J Microbiol Res, 2011. **5**(12): p. 1368-1373.

63. Jiang, W., H. Mashayekhi, and B. Xing, *Bacterial toxicity comparison between nano-and micro-scaled oxide particles.* Environmental Pollution, 2009. **157**(5): p. 1619-1625.

64. Dimapilis, E.A.S., et al., *Zinc oxide nanoparticles for water disinfection.* Sustainable Environment Research, 2018. **28**(2): p. 47-56.

65. Mehmood, S., et al., *Significance of postgrowth processing of ZnO nanostructures on antibacterial activity against gram-positive and gram-negative bacteria.* International journal of nanomedicine, 2015. **10**: p. 4521.

66. Betancourt-Galindo, R., et al., *Surface Modification of ZnO Nanoparticles.* Materials Science Forum, 2010. **644**: p. 61-64.

67. Potara, M., et al., *Synergistic antibacterial activity of chitosan–silver nanocomposites on Staphylococcus aureus.* Nanotechnology, 2011. **22**(13): p. 135101.

68. Prasad, K., et al., *Synergic bactericidal effects of reduced graphene oxide and silver nanoparticles against Gram-positive and Gram-negative bacteria.* Scientific Reports, 2017. **7**.

69. Sirelkhatim, A., et al., *Review on Zinc Oxide Nanoparticles: Antibacterial Activity and Toxicity Mechanism.* Nano-Micro Letters, 2015. **7**(3): p. 219-242.

70. Li, M., et al., *Synergistic Bactericidal Activity of Ag-TiO2 Nanoparticles in Both Light and Dark Conditions.* Environmental Science & Technology, 2011. **45**(20): p. 8989-8995.

71. Hetrick, E.M. and M.H. Schoenfisch, *Reducing implant-related infections: active release strategies.* Chemical Society Reviews, 2006. **35**(9): p. 780-789.

72. Cloutier, M., D. Mantovani, and F. Rosei, *Antibacterial coatings: challenges, perspectives, and opportunities.* Trends in biotechnology, 2015. **33**(11): p. 637-652.

73. Vasilev, K., et al., *Template-Assisted Generation of Nanocavities within Plasma Polymer Films.* The Journal of Physical Chemistry B, 2009. **113**(20): p. 7059-7063.

74. Vasilev, K., et al., *Tunable antibacterial coatings that support mammalian cell growth.* Nano letters, 2009. **10**(1): p. 202-207.

75. Al-Jumaili, A., et al., *The Electrical Properties of Plasma-Deposited Thin Films Derived from Pelargonium graveolens.* Electronics, 2017. **6**(4): p. 86.

Chapter V

Part 1

The Electrical Properties of Geranium Plasma polymer Thin Films

The primary focus of Chapter V is to study the electrical properties of geranium plasma polymer thin films (part 1) and Zinc incorporated geranium plasma polymer thin films (part 2). Chapter V-part 1 reports the outcomes of electrical characterization of geranium films as a potential insulating layer in organic electronic devices. The influence of power deposition on the dielectric constant and electrical conductivity of pristine geranium polymers was studied. In addition, the mechanisms of charge transport of the polymers were explored.

Chapter V-part 1 was published as:

Al-Jumaili, A.; Alancherry, S.; Bazaka, K.; Jacob, M.V. The Electrical Properties of Plasma-Deposited Thin Films Derived from Pelargonium graveolens. Electronics 2017, 6, 86.

Abstract

Inherently volatile at atmospheric pressure and room temperature, plant-derived precursors present an interesting human-health-friendly precursor for the chemical vapour deposition of thin films. The electrical properties of films derived from Pelargonium graveolens (geranium) were investigated in metal–insulator–metal (MIM) structures. Thin polymer-like films were deposited using plasma-enhanced synthesis under various plasma input power. The *J–V* characteristics of thus-fabricated MIM were then studied in order to determine the direct current (DC) conduction mechanism of the plasma polymer layers. It was found that the capacitance of the plasma-deposited films decreases at low frequencies ($C \approx 10^{-11}$) and remains at a relatively constant value ($C \approx 10^{-10}$) at high frequencies. These films also have a low dielectric constant across a wide range of frequencies that decreases as the input RF power increases. The conductivity was determined to be around 10^{-16}–10^{-17} Ω^{-1} m^{-1}, which is typical for insulating materials. The Richardson–Schottky mechanism might dominate charge transport in the higher field region for geranium thin films.

V.1.1. Introduction

Polymer thin films gained broad research interest in paving the way for low-cost engineering of large-area flexible electronic devices. Among different polymers investigated for organic

electronics, conducting polymers are used as electrodes and contacts for charge transporting [1], semiconducting polymers are employed as active layers in organic thin film transistors (OTFTs) [2] and organic photovoltaics (OPVs) [3], and insulating polymers are used as dielectric layers in OTFTs [4]. Over the years, much attention has been paid to the development of insulating polymers to replace the conventional gate dielectric materials, mostly silicon dioxide ($k \sim 4$), to realise flexible thin film transistors (TFTs) with a low operating voltage and high mobility [5,6]. To this end, a number of low dielectric constant polymers, such as polystyrene ($k \sim 2.6$) and polymethyl methacrylate ($k \sim 3.5$), and high dielectric constant polymers, such as poly (vinyl phenol) ($k \sim 4.2$) and poly (vinyl alcohol) ($k \sim 7.8$), have been synthetized and tested [5]. The majority of these polymers exhibit a low dielectric constant; a thicker layer (>300 nm) is hence required to suppress the leakage current. On the other hand, low dielectric thickness is an essential requirement for the gate dielectric to increase the capacitance per unit area and to achieve low operating voltage [7,8]. Unfortunately, reducing the thickness of polymer thin films below 50 nm is extremely challenging because of the formation of pinholes, non-uniformity, and the degradation of the dielectric strength that necessitates higher dielectric constant polymers [5,8–10]. Additionally, the present methods for the integration of polymer thin films into devices are mostly solution-assisted and thus present additional challenges, such as the incomplete removal of solvent residues, the degradation of existing layers while in contact with solvents, and a difficulty in achieving local patterning [11]. Therefore, development of polymeric materials with moderate k and stable dielectric performances within a lower thickness range via low-cost techniques compatible with modern microelectronics processing has become important.

Plasma polymerisation is one of the swiftly advancing techniques for fabricating highly uniform, ultra-thin pinhole-free polymer thin films from virtually any monomer on a wide variety of substrates. Where previously it was mostly used to fabricate highly crosslinked polymer-like materials that lacked a regularly repeating structure of conventional polymers [12], recent advances, such as the development of pulsed plasma deposition, have enabled the use of the plasma environment as an initiator and catalyst of chemical polymerisation reactions, producing polymers with a lower degree of cross-linking and a well-defined chemical structure [13,14]. In general, plasma polymers that are used as insulating layers are highly cross-linked, are well-adhered to the substrate, and can be made very thin, with a thickness of few tens of nanometres and with excellent conformity [15]. One of the properties that plasma polymers are recognised for is their high dielectric constant, which enables their application as flexible insulating layers in thin film device structures [16,17]. TFTs that are incorporated with dielectric layers formed by plasma polymerising styrene and vinyl acetate [18], acetylene [19], hexamethyldisiloxane [20], methyl methacrylate (pp-MMA) [21], dichlorotetra-methyldisiloxane (pp-DCTMDS) [17], and allyl amine/vinyl acetic acid [22] have shown good device characteristics. Plasma polymers are

also noticed for their excellent surface characteristics, so they are frequently uses as buffer layers to improve the interfacial characteristics in TFTs and organic light-emitting diode (OLED) devices [23,24].

Foreseeing the significant demand, along with the development of novel polymeric materials, much attention has also been paid to sustainable production of these materials from natural precursors. The green synthesis of polymers can markedly reduce the growing environmental concerns raised by the e-wastes (plastics, silicon etc.) and minimizes the dependence of organic electronic industry to petrochemical resources [25]. Furthermore, bio-degradability and biocompatibility of these classes of polymers open up new possibilities, such as the integration of electronics into living tissues [26,27]. Cellulose, hemicellulose, lignin, natural silk, gelatin, shellac, egg albumin, etc. are typical examples of naturally derived compounds that have been proven to be promising for bio-electronics applications [25,26]. Yet the major challenge is to identify a cheap and abundant material and an appropriate method to transform them into polymers, ensuring a low cost, complementary properties, and a better life-cycle assessment [28]. In this regard, plasma-assisted deposition gained considerable interest as plasma provides a highly reactive environment that enables the simple and efficient conversion of bio-renewable resources into diverse structures from simple polymers to advanced carbon nanostructures [29–32]. Our previous studies showed that essential oils (mixtures of volatile organic molecules extracted from different parts of plants) are promising precursor candidate for plasma polymerisation [29,33,34]. Plasma polymers derived from essential oils such as terpenol, linalyl acetate, and γ-terpinene have been demonstrated to be suitable for different applications such as insulating layers, encapsulation layers in organic electronics, and biocompatible coatings for implants [23,35–37].

Hence, plasma polymers fabricated from individual components of essential oils have the potential to meet the various material demands put forward by the organic electronics industry. Material costs, processing complexity, and environmental impact can be further reduced by fabricating polymers directly from multicomponent essential oil instead of pure, individual components (e.g., terpinene-4-ol). However, the properties of essential-oil-derived plasma polymers are correlated with the chemical composition of the precursor oil [38]. For instance, plasma polymer synthesised from terpenol has exhibited electron-blocking hole-transporting behaviour, whereas plasma-polymerised linalyl acetate has not [39]. It is therefore important to further investigate the extent to which the multi-component nature of the oil, in this study the Pelargonium graveolens (geranium essential oil), affects the electrical properties, such as the dielectric constant and conductivity, of the polymer thin films synthesized under varied input RF power.

V.1.2. Experimental

Microscope glass slides (76 mm × 26 mm) were sonicated in a solution of distilled water and commercial decon for 20 min before being rinsed in acetone and dried using compressed air. Aluminium electrodes were deposited onto the glass slides using thermal evaporation system model HIND 12A4D (HINDHIVAC, Bangalore, KA, India) under a pressure of (7×10^{-5} torr). Organic thin layers were fabricated on the aluminium utilizing custom-built plasma-enhanced chemical vapor deposition (PECVD) system (MKS Instruments, Andover, MA, USA). A generator provided radio frequency (RF) power at 13.56 MHz to a glass tube via capacitively coupled copper electrodes. The pelargonium essential oil was obtained from Australian Botanical Products, and was used without further modification. The main compounds include citronellol (32%), geraniol (15%), linalool (6%), isomenthone (6%), geranyl formate (2.5%), tiglate (2%), citronellyl formate (6%), guaia-6,9-diene, and 10-epi-*γ* eudesmol (5%). The chemical structure of some components of pelargonium is presented in Figure V.1.1.

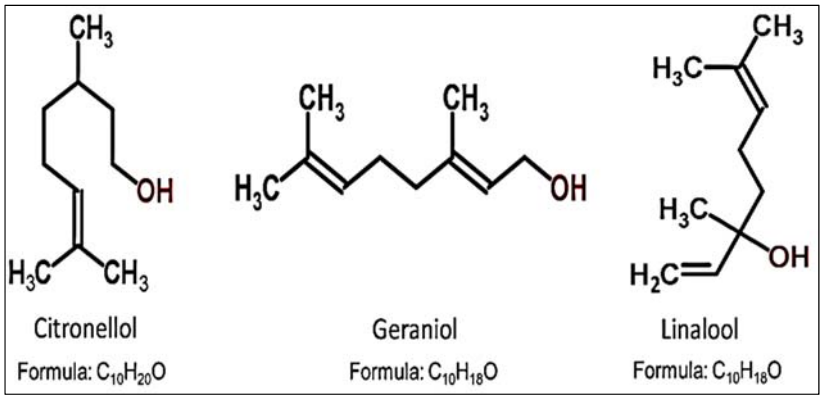

Figure V.1.1. The chemical structure of main components of pelargonium essential oil.

In each experiment, 0.5 g of the monomer was used, producing an average flow rate of ~16 cm^3/min and a film thickness in a range ~500–700 nm. Power levels of 10 W, 25 W, 50 W, 75 W, and 100 W were applied to fabricate the organic films. Finally, aluminium electrodes were fabricated on top of the organic layers using a custom made shadow mask, which created a device with metal–insulator–metal (MIM) structures as seen in Figure **V.1.**2.

Then, dielectric properties were investigated between frequencies of 10 Hz and 100 KHz utilizing a Hioki 3522 LCR meter (Hioki, Ueda, NA, Japan). From the known thickness and the area of the device, and measured C values, dielectric constant was determined. Additionally, *I–V* measurements were performed on the MIM structures using a Keithley 2636A source meter (Keithley, Cleveland, OH, United States.Data were acquired between 0 and 20 V, with steps of 0.2 V for each point at room temperature.

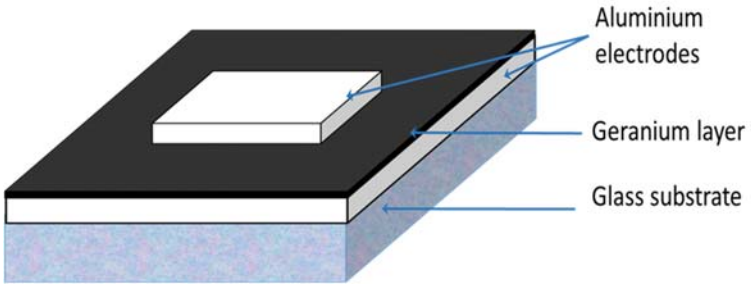

Figure V.1.2. Metal–insulator–metal (MIM) structure used to study the electrical properties of geranium plasma polymer thin films.

V.1.3. Results and Discussion

As seen in the atomic force microscopy (AFM) images in Figure 3A, the pelargonium graveolens plasma polymer films seemed to be smooth, defect-free, and homogeneous on the nano-scale, indicating that polymerisation reactions took place basically on the surface of the substrate instead of in the gas phase. The films were also shown to be optically transparent within the visible wavelength range, based on the absorbance and transmission data in Figure 3B,C, similar to films from γ-terpinene [40] and terpinene-4-ol [38]. Furthermore, the energy gap (E_g) of the pelargonium films was calculated by applying the Tauc relation to the optical absorption coefficient data recorded from UV-Vis spectroscopy measurements. Polymers fabricated at 10 and 100 W had $E_g \approx 3.67$ and 3.60 eV, respectively. The reduction in E_g as a result of power deposition was attributed to dangling bonds that formed in the polymer structure during the fabrication process. At low input power density, a low concentration of dangling bonds are created due to their saturation with hydrogen atoms, whereas higher input power enhances the fragmentation rate in the plasma field [41], which highly accelerates the formation of chains with unsaturated bonds [42]. The relatively high energy gap for geranium plasma polymer films is in good agreement with the low conductivity values acquired in this study. Further details regarding the effect of deposition power on morphological, optical, mechanical, and chemical properties of pelargonium plasma polymer films can be found in [43].

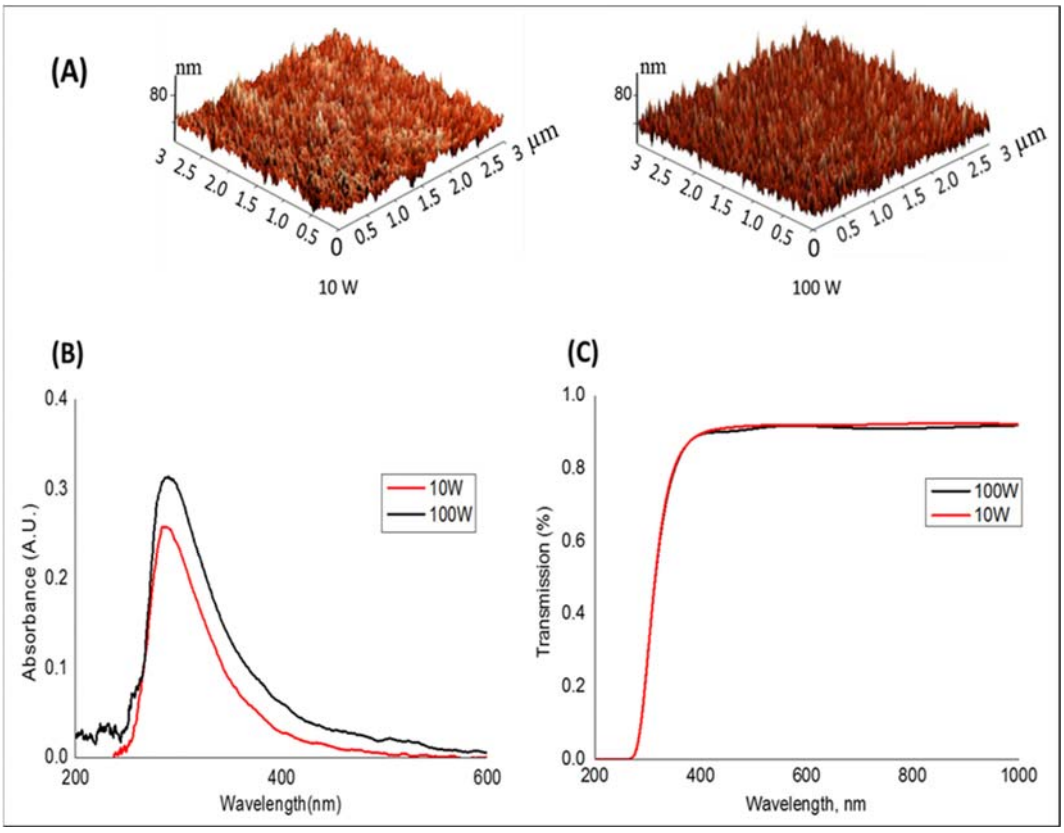

Figure V.1.3. (**A**) Atomic force microscope images of pelargonium plasma polymer films fabricated at 10 W and 100 W. (**B**) Ultraviolet–visible spectroscopy (UV-VIS) measurements of pelargonium plasma polymer films deposited at various input power. (**C**) Optical transmission of pelargonium plasma polymer films deposited at 10 W and 100 W.

In order to determine the electric behavior of pelargonium plasma polymer films, capacitance data, shown in Figure V.1.4, were acquired using LCR records across frequencies from 10 Hz to 100 KHz. It is clear that the capacitance initially decreases at low frequencies ($C \approx 10^{-11}$), approaching a constant value ($C \approx 10^{-10}$) at high frequencies for all measured samples. Independent of frequency, deposition power had a slight influence on the capacitance of pelargonium plasma polymer films. Then, based on capacitance values, the dielectric properties (ε) of the polymers were attained and are given in Table 1 as a function of frequency. The dielectric constant value of pelargonium plasma polymer thin films ostensibly decreased as input deposition power increased. This decrease can be associated with the increase in carbon and reduction in oxygen content in the films' structure with RF power [36]. In addition, it was documented that higher input powers increase the degree of cross-linking that render the polymer more dense, reducing the dielectric property and leakage current density [44].

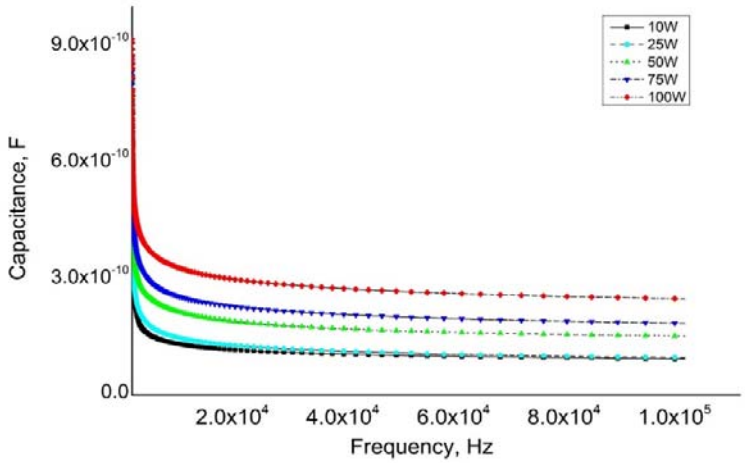

Figure V.1.4. Capacitance of plasma-polymerised pelargonium thin films fabricated at different deposition power as a function of frequency in the range of 10–100 kHz.

Table V.1.1. Variation of the corresponding dielectric constants with frequency for pelargonium plasma polymer thin films in the range of 10–100 kHz.

Frequency (Hz)	Dielectric Constant				
	10 W	**25 W**	**50 W**	**75 W**	**100 W**
10	5.75	4.92	4.74	4.62	4.29
100	4.73	4.10	3.38	2.97	2.56
500	4.48	3.88	3.03	2.62	2.20
1000	4.40	3.80	2.93	2.52	2.10
10,000	4.17	3.59	2.66	2.26	1.85
50,000	3.69	3.24	2.37	1.98	1.59
100,000	3.05	2.78	2.04	1.68	1.32

Independent of deposition power, all of the samples have approximately the same frequency dependence of the dielectric constant, which noticeably decreases at initial low frequencies. In dielectric materials, there are some trapped charges that can typically move for a short distance through the material once an external electric field is applied [45]. These carriers can cause space charges and macroscopic field distortions when they are impeded in their motion. It is known that when charge carriers migrate under the impact of an electric field, they most likely become blocked at the electrode–dielectric interface, which causes interfacial polarisation [45,46]. The interfacial polarisation phenomena are characteristically observed in sandwich-type configurations, where they lead to an increase in capacitance of the polymer at low frequencies [47]. This may be one of the explanations for the high value of the dielectric constants experimentally observed in the pelargonium films within the low frequency region. On the other

hand, at higher frequencies, interfacial polarisation effects are significantly less dominant and do not have an important influence on dielectric constant values [44]. The dielectric constant for all polymers gradually decreases at higher frequencies, showing behavioural characteristics of a polymer insulating material.

The charge transport mechanism in pelargonium plasma polymer films was investigated through standard current–voltage characterisation in the voltage range of 0.1–20 V. The three main transport mechanisms typically observed in organic films are Richardson–Schottky (RS) conduction, Poole–Frenkel (PF) conduction, and space-charge-limited conduction (SCLC). The PF mechanism refers to a bulk-limited conduction route in which the trap barrier of the material is dropped by the application of an adequately high electric field [35]. The RS conduction designates a barrier-limited conduction route, in which there is an interaction of an electric field at a metal–insulator edge that prompts a dropping of the potential barrier [48]. SCLC is a mechanism where the current conducted through the solid material is limited by a distribution of traps in the bulk material [36]. Theoretically, a linear dependence of ln J−ln$V$ indicates a possibility of a SCLC mechanism, while a linear dependence of ln J−$V^{1/2}$ points toward a predominance of RS or PF conduction [49]. In the low field region, various mechanisms most likely govern the conduction process of the polymer, whereas, at higher fields, one mechanism starts to dominate [35].

The physical relationship between the current density (J) in an insulator and the applied voltage (V) at a temperature T is given by the following mathematical formula [36,50]:

$$J = J_0 \exp\left(\frac{\beta V^{0.5}}{K_B T d^{0.5}}\right)$$

where J_0 is the low field current density, V is the voltage, T is the absolute temperature, k_B is Boltzmann's constant, and d is the film thickness. The parameter β is the field dropping coefficient and for PF and RS conduction mechanisms is given by β_{PF} and β_{RS}, respectively [51], expressed as follows:

$$2\beta_{RS} = \beta_{PF} = \left(\frac{q^3}{\pi \varepsilon_0 \varepsilon_r}\right)^{\frac{1}{2}}$$

where q is the electronic charge, ε_0 is the free space permittivity, and ε_r is the dielectric constant.

The relation between the current density of pelargonium plasma polymer films with an applied voltage of 0–20 V is given in figure V.1.5. The J–V characteristic can be expressed by a power law relation $J \propto V^n$, where n is a power law index. In the low field region (0–3 V), the value of n for all pelargonium films is found to be within the range of $0.4 < n < 0.6$. Further, the plots of ln$J$ vs. $V^{1/2}$ with an applied voltage in figure V.1.6 show that the current density J displays an almost

ohmic dependence on the applied voltage in the low region. Whereas in the higher field region (3–20 V), the value of n is considerably increased, ranging within $2.1 < n < 3.3$, and ln J is straight to $V^{1/2}$, indicating a non-ohmic charge transport process. In addition, the fitting of ln J vs. ln$V$ for all pelargonium plasma polymer films in figure V.1.7 demonstrate similar behaviour as those in figure V.1.6. According to power law index values and the linear fitting of the J–V plots, RS or PF conduction mechanisms are expected for geranium thin films.

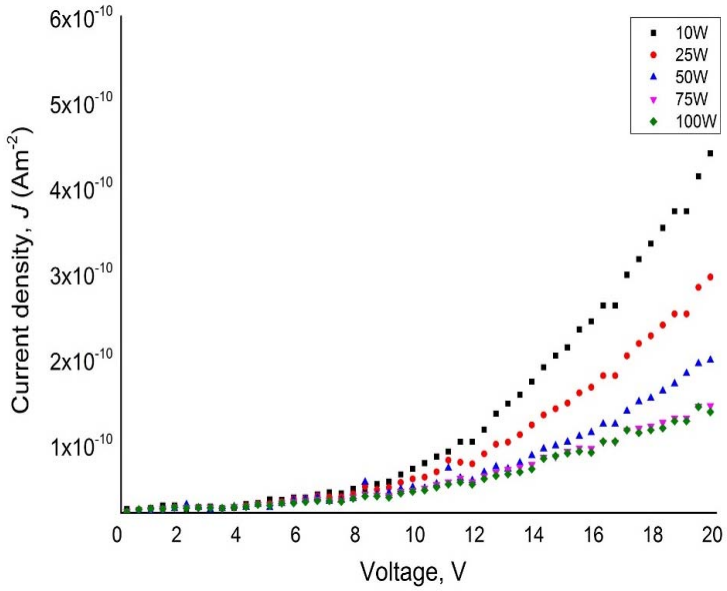

Figure V.1.5. Current density (J) of pelargonium plasma polymer thin films with an applied voltage (V) between 0 and 20 V.

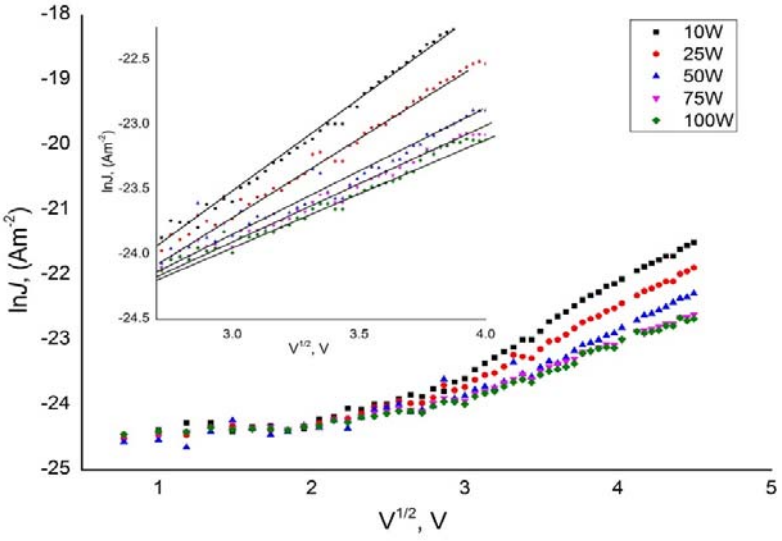

Figure V.1.6. Variation of ln *J* with square root of applied voltage for pelargonium plasma polymer thin films fabricated at different deposition powers.

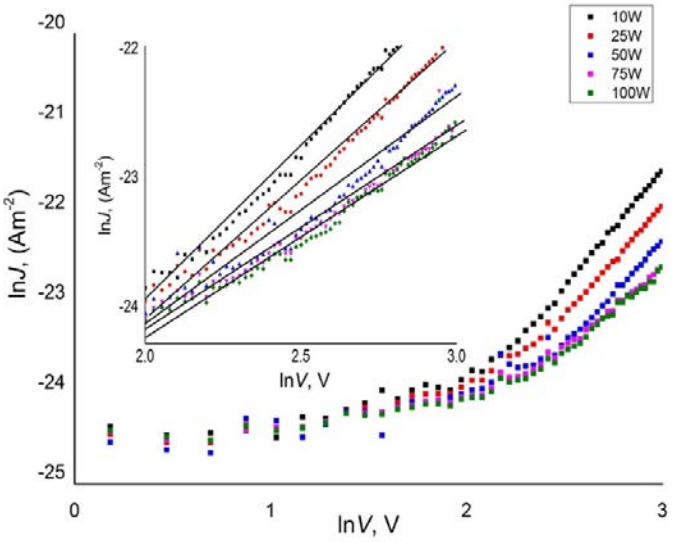

Figure V.1.7. Variation of ln *J* with ln *V* for pelargonium plasma polymer thin films fabricated at different deposition powers.

In order to distinguish between PF and RS mechanisms, theoretical parameters (β_S and β_{PF}) and experimental β_{exp} should be determined. The following relation was used to estimate β_{exp} [35]:

$$\beta_{exp} = SKTd^{\frac{1}{2}}. \quad (1)$$

Using the dielectric value acquired at high frequencies, both β_S and β_{PF} were calculated as ~2.2 × 10^{-5} eV·m$^{1/2}$·$V^{-1/2}$ and 4.4 × 10^{-5} eV·m$^{1/2}$·$V^{-1/2}$, respectively, and summarised in Table 2. Likewise, the coefficient β_{exp} were determined to be around 2.5 × 10^{-5} eV·m$^{1/2}$·$V^{-1/2}$. Hence, by comparing β_S and β_{PF} with the β_{exp} coefficient, the Schottky mechanism might dominate the charge transport of pelargonium plasma polymer films in the higher field region.

Table V.1.2. Experimental β_{exp} and theoretical β_{PF} and β_{RS} values of pelargonium plasma polymer films.

Power of Deposition (W)	β_{exp}	β_{PF}	β_{RS}
10	2.53 × 10^{-5}	4.32 × 10^{-5}	2.16 × 10^{-5}
25	2.55 × 10^{-5}	4.40 × 10^{-5}	2.20 × 10^{-5}
50	2.58 × 10^{-5}	4.42 × 10^{-5}	2.21 × 10^{-5}
75	2.59 × 10^{-5}	4.45 × 10^{-5}	2.22 × 10^{-5}

100	2.61×10^{-5}	4.46×10^{-5}	2.23×10^{-5}

The current–voltage characterisation was then used to estimate the dc conductivity (σ) of the polymerised films through the following relation:

$$\sigma = \frac{Jd}{V}$$

where d is the thickness of the material, J is the measured current density, and V is the applied voltage. Independent of the power of deposition, the maximum conductivity for all samples was found to be in the range of 10^{-16}–10^{-17} Ω^{-1} m^{-1}, which is a typical value for insulators. The deposition power slightly reduced the conductivity value, which can be ascribed to the more amorphous nature of the films deposited at higher power densities [35]. It is important to mention that the difference in the conductivity could not be solely related to structural changes induced by the plasma power. If the SCLC mechanism is responsible for the observed behaviour of the polymer, thickness dependent conductivity may appear as well. However, the conductivity of the plasma-polymer-derived films was significantly lower than that of other known amorphous polymers fabricated using plasma. Generally, plasma polymers derived from essential oil such as *cis*-β-ocimene, γ-terpinene, and linalyl acetate have conductivities in the range of 10^{-12}–10^{-11} $\Omega^{-1}\cdot m^{-1}$ [35,52,53].

V.1.4. Conclusions

The electrical properties of thin films derived from plasma-polymerised Pelargonium graveolens (geranium) were studied across frequencies of 10 Hz to 100 KHz in metal–insulator–metal (MIM) structures for several plasma input powers. The dielectric constant was observed to decrease with increasing deposition power, which can be attributed to the increase in carbon rate and the reduction in oxygen content in the formed films. Regardless of the input power, all investigated samples have approximately the same frequency dependence on the dielectric constant, where it rapidly decreases within a low frequency region. Furthermore, the charge transport mechanism was investigated through a standard current–voltage characterisation, showing that the Schottky mechanism might be the dominant mechanism in the higher field region. These polymers revealed a relatively low conductivity value (10^{-16}–10^{-17} Ω^{-1} m^{-1}), demonstrating characteristics of a typical insulator material. The aforementioned properties, in addition to other advantageous characteristics of geranium plasma polymer thin films (e.g., low density, high adhesion to substrates, relatively high optical band gap, and uniform coverage), render them a suitable candidate for various dielectric applications in advanced microelectronics.

References

1. Yim, J.H.; Joe, S.-Y.; Pang, C.; Lee, K.M.; Jeong, H.; Park, J.-Y.; Ahn, Y.H.; de Mello, J.C.; Lee, S. Fully solution-processed semitransparent organic solar cells with a silver nanowire cathode and a conducting polymer anode. *ACS Nano* **2014**, *8*, 2857–2863.
2. Tseng, H.R.; Phan, H.; Luo, C.; Wang, M.; Perez, L.A.; Patel, S.N.; Ying, L.; Kramer, E.J.; Nguyen, T.Q.; Bazan, G.C.; et al. High-Mobility Field-Effect Transistors Fabricated with Macroscopic Aligned Semiconducting Polymers. *Adv. Mater.* **2014**, *26*, 2993–2998.
3. He, Z.; Xiao, B.; Liu, F.; Wu, H.; Yang, Y.; Xiao, S.; Wang, C.; Russell, T.P.; Cao, Y. Single-junction polymer solar cells with high efficiency and photovoltage. *Nat. Photonics* **2015**, *9*, 174–179.
4. Moon, H.; Seong, H.; Shin, W.C.; Park, W.-T.; Kim, M.; Lee, S.; Bong, J.H.; Noh, Y.-Y.; Cho, B.J.; Yoo, S.; et al. Synthesis of ultrathin polymer insulating layers by initiated chemical vapour deposition for low-power soft electronics. *Nat. Mater.* **2015**, *14*, 628–635.
5. Ortiz, R.P.; Facchetti, A.; Marks, T.J. High-k organic, inorganic, and hybrid dielectrics for low-voltage organic field-effect transistors. *Chem. Rev.* **2009**, *110*, 205–239.
6. Kumar, B.; Kaushik, B.K.; Negi, Y. Perspectives and challenges for organic thin film transistors: Materials, devices, processes and applications. *J. Mater. Sci. Mater. Electron.* **2014**, *25*, 1–30.
7. Liu, X.; Guo, Y.; Ma, Y.; Chen, H.; Mao, Z.; Wang, H.; Yu, G.; Liu, Y. Flexible, Low-Voltage and High-Performance Polymer Thin-Film Transistors and Their Application in Photo/Thermal Detectors. *Adv. Mater.* **2014**, *26*, 3631–3636.
8. Choi, J.; Joo, M.; Seong, H.; Pak, K.; Park, H.; Park, C.W.; Im, S.G. Flexible, Low-Power Thin-Film Transistors (TFTs) Made of Vapor-Phase Synthesized High-k, Ultrathin Polymer Gate Dielectrics. *ACS Appl. Mater. Interfaces* **2017**, *9*, 20808–20817.
9. Facchetti, A.; Yoon, M.H.; Marks, T.J. Gate Dielectrics for Organic Field-Effect Transistors: New Opportunities for Organic Electronics. *Adv. Mater.* **2005**, *17*, 1705–1725.
10. Cheng, X.; Caironi, M.; Noh, Y.-Y.; Wang, J.; Newman, C.; Yan, H.; Facchetti, A.; Sirringhaus, H. Air stable cross-linked Cytop ultrathin gate dielectric for high yield low-voltage top-gate organic field-effect transistors. *Chem. Mater.* **2010**, *22*, 1559–1566.
11. Eslamian, M. Inorganic and organic solution-processed thin film devices. *Nano-Micro Lett.* **2017**, *9*, 3.
12. Friedrich, J. Mechanisms of Plasma Polymerization—Reviewed from a Chemical Point of View. *Plasma Process. Polym.* **2011**, *8*, 783–802.
13. Boscher, N.D.; Hilt, F.; Duday, D.; Frache, G.; Fouquet, T.; Choquet, P. Atmospheric Pressure Plasma Initiated Chemical Vapor Deposition Using Ultra-Short Square Pulse Dielectric Barrier Discharge. *Plasma Process. Polym.* **2015**, *12*, 66–74.

14. Hilt, F.; Duday, D.; Gherardi, N.; Frache, G.; Didierjean, J.; Choquet, P. Plasma polymerisation of an allyl organophosphate monomer by atmospheric pressure pulsed-PECVD: Insights into the growth mechanisms. *RSC Adv.* **2015**, *5*, 4277–4285.
15. Flamm, D.L.; Auciello, O. *Plasma Deposition, Treatment, and Etching of Polymers: The Treatment and Etching of Polymers*; d'Agostino, R, Ed.; Academic Press: San Diego, CA, USA; 2012.
16. Bhattacharyya, D.; Yoon, W.-J.; Berger, P.R.; Timmons, R.B. Plasma-Polymerized Multistacked Organic Bipolar Films: A New Approach to Flexible High-κ Dielectrics. *Adv. Mater.* **2008**, *20*, 2383–2388.
17. Xu, Y.; Berger, P.R. Pulsed plasma polymerized dichlorotetramethyldisiloxane high-k gate dielectrics for polymer field-effect transistors. *J. Appl. Phys.* **2006**, *99*, 014104.
18. Lim, J.-S.; Shin, P.-K.; Lee, B.-J. Organic Thin Film Transistors with Gate Dielectrics of Plasma Polymerized Styrene and Vinyl Acetate Thin Films. *Trans. Electric. Electron. Mater.* **2015**, *16*, 95–98.
19. Feng, L.; Anguita, J.V.; Tang, W.; Zhao, J.; Guo, X.; Silva, S.R.P. Room Temperature Grown High-Quality Polymer-Like Carbon Gate Dielectric for Organic Thin-Film Transistors. *Adv. Electron. Mater.* **2016**, *2, 1500374*.
20. Tsai, C.H.; Li, Y.-S.; Cheng, I.-C.; Chen, J.-Z. O2/HMDSO-Plasma-Deposited Organic–Inorganic Hybrid Film for Gate Dielectric of MgZnO Thin-Film Transistor. *Plasma Process. Polym.* **2014**, *11*, 89–95.
21. Lim, J.-S.; Shin, P.-K.; Lee, B.-J.; Lee, S. Plasma polymerized methyl methacrylate gate dielectric for organic thin-film transistors. *Org. Electron.* **2010**, *11*, 951–954.
22. Yoon, W.-J.; Bhattacharyya, D.; Timmons, R.B.; Berger, P.R. Plasma-polymerized multistacked bipolar gate dielectric for organic thin-film transistors. *Org. Electron.* **2010**, *11*, 1767–1771.
23. Jacob, M.V.; Bazaka, K.; Weis, M.; Taguchi, D.; Manaka, T.; Iwamoto, M. Fabrication and characterization of polyterpenol as an insulating layer and incorporated organic field effect transistor. *Thin Solid Films* **2010**, *518*, 6123–6129.
24. Kwok, H.S.; Wong, M.; Peng, H.; Sun, J. Metallic Anode Treated by Carbon Tetrafluoride Plasma for Organic Light Emitting Device. U.S. Patent 9,166,197 B2, 20 October 2015.
25. Zhu, H.; Luo, W.; Ciesielski, P.N.; Fang, Z.; Zhu, J.Y.; Henriksson, G.; Himmel, M.E.; Hu, L. Wood-derived materials for green electronics, biological devices, and energy applications. *Chem. Rev.* **2016**, *116*, 9305–9374.
26. Irimia-Vladu, M. "Green" electronics: Biodegradable and biocompatible materials and devices for sustainable future. *Chem. Soc. Rev.* **2014**, *43*, 588–610.

27. Irimia-Vladu, M.; Głowacki, E.; Voss, G.; Bauer, S.; Sariciftci, N.S. Green and biodegradable electronics. *Mater. Today* **2012**, *15*, 340–346.
28. Zhu, Y.; Romain, C.; Williams, C.K. Sustainable polymers from renewable resources. *Nature* **2016**, *540*, 354–362.
29. Bazaka, K.; Jacob, M. Synthesis of radio frequency plasma polymerized non-synthetic Terpinen-4-ol thin films. *Mater. Lett.* **2009**, *63*, 1594–1597.
30. Jacob, M.V.; Rawat, R.S.; Ouyang, B.; Bazaka, K.; Kumar, D.S.; Taguchi, D.; Iwamoto, M.; Neupane, R.; Varghese, O.K. Catalyst-free plasma enhanced growth of graphene from sustainable sources. *Nano Lett.* **2015**, *15*, 5702–5708.
31. Bazaka, K.; Jacob, M.V.; Ostrikov, K. Sustainable Life Cycles of Natural-Precursor-Derived Nanocarbons. *Chem. Rev.* **2016**, *116*, 163–214.
32. Al-Jumaili, A.; Alancherry, S.; Bazaka, K.; Jacob, M.V. Review on the antimicrobial properties of carbon nanostructures. *Materials* **2017**, *10*, 1066.
33. Jacob, M.V.; Easton, C.D.; Woods, G.S.; Berndt, C.C. Fabrication of a novel organic polymer thin film. *Thin Solid Films* **2008**, *516*, 3884–3887.
34. Anderson, L.; Jacob, M. Effect of RF power on the optical and morphological properties of RF plasma polymerised linalyl acetate thin films. *Appl. Surf. Sci.* **2010**, *256*, 3293–3298.
35. Anderson, L.; Jacob, M. Electrical characterisations of plasma polyermised linalyl acetate. *Mater. Sci. Eng. B* **2012**, *177*, 311–315.
36. Ahmad, J.; Bazaka, K.; Vasilev, K.; Jacob, M.V. Electrical conduction in plasma polymerized thin films of γ-terpinene. *J. Appl. Polym. Sci.* **2015**, *132*, doi:10.1002/app.42318.
37. Bazaka, K.; Jacob, M.V.; Crawford, R.J.; Ivanova, E.P. Plasma-assisted surface modification of organic biopolymers to prevent bacterial attachment. *Acta Biomater.* **2011**, *7*, 2015–2028.
38. Bazaka, K.; Jacob, M.V.; Bowden, B.F. Optical and chemical properties of polyterpenol thin films deposited via plasma-enhanced chemical vapor deposition. *J. Mater. Res.* **2011**, *26*, 1018–1025.
39. Jacob, M.V.; Bazaka, K.; Taguchi, D.; Manaka, T.; Iwamoto, M. Electron-blocking hole-transport polyterpenol thin films. *Chem. Phys. Lett.* **2012**, *528*, 26–28.
40. Ahmad, J.; Bazaka, K.; Jacob, M.V. Optical and surface characterization of radio frequency plasma polymerized 1-isopropyl-4-methyl-1, 4-cyclohexadiene thin films. *Electronics* **2014**, *3*, 266–281.
41. Ahmad, J.; Bazaka, K.; Whittle, J.D.; Michelmore, A.; Jacob, M.V. Structural Characterization of γ-Terpinene Thin Films Using Mass Spectroscopy and X-ray Photoelectron Spectroscopy. *Plasma Process. Polym.* **2015**, *12*, 1085–1094.

42. Vassallo, E.; Cremona, A.; Ghezzi, F.; Laguardia, L.; Ambrosone, G.; Coscia, U. Structural and optical properties of amorphous hydrogenated silicon carbonitride films produced by PECVD. *Appl. Surf. Sci.* **2006**, *252*, 7993–8000.
43. Al-Jumaili, A.; Bazaka, K.; Jacob, M.V. Retention of Antibacterial Activity in Geranium Plasma Polymer Thin Films. *Nanomaterials* **2017**, *7*, 270.
44. Bazaka, K., Destefani, R.; Jacob, M.V. Plant-derived cis-β-ocimene as a precursor for biocompatible, transparent, thermally-stable dielectric and encapsulating layers for organic electronics. *Sci. Rep.* **2016**, *6*, 38571.
45. Kumar, D.S. Yoshida, Y. Dielectric properties of plasma polymerized pyrrole thin film capacitors. *Surf. Coat. Technol.* **2003**, *169*, 600–603.
46. Chowdhury, F.-U.-Z.; Bhuiyan, A. Dielectric properties of plasma-polymerized diphenyl thin films. *Thin Solid Films* **2000**, *370*, 78–84.
47. Mathai, C.J.; Saravanan, S.; Anantharaman, M.R.; Venkitachalam, S.; Jayalekshmi, S. Characterization of low dielectric constant polyaniline thin film synthesized by ac plasma polymerization technique. *J. Phys. D Appl. Phys.* **2002**, *35*, 240–245.
48. Bazaka, K.; Jacob, M.V. Effects of iodine doping on optoelectronic and chemical properties of polyterpenol thin films. *Nanomaterials* **2017**, *7*, 11.
49. Matin, R.; Bhuiyan, A. Electrical transport mechanism in plasma polymerized 2, 6, diethylaniline thin films. *Thin Solid Films* **2011**, *519*, 3462–3467.
50. Dakhel, A. Mechanisms of dc-current transfer in tris (acetylacetonato) iron (III) films. *J. Non-Cryst. Solids* **2007**, *353*, 1529–1533.
51. Capan, R.; Davis, F. Electrical properties of a calix [4] acid/amine Langmuir–Blodgett thin film. *Mater. Chem. Phys.* **2011**, *125*, 883–886.
52. Bazaka, K.; Jacob, M.V. Complex permittivity measurements of RF plasma polymerized polyterpenol organic thin films employing split post dielectric resonator. *J. Polym. Eng.* **2011**, *31*, 73–75.
53. Kiesow, A.; Heilmann, A. Deposition and properties of plasma polymer films made from thiophenes. *Thin Solid Films* **1999**, *343*, 338–341.

Chapter V

Part 2

The Electrical Properties of ZnO Incorporated into Geranium Polymer Films

The electrical properties of ZnO incorporated into geranium polymer films were studied with the intention to produce nanocomposite thin coatings that are electrically insulated and biologically active material for encapsulation of microelectronics and implantable devices. The electrical properties of pristine polymers and Zn/polymers composites films deposited at 10 and 50 W input RF powers were investigated using metal–insulator–metal structures and reported in this session (chapter V-part 2).

Abstract

Metal/polymer coatings that have distinct tailored electrical properties in addition to chemical, physical and/or bio-response characteristics is important to develop various applications. In this report, the electrical properties of ZnO Nanoparticles (NPs) functionalized plasma polymer films were investigated in order to fulfil the potential applications of the resultant-composites in biomaterials and microelectronics fields. The electrical properties of pristine polymers and Zn/composites films fabricated at 10 and 50 W input RF power levels were studied in metal–insulator–metal structures. At a quantity of ZnO around ˜1%, it was found that ZnO had small influence on the capacitance and dielectric constants of the fabricated films. The dielectric constant of smaller-sized nanoparticles exhibited the higher value, whereas, with the increase of particle size, the dielectric constant is decrease. The conductivity for the composites were calculated in the in the range of 10^{-14}–$10^{-15}\,\Omega^{-1}\,m^{-1}$, compared to conductivity of 10^{-16}–$10^{-17}\,\Omega^{-1}\,m^{-1}$ for pristine polymer.

V.2.1. Introduction

Recent progresses in material technologies have encouraged the development of various preparation approaches and applications of novel polymer–nanoparticles composites films. These composites are preferred as promising innovative materials owing to their superior characteristics, such as strength, high elastic modulus, great large surface areas, enhanced density, and controlled optoelectronic properties [1, 2]. Metal/plasma polymer composite films have exhibited interesting optical, electrical and biological properties [3]. Nanocomposites remarkably merge advantages of low-dimensional organic films with a great surface area of embedded nanoparticles, offering a

wide range of possible applications such as photoactive layers on the surface of the solar panels, transparent conductive coatings, and antibacterial surfaces for medical implants [4, 5]. A specific application highly depends on broad polymer properties and unique surface electronic structure of embedded nanoparticles.

Manufacturing of matrix-polymers and their resultant-composites from natural resources is highly recommended from environmental point of view [6]. The material can be derived from a wide range of renewable precursors such as planet essential oils. Essential oils are relatively low-cost, available in commercial amounts, and offer minimal toxicity compared to various typically-used precursors [7, 8]. Current progress in plasma enhanced chemical vapor deposition convert essential oils into cost-effective ultra-thin layers with the possibility to incorporate metallic nanoparticles in the plasma polymer thin films [9, 10]. It allows good control over film thickness, physical-chemical characteristics, and biological functionality [11-13]. Nevertheless, donating nanoparticles into plasma polymers give the potential for providing a variety of properties to the resultant polymer-matrix composites. In particular, electrical characteristics of composite films critically rely on both the metal volume fraction and the polymer configuration. The doping level of composite films is typically determined by the filling factor [14, 15]. The variation in electrical properties of such composites as a function of the filling factor has been explained in the literature through percolation theories [16].

In our previous study, a novel nanocomposite film was fabricated from ZnO NPs and renewable geranium oil using a single-step plasma approach [17]. We demonstrated that a significant antibacterial activities can be achieved by incorporating ˜1% zinc oxide nanoparticles in geranium thin films. In this manuscript we investigated the electrical properties of ZnO/geranium polymer (Zn/Ge) films with the intention to design composite coatings that are electrically insulated and biologically active material for encapsulation of microelectronics and implantable devices. Amongst various fillers nanoparticles, zinc oxide (ZnO) was selected in our research due to its desired antibacterial properties. The optical transparency, good stability at high temperature and inherent ability to absorb UV, beside bio-safety and powerful antimicrobial activity, ZnO nanoparticles are considered to be one of the most potential substance in the manufacturing of microelectronic and coatings for advanced biomedical applications [18, 19].

V.2.2. Experimental:

V.2.2.1 Precursor materials

Geranium essential oil (secondary plant metabolites) was purchased from Australian Botanical Products (ABP, Victoria, Australia). As documented by the manufacturer, geranium oil had various components including citronellol (32%), geraniol (15%), linalool (6%), and

isomenthone (6%). Geranium essential oil was selected as precursor due to its high volatile property at room temperature, which ensure no external heating nor carrier gases to curry the precursor gas to the fabrication chamber. It was used if the fabrication without further modification.

Zinc nanoparticles were formed from commercially available zinc acetylacetonate $Zn(acac)_2$ (Sigma-Aldrich, Germany) and was used without further modification/purification. $Zn(acac)_2$ compound was nominated owing to its relatively low decomposition temperature and ability to integrate in gas-phase catalyst-free nanoparticle formation in plasma polymer system.

V.2.2.2 Material fabrication

Prior to samples fabrication, microscope glass substrates (76 mm × 26 mm) were cleaned and sonicated in a solution of water and commercial decon for 20 min. Then, substrates rinsed in acetone and dried using compressed air. Aluminum electrodes were fabricated onto the glass slides using thermal evaporation system (HINDHIVAC 12A4D) at a pressure of 7×10^{-5} torr. Pristine polymers and ZnO/polymer thin films were fabricated on the aluminum layer employing modified-plasma-enhanced chemical vapor deposition (M-PECVD) system (MKS Instruments, Andover, MA, USA). A RF generator is used to deliver radio frequency power at 13.56 MHz to a glass tube via external coupled copper electrodes. In the case of composite fabrication, the plasma system was supplemented with an external heater to achieve thermal decomposition of $Zn(acac)_2$ powder (0.05 g), which was placed inside the plasma system. ZnO nanoparticles were generated in the gas phase and inserted into the polymer medium during the growing of the polymer chains. However, a quantity of 0.5 g of geranium oil was used in each deposition that yield a flow rate of ~16 cm^3/min and a film thickness in a range ~500–700 nm. Finally, another aluminum electrode was made on top of the organic layers using a home-made shadow mask that manufactured a device with metal–insulator–metal (MIM) structures as presented in figure V.2.1.

All thin films were derived from geranium essential oil at input powers 10 W and 50 W, and the resulting pristine polymers were abbreviated as Ge 10 W and Ge 50 W, while the counterpart ZnO-polymers were abbreviated as Zn/Ge 10 W and Zn/Ge 50 W, respectively.

V.2.2.3 Electrical measurements

Dielectric properties of the resultant MIM device were investigated between frequencies of 10 Hz and 100 KHz using a Hioki 3522 LCR meter (Hioki, Ueda, Japan). As we identified the thickness and area of the device, and measured C values, dielectric constant was calculated. Besides, current—voltage (*I–V)* measurements were obtained on the MIM structures

employing a Keithley 2636A source meter (Keithley, Cleveland, OH, USA). Data were recorded between 0 and 20 V, with steps of 0.2 V for each point at room temperature.

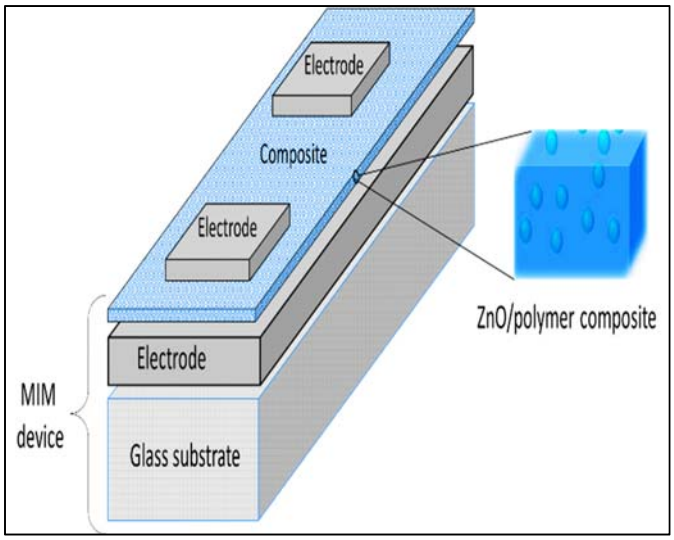

Figure V.2.1. Metal–insulator–metal (MIM) device that designed to investigate the electrical properties of ZnO/geranium plasma polymer composite films.

V.2.3. Results and discussion

The ZnO/geranium plasma polymer composite films were fabricated using the modified PECVD system. Figure V.2.2 (a) clearly shows that ZnO NPs were formed in ball-like-structure. The average nano-particle size is 60 nm and 80 nm for samples fabricated at 10 W and 50 W, respectively. Furthermore, we observed some of unavoidable clusters of nanoparticles within polymers due to high cohesive energy of metals, as seen figure V.2.2 (b). These aggregations statistically represented less than 10 % of the over-all number of nanoparticles. Full scan XPS spectra of ZnO/polymer composite films given in figure V.2.2 (c) evidently showed the incorporation of ZnO in the geranium polymer structure. It shows the presence of symmetrical zinc oxide at binding energies of 1021.32 and 1044.60 eV, where zinc oxide had significantly split spin-orbit components (Δ_{metal}=23 eV). Also, carbon, oxygen, and nitrogen were observed in the chemical structure of the composites. XPS indicated that carbon is dominated the films with atomic concentrations of 83 %, and oxygen and nitrogen are around 13 % and 3 %, respectively. Zinc was revealed to be 1 %. The element atomic concentrations in the composites were found to slightly vary as a function of the deposition power. AFM image in figure V.2.2 (d) shows the porous surface with random distribution of ZnO NPs, as the average roughness was at 33.7 ± 2.1 for input power of 10 W. Figure V.2.2 (e) shows the bacterial viability of gram-negative *E. coli* cells on the control, pristine and composite films. It was found that 81% of *E. coli* cells were viable on the control surface, while the viability of cells were decreased on other samples showing approximately 60%, 76%, 33% and 44% on Ge 10 W, Ge 50 W, Zn/Ge 10 W and Zn/Ge 50 W,

respectively. This outcome indicates a significant antibacterial perform of Zn/Ge 10 W sample owing to presents ZnO-NPs in the polymer. However, further details regarding the release of ZnO NPs and morphological, surface, chemical and antimicrobial properties of Zn/Ge composites films can be found in our previous study [17].

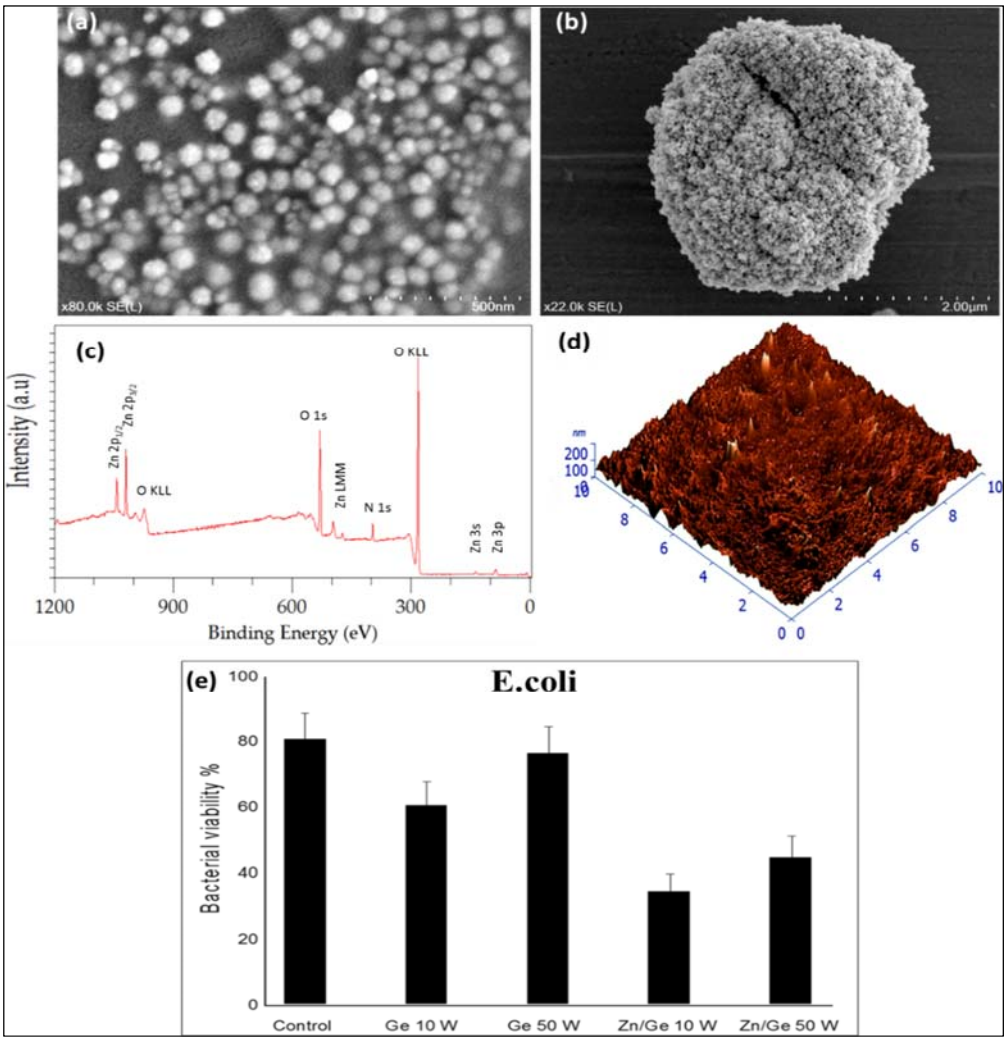

Figure V.2.2. Display a number of properties recorded for ZnO/geranium plasma polymer films. (a) SEM images of ZnO-NPS acquired at magnification of x80K. (b) SEM images of aggregation of some ZnO-NPs. (c) Full scan XPS spectrum of ZnO/geranium plasma polymer films. (d) Three-dimensional AFM image of the composite surface measured at scanning area of 10 µm × 10 µm. (e) Bar chart of the bacterial viability of *E.coli cells* (cultured for 24 h at 37 °C) on surfaces of pristine polymers and ZnO/polymers composites. The control is sterilized cover glass substrates.

The electrical properties of the composite film is studied understand the feasibility of manufacturing of encapsulation coatings for microelectronics and medical implantable devices.

The electric characteristics of pristine and composite polymer films were measured using capacitance measurements of the M-I-M structure. The data were acquired utilizing LCR device in the frequency range 10 Hz and 100 KHz. In figure V.2.3, it can be seen that the capacitance values for pristine and composites films were approximately 10^{-9} and 10^{-10} F, which sharply decreases at low frequencies, approaching a constant value around 10^{-10} F at high frequencies for all measured films. Independent of frequency, ZnO nanoparticles and deposition power had minor effect on the capacitance of the pristine and composites films.

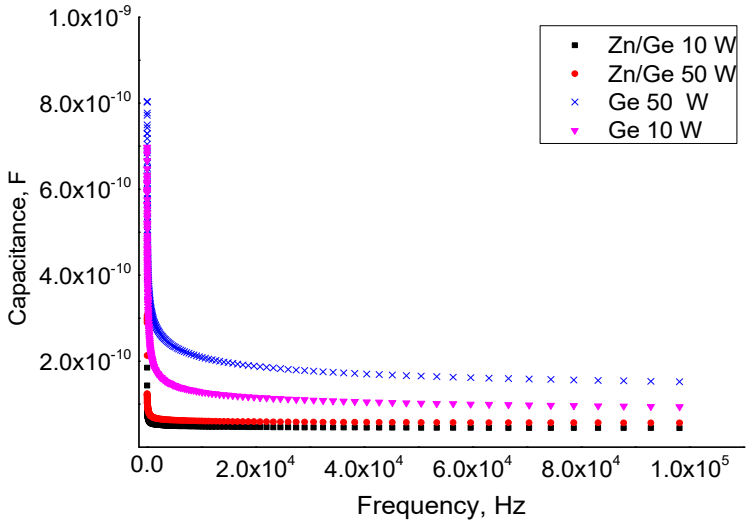

Figure V.2.3. Capacitance of pristine and composites plasma- geranium thin films fabricated at 10 W and 50 W as a function of frequency in the range of 10–100 kHz.

Table V.2.1. Variation of the dielectric constants of pristine and composites plasma geranium thin films fabricated at 10 W and 50 W with applied frequency in the range of 10–100 kHz.

Frequency (Hz)	**Dielectric Constant**			
	10 W	50 W	Zn/Ge 10 W	Zn/Ge 50 W
10	5.75	4.74	4.12	4.04
100	4.73	3.38	3.57	3.87
500	4.48	3.03	3.42	3.72
1000	4.4	2.93	3.37	2.64
10,000	4.17	2.66	2.06	2.35
50,000	3.69	2.37	2.98	2.73
100,000	3.05	2.04	2.78	2.42

The subsequent dielectric constant of the pristine and composite was calculated in table V.2.1 as a function of frequency. The dielectric constant decreases with the increase of frequency for all samples for different power of deposition. At the high frequency range (10^4 Hz), the decreasing trend is not too sharp as compared with the lower frequency region. The decrease in trend is more noticeable in ZnO/Ge composite films, since the inherent dielectric constant tendency of ZnO nanoparticles also decreases with increasing frequencies of the applied voltage. However, no percolation behavior was observed for the permittivity, which was observed in other studies for ZnO nanoparticles integrated with polymers [20].

SEM images showed that the ZnO nanoparticles are not uniformally distributed, but rather touching other particles creating interfaces between ZnO nanoparticles. It had been hypothesized that the interface dipole moments originate from the electrons that are trapped at the ZnO/ZnO interface electronic states [20]. The energy levels of ZnO/ZnO are different from those of ZnO/polymer interface states, where the electrons in those states respond to different frequencies. Hence, the interface dipoles related to ZnO/ZnO interfaces are possibly responsible for the variation in the dielectric constant values especially at low frequencies.

In order to theoretically estimate the dielectric constant of pure ZnO nanoparticles (apart from polymer), we used the modified Rother–Lichtenecker equation. The measured dielectric constant is given by the relation [21]:

$$\varepsilon_{measured} = \exp\left[\ln \varepsilon_1 + f_2(1-k)\ln(\varepsilon_2/\varepsilon_1)\right]$$

where $\varepsilon_{measured}$, ε_1, and ε_2 represent the dielectric constant of the ZnO/Ge composite, the polymer medium, and the ZnO nanoparticle, respectively, f_2 represents the volume fraction of the ZnO nanoparticle, and k is the shape dependent factor ($k = 0.5$).

Considering the differences in the particles size as ~ 60 nm formed at 10 W and ~ 80 nm formed at 50 W, the dielectric constant for ZnO NPs was evaluated at room temperature to be ε= 6.7 and ε=6.1, respectively. It can be understood that dielectric constant of smaller-sized nanoparticles exhibited higher value, whereas, with increase of particle size, the dielectric constant decreased. This is in agreement with previous findings [21]. In contrast, other studies reported that dielectric constant increase with increase in the size of nanoparticles [22]. The dielectric constant of pure ZnO NPs can be varied depending on the experimental conditions, for example it was measured to be around ˜10 at high frequency region (for particles size of 20 to 35 nm at 30 ˚C) [23]. The calculated dielectric constant in the current study could be slightly different from the real value. This phenomenon is not strange. It is known that ZnO is a typical metal excess, where oxygen is easily to be adsorbed on the surface of ZnO, resulting in the formation of high resistivity layers (as Schottky barriers) on the surface of the ZnO grains [24]. Larger the ZnO particle, the smaller the ratio of surface area to the particle volume. Accordingly, it retain larger dielectric constant. In

addition, it is worth to mention that Rother–Lichtenecker equation is valid for ideal well-dispersed particles. The non-ideal distribution of nanoparticles through geranium polymers and the dissimilarities, the particles dimension/shape could affect the accuracy of the results.

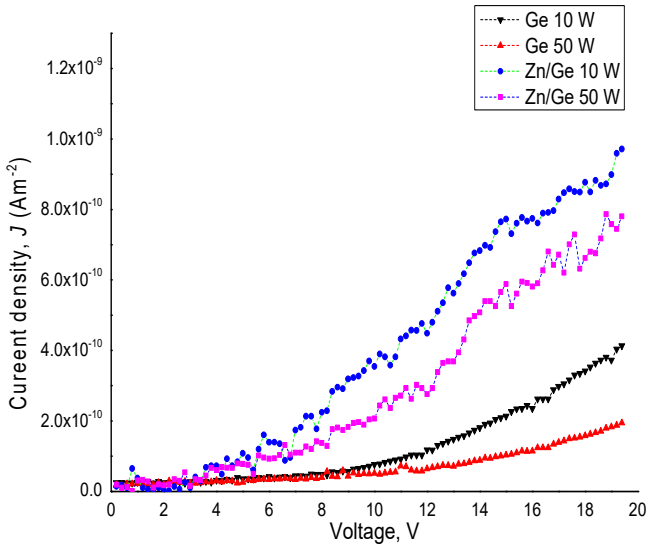

Figure V.2.4. Current density (*J*) of pristine and composites plasma geranium thin films fabricated at 10 W and 50 W as a function of applied voltage (*V*).

Figure V.2.4 displays the variation of current density (*J*) of pristine and ZnO-geranium plasma polymer composite as a function of the applied voltage (*V*) for samples fabricated at 10 W and 50 W. The current density (*J*) of the films is calculated through the following equation [25, 26]:

$$J = J_0 \exp\left(\frac{\beta V^{0.5}}{K_b T d^{0.5}}\right)$$

where J_0 is the low field current density, *V* is voltage, *T* is absolute temperature, k_B is Boltzmann's constant in and *d* is film thickness. The parameter β is the field dropping coefficient for Richardson–Schottky (RS) conduction or Poole–Frenkel (PF) conduction mechanisms, which is given the following equation [27]:

$$2\beta_{RS} = \beta_{PF} = \left(\frac{q^3}{\pi\varepsilon_0\varepsilon_r}\right)^{1/2}$$

where q is the electronic charge, ε_0 is the free space permittivity, ε_r is the dielectric constant, and β_{PF} and β_{RS}, are field dropping coefficient for Poole–Frenkel and Richardson–Schottky conduction respectively.

Dc conductivity (σ) of the pristine and composited films was estimated using the current–voltage data through the relation: $\sigma = Jd/V$, where d is the thickness of the material, J is the measured current density, and V is the applied voltage. The conductivity for the composites were calculated in the in the range of 10^{-14}–10^{-15} Ω^{-1} m^{-1}, compared to pristine polymer that revealed 10^{-16}–10^{-17} Ω^{-1} m^{-1}.

In nanoparticles/polymer composites, there is a critical volume/weight concentration of fillers called percolation threshold. According to the percolation theory, when the content of conductive filler is near the percolation threshold, the fillers connect with each other to build a continuous conducting pathway, providing the potential for electrons/carriers to transport among the fillers [16]. Thus, the composite always reveal a rapid increase in electrical properties [28]. The percolation threshold is determined by the filler shape, size distribution, interlayer thickness, temperature, physicochemical properties, and applied external field [29]. Yet, the relationship between the filler concentration and conductivity of the composite is not fully understood [30].

The conductivity (σ) near the percolation threshold (ϕ_c) can be given by the power law:

$$\sigma_c = \sigma_f(\emptyset_f - \emptyset_c)^t$$

where σ_c is electrical conductivity of the composites, σ_f is the conductivity of the filler, ϕ_f is the volume portion of the filler, ϕ_c is the percolation concentration, t is the critical exponent, which is a parameter determining the power of the conductivity based on ϕ_c. The critical exponent t depends on the system dimension, and is set between 1.6 and 2 for three-dimensional structure. The value of was adjusted until the best linear fit was obtained in *log* σ *vs. log* σ *(* − *)*. The range of critical exponent values fitted from experimental measurements obtained by different studies indicate that the t is not universal, as it varied in the range of 0.9 to 2 [15, 31, 32].

Based on the percolation threshold equation, we estimated the percolation threshold of Zn/Ge composites to be ˜2.67 %. It is clear that the Zn/Ge composites did not show percolation threshold since the conductivity was kept at relatively low values (10^{-14} Ω^{-1} m^{-1}), rather than increases rapidly. The relative increase in conductivity after introducing ZnO NPs could be related to the increase in the number of dipoles, where the reformation of trap structure induced by ZnO nanoparticles. This specifies that the formed composites do not follow the behaviors of systems incorporating 2D or 3D conducting particles, but more complex charge tunneling transport mechanisms are obviously involved in their conductivity [33]. The electrical conduction could also be increased due to the electronic and impurity contributions arising from the zinc precursor during the thermal decomposition of zinc acetylacetonate ($Zn(acac)_2$).

Some studies showed that the percolation threshold for conductivity of ZnO/polymer system to be 15 wt.% of the volume fraction polymer [34]. Different researchers found that the percolation concentration is 2.8 vol%.(ZnO =200 nm) [35], and 0.05 percentage for ZnO nano-rods (d=400 nm and L=2 µm) [36].

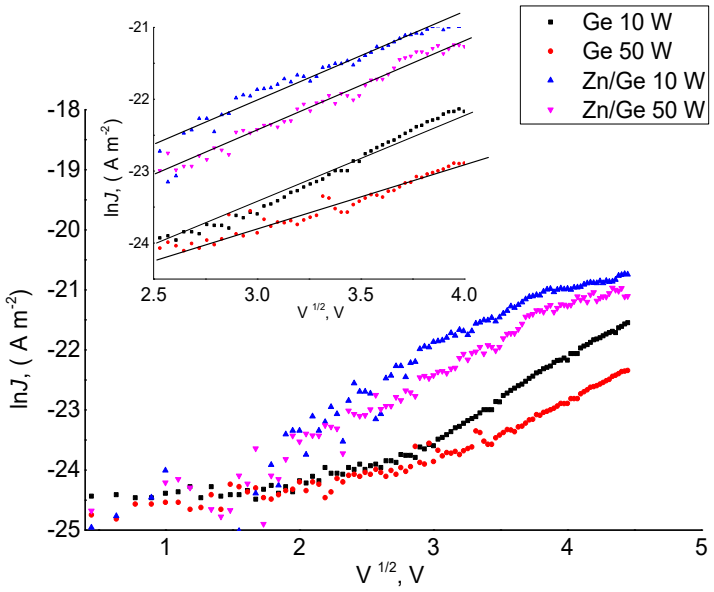

Figure V.2.5. Variation of ln *J* with square root of applied voltage for pristine and composites plasma geranium thin films fabricated at 10 W and 50 W.

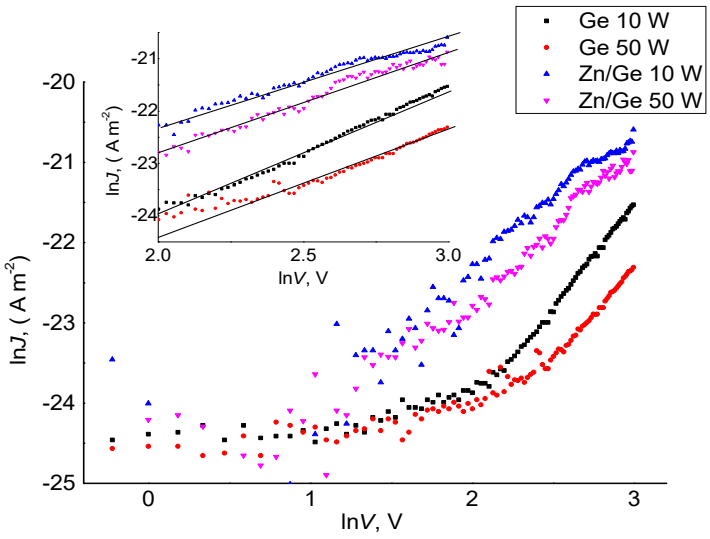

Figure V.2.6 Variation of ln *J* with ln*V* for for pristine and composites plasma geranium thin films fabricated at 10 W and 50 W.

As shown in figure V.2.5 and V.2.6, the fitting result of In (J)–($V^{1/2}$) and ln (J)–ln (V) indicates that the conduction mechanism in the high voltage range could be related to the Richardson–Schottky (RS) or Poole–Frenkel (PF) conduction. Furthermore, the fitting of ln J vs. ln$V$ for all plasma polymer and composites demonstrates similar behavior as those in ln J vs. $V^{1/2}$. According to power law index values and the linear fitting of the J–V plots for pristine polymer that previously reported in [37], the Schottky mechanism might dominate the charge transport of geranium plasma polymer films in the higher field region. This suggests the ZnO NPs do not affect the transport at high field, but may indirectly change the carrier transport properties at lower fields. It is expected since the NP loads used were at low concentration (below the percolation threshold).

V.2.4. Conclusion:

The electrical properties of pristine and ZnO incorporated plasma polymerised geranium oil thin films were studied in the frequency range of 10 Hz to 100 KHz using metal–insulator–metal structures. The dielectric constant was observed to decrease with increasing deposition power for all samples. Regardless of the input power, all investigated samples have approximately the same frequency dependence on the dielectric constant, where it rapidly decreases at the low frequency region. Furthermore, the charge transport mechanism was investigated through a standard current−voltage characterisation, showing Schottky mechanism as a possible dominant mechanism in the higher field region. The material revealed a relatively low conductivity value ($\sim 10^{-16}\,\Omega^{-1}\,m^{-1}$), demonstrating characteristics of a typical insulator. Incorporation of ZnO nanoparticles into the geranium polymer thin films did not change the nature of charge transport, as the nanocomposite films still behave as an insulator. The aforementioned properties, in addition to the antibacterial activities and other advantageous characteristics of Zn/Ge thin films (e.g. low density, high adhesion to substrates, relatively high optical band gap, and uniform coverage) render them as a suitable candidate for various dielectric applications in advanced microelectronics.

References

1. Zhou, M., et al., *Enhancement of Low-field Magnetoresistance in Self-Assembled Epitaxial La0.67Ca0.33MnO3:NiO and La0.67Ca0.33MnO3:Co3O4 Composite Films via Polymer-Assisted Deposition.* Scientific Reports, 2016. **6**: p. 26390.
2. Zhang, R.-C., et al., *Gold nanoparticle-polymer nanocomposites synthesized by room temperature atmospheric pressure plasma and their potential for fuel cell electrocatalytic application.* Scientific Reports, 2017. **7**: p. 46682.

3. Wang, X. and G. Grundmeier, *Thin Functional Plasma Polymer and Metal/Plasma Polymer Nanocomposite Films*. 2007, Ruhr-Universität, Fakultät Maschinenbau, Institut für Werkstoffe Bochum, Germany.
4. Javid, A., et al., *Size-controlled growth and antibacterial mechanism for Cu: C nanocomposite thin films.* Physical Chemistry Chemical Physics, 2017. **19**(1): p. 237-244.
5. Müller, K., et al., *Review on the processing and properties of polymer nanocomposites and nanocoatings and their applications in the packaging, automotive and solar energy fields.* Nanomaterials, 2017. **7**(4): p. 74.
6. Bazaka, K., *Fabrication and characterization of plasma polymer thin films from monoterpene alcohols for applications in organic electronics and biotechnology*. 2011, James Cook University.
7. Al-Jumaili, A., et al., *Plant Secondary Metabolite-Derived Polymers: A Potential Approach to Develop Antimicrobial Films.* Polymers, 2018. **10**(5): p. 515.
8. Duque, L. and R. Förch, *Plasma Polymerization of Zinc Acetyl Acetonate for the Development of a Polymer-based Zinc Release System.* Plasma Processes and Polymers, 2011. **8**(5): p. 444-451.
9. Al-Jumaili, A., et al., *Plasma Treatment of Polymeric Membranes*, in *Non-Thermal Plasma Technology for Polymeric Materials*. 2019, Elsevier. p. 211-240.
10. Malzahn, K., et al., *Antimicrobial Activity and Cyto-Compatibility of Plasma Polymerized Zinc Acetylacetonate Thin Films.* Plasma Processes and Polymers, 2013. **10**(3): p. 243-249.
11. Al-Jumaili, A., K. Bazaka, and M.V. Jacob, *Retention of Antibacterial Activity in Geranium Plasma Polymer Thin Films.* Nanomaterials, 2017. **7**(9): p. 270.
12. Bayram, O. and O. Simsek, *Investigation of the effect of RF energy on optical, morphological, chemical and antibacterial properties of PolyTerpenol thin films obtained by RF-PECVD technique.* Journal of Materials Science: Materials in Electronics, 2018. **29**(8): p. 6586-6593.
13. Jacob, M.V., et al., *Plasma polymerised thin films for flexible electronic applications.* Thin Solid Films, 2013. **546**: p. 167-170.
14. Hanisch, C., et al., *Fast electrical response to volatile organic compounds of 2D Au nanoparticle layers embedded into polymers.* Journal of Materials Science, 2011. **46**(2): p. 438-445.
15. Bauhofer, W. and J.Z. Kovacs, *A review and analysis of electrical percolation in carbon nanotube polymer composites.* Composites Science and Technology, 2009. **69**(10): p. 1486-1498.

16. Coelho, P.H.d.S.L., et al., *Electrical percolation, morphological and dispersion properties of MWCNT/PMMA nanocomposites.* Materials Research, 2014. **17**: p. 127-132.
17. Ahmed Al-Jumaili, P.M., Avishek Kumar, Kateryna Bazaka, Karthika Prasad, Jeff Warner and Mohan V. Jacob *Eco-friendly nanocomposites derived from geranium oil and zinc oxide in one step approach*, in *Scientific Reports*. 2018.
18. Nohynek, G., E. Dufour, and M.S. Roberts, *Nanotechnology, cosmetics and the skin: is there a health risk?* Skin pharmacology and physiology, 2008. **21**(3): p. 136-149.
19. Nohynek, G.J., et al., *Grey goo on the skin? Nanotechnology, cosmetic and sunscreen safety.* Critical reviews in toxicology, 2007. **37**(3): p. 251-277.
20. Hong, J.I., et al., *Dielectric properties of zinc oxide/low density polyethylene nanocomposites.* Materials Letters, 2005. **59**(4): p. 473-476.
21. Ge, H., et al., *Size dependence of the polarization and dielectric properties of KNbO 3 nanoparticles.* RSC Advances, 2014. **4**(44): p. 23344-23350.
22. Al-Turki, A.M., *Effect of Preparation Methods on the Particles Size, Dielectric Constant and Antibacterial Properties of ZnO Nanoparticles and Thin Film of ZnO/Chitosan.* ORIENTAL JOURNAL OF CHEMISTRY, 2018. **34**(1): p. 548-554.
23. Sagadevan, S., et al., *Structural, dielectric and optical investigation of chemically synthesized Ag-doped ZnO nanoparticles composites.* Journal of Sol-Gel Science and Technology, 2017. **83**(2): p. 394-404.
24. Nan, C.-W., et al., *Grain size-dependent electrical properties of nanocrystalline ZnO.* Journal of applied physics, 1999. **85**(11): p. 7735-7740.
25. Dakhel, A., *Mechanisms of dc-current transfer in tris (acetylacetonato) iron (III) films.* Journal of non-crystalline solids, 2007. **353**(16): p. 1529-1533.
26. Ahmad, J., et al., *Electrical conduction in plasma polymerized thin films of γ-terpinene.* Journal of Applied Polymer Science, 2015. **132**(30).
27. Capan, R. and F. Davis, *Electrical properties of a calix [4] acid/amine Langmuir–Blodgett thin film.* Materials Chemistry and Physics, 2011. **125**(3): p. 883-886.
28. Ren, L., et al., *Coulomb block effect inducing distinctive dielectric properties in electroless plated barium titanate@ silver/poly (vinylidene fluoride) nanocomposites.* RSC Advances, 2015. **5**(80): p. 65167-65174.
29. Roldughin, V.I. and V.V. Vysotskii, *Percolation properties of metal-filled polymer films, structure and mechanisms of conductivity.* Progress in Organic Coatings, 2000. **39**(2): p. 81-100.
30. Hong, J., et al., *Rescaled electrical properties of ZnO/low density polyethylene nanocomposites.* Applied physics letters, 2003. **82**(12): p. 1956-1958.

31. Celzard, A., et al., *Critical concentration in percolating systems containing a high-aspect-ratio filler.* Physical Review B, 1996. **53**(10): p. 6209.
32. Pleşa, I., et al., *Properties of Polymer Composites Used in High-Voltage Applications.* Polymers, 2016. **8**(5): p. 173.
33. Feng, J., et al., *Enhanced electrical conductivity of poly (methyl methacrylate) filled with graphene and in situ synthesized gold nanoparticles.* Nano Futures, 2018. **2**(2): p. 025003.
34. Batool, A., et al., *Synthesis of polypyrrole/zinc oxide composites and study of their structural, thermal and electrical properties.* Synthetic Metals, 2012. **161**(23): p. 2753-2758.
35. Tjong, S.C. and G.D. Liang, *Electrical properties of low-density polyethylene/ZnO nanocomposites.* Materials Chemistry and Physics, 2006. **100**(1): p. 1-5.
36. Wang, G., et al., *Fabrication of radial ZnO nanowire clusters and radial ZnO/PVDF composites with enhanced dielectric properties.* Advanced Functional Materials, 2008. **18**(17): p. 2584-2592.
37. Al-Jumaili, A., et al., *The Electrical Properties of Plasma-Deposited Thin Films Derived from Pelargonium graveolens.* Electronics, 2017. **6**(4): p. 86.

Chapter VI

Antimicrobial Behaviour of Vertical Graphene Synthesized Using PECVD

The formation of high quality vertical graphene by PECVD technique is described in chapter VI. Surface characterization, optical transparency, Raman spectroscopy, and the antibacterial performance of the formed graphene are systematically presented in this chapter.

Abstract

Graphene exhibited a wide range of remarkable properties suitable for many applications including biomedical applications. Plasma-enhanced chemical vapour deposition (PECVD) had been utilized for the fabrication of high-quality vertical graphene from sustainable geranium essential oil on silicon and quartz substrates without use any catalyst. Raman spectra of the samples substantiated the graphene growth. SEM of the sample exhibited vertical growth of graphene and in addition, AFM confirmed the very sharp edges of the produced graphene. The material revealed relatively high water contact angle value ranging around 123˚. Antibacterial performance of graphene nano-walls was studied against gram-positive and gram-negative microorganisms. Confocal scanning laser microscopy images demonstrated that 32% and 38% of *E.coli* and *S. aureus* cells were alive on graphene compare to controls that showed 80% and 82%, respectively.

VI.1. Introduction

Graphene is one-atom-thick planar layer of sp^2-bonded carbon that densely constructed in a honeycomb crystal lattice [1]. Graphene-related materials have received great attention due to its extraordinary features such as high electrical and thermal conductivity, extraordinary hardness and chemical inertness. Furthermore, graphene is well-known for the extra ordinarily high surface area (2630 m^2/g), super hydrophobicity (~150˚) and high optical transmittance of around 97% over the entire wavelength region [2, 3].

The characteristics of graphene-based materials are highly relevant for their biological activities since numerous reports have been published on contributing of graphene into biosensors, tissue scaffolds, drug/gene delivery, antibacterial agents, and bioimaging probes [4-8]. More importantly, graphene offers a promising potential to engage with microorganisms. Graphene also demonstrated wide-spectrum antimicrobial activity toward important human pathogens [9, 10]. The antimicrobial performance of graphene is believed to be instigated by physical and/or chemical interactions upon

direct contact with microbial cells. Although bactericidal mechanisms of graphene-based materials have theoretically and experimentally investigated in many studies, their antibacterial mechanisms still controversial.

Plasma enhanced chemical vapor deposition (PECVD) has advantages to yield uniform vertically grown graphene (VG) without using any catalyst. Reactive species generated in the plasma field are effective in breaking the bonds of carbon-based precursors decreasing the required temperature for graphene fabrication. PECVD is a bottom-up technique that highly-versatile and feasible for large-area production of graphene structures at reasonable growth rates [11, 12]. Furthermore, it allows for preservation of original minerals existing in the precursor, resulting in varying morphologies and chemistries of the fabricated materials [13]. The properties of the designed graphene are strongly dependent on precursor, plasma power, temperature, growth time and substrate coating.

Synthesis of graphene from inexpensive natural precursors is of great interest from both ecological and industrial point of view [14]. Essential oils, in particular, represent a promising renewable precursor for producing graphene through PECVD, since they are volatile oily liquid that can evaporate at room temperature without any carrier gas [15] . A previous study reported successfully synthesis vertically-oriented graphene walls from tea tree essential oil (*Melaleuca alternifolia*) utilizing a green catalyst-free low temperature PECVD. The resultant graphene material demonstrated enhanced surface area with ultra-long edges, high surface roughness, and low level of defects [16].

In this study, geranium essential oil (*Pelargonium Graveolens*) was selected as precursor. It is a hydrocarbon-rich mixture containing around 85 components [17]. The main compounds include 32% citronellol ($C_{10}H_{20}O$), 15% geraniol ($C_{10}H_{18}O$), 6%linalool ($C_{10}H_{18}O$), 6% isomenthone ($C_{10}H_{18}O$), 6% citronellyl formate ($C_{11}H_{20}O_2$), 5% guaia-6,9-diene ($C_{15}H_{24}$), 5% 10-epi-γ eudesmol ($C_{15}H_{26}O$), 2.5%geranyl formate ($C_{11}H_{18}O_2$), and 2% tiglate ($C_5H_8O_2$). The precursor was introduced to a single-step PECVD for fabrication high quality and large surface area vertically oriented graphene.

VI.2. Experimental

VI.2.1. Graphene fabrication

Silicon (with 100 nm oxide layer) and quartz substrates (1x1 cm^2) were washed with acetone propanol, and dried by air gun. The graphene was fabricated using single step PECVD technique. The plasma system, shown in figure VI.1, consists of a quartz tube reactor with external heater. An adjustable voltage regulator was utilized to obtain the required temperature of 800 °C. The initial pressure was kept around 0.05 mbar. Then, the pressure of the system was kept at 0.20 mbar when H_2 gas flown at the rate of 10 sccm. The input power of 500 W supplied from the Navio RF Generator operating at 13.56 MHz frequency through the Navio Matching Network. Prior to growth, substrates were pretreated with plasma for 1 min for surface preparation. The vaporized precursor was then introduced

into the reactor using a flow controller. The precursor (geranium oil) was obtained from Australian Botanical Products (ABP, Victoria, Australia) that used without further modification.

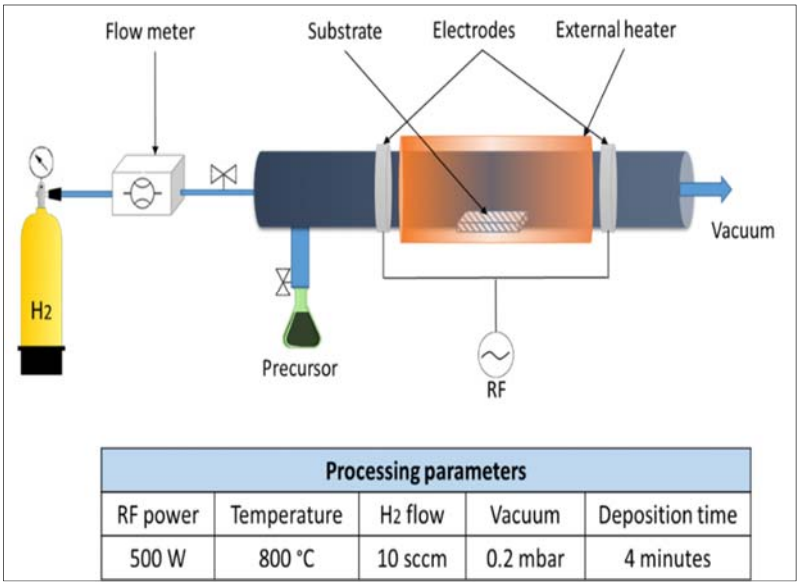

Processing parameters				
RF power	Temperature	H_2 flow	Vacuum	Deposition time
500 W	800 °C	10 sccm	0.2 mbar	4 minutes

Figure VI.1. Plasma enhanced chemical vapor deposition system for graphene fabrication.

VI.2.2. Graphene characterization

The Raman spectra were acquired using a WITec's Raman spectrometer (WITec, Ulm, Germany) with laser excitations of 532 nm.

Static water contact angle measurements were preformed to determine the wettability of VG. Contact angle was recorded using goniometer (KSV CAM 101, Helsinki, Finland). Young–Laplace fitting was used to evaluate the contact angle and a minimum of three measurements per sample is performed.

Surface morphology was inspected using a high-resolution and low-noise scanning atomic force microscope AFM (NT-MDT NTEGRA, Moscow, Russian) with a scanning area of 4 µm × 4 µm. AFM was activated in the tapping mode, where the cantilever oscillated directly above the surface to obtain records. The data then analyzed using Nova Software (Version 1.0.26, Moscow, Russian) with the fitting correction value (polynomial order of 4).

Optical transparency was identified using Variable Angle Spectroscopic Ellipsometry (JA Woollam-M2000 D, Lincoln, NE, USA) with a software package (WVASE32, Lincoln, NE, USA).

Scanning Electron Microscopy (SEM) (SU5000, Hitachi, Canada) was employed to image VG samples fabricated on silicon. Data were gained at Vacc = 3.0kV, EC= 124K nA, WD=9.0 mm.

The antibacterial performance of VG was evaluated by Live/Dead staining method toward Escherichia coli (gram-negative) and Staphylococcus aureus (gram-positive). The experiment was run in triplicate.

For each experiment, a fresh bacterial suspension was prepared by first refreshing the frozen stock culture (1 mL) in Oxoid nutrient broth (10 mL) at 37 °C in shaking mode at 120 rpm. A spectrometer (The SPECTROstar Nano, BMG labtech, Germany) was used to estimate cell numbers in a bacterial suspension prior to placing them onto graphene surfaces. The cell density was kept at (OD_{600} = 0.1) to make sure uniform starting culture (2×10^5 cell/ CFU).

Controls (quartz substrates) and VG samples were placed into 12-well plates, then irradiated by UV-light for 20 min to sterilize the samples. An aliquot of 2 ml of bacterial suspension was placed onto the sample surface. All tested samples were incubated at 37 °C and 5% CO_2 for 24 h. After the incubation time, a staining kit (SYTO™ Invitrogen, Thermo Fisher, USA) was performed to study live/dead microbial cells. The dyes were used following the protocol outlined in [18]. Prior to imaging, bacterial suspensions were removed from the samples. A 90 µl of the stain were kept on top of each sample and retained in the dark. After 20 min, samples were lightly washed with 0.5 ml of distilled water to remove unattached bacteria. Fluorescent images were acquired with a confocal laser scanning microscope (LSM 800, ZEISS, Germany), as green and red cells were refer of live and non-viable cells, respectively. Viability was assessed as the percentage of viable, adhering bacteria relative to the total number of attached bacteria to the surface.

VI.3. Results and discussion

VI.3.1 The Raman spectroscopy

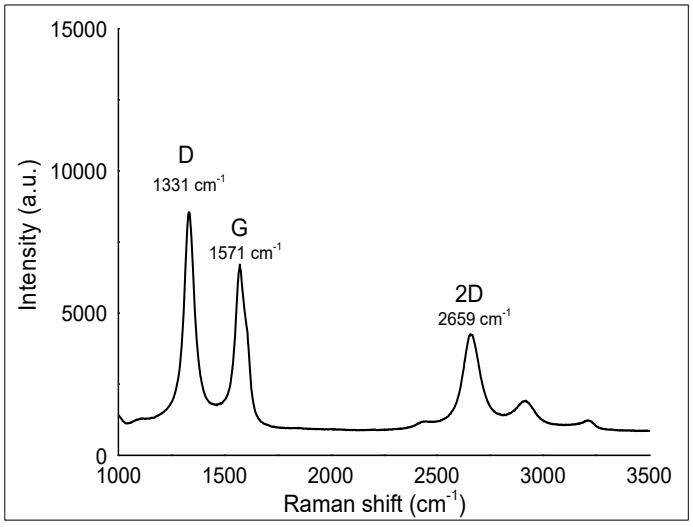

Figure VI.2. Raman spectra of vertically grown graphene deposited from geranium oil on silicon substrates.

The Raman spectrum of graphene synthesized from geranium oil is presented in Figure VI.2. The D peak at around 1331 cm^{-1} is initiated by the disordered structure of the graphene nano-wall such as random orientation of the crystalline, fullerene-like structure, and local defects [19-21]. The G peak at

1571 cm^{-1} represents sp^2 variations in the graphic planes [22]. The shape and position of the 2D peak reflects the number of the graphene layers. Here, Raman spectra of the graphene samples displayed a 2D peak at 2659 cm^{-1}, demonstrating the graphene formation. The 2D peak showed a full width at half-maximum (fwhm) of approximately 70 cm^{-1} at 2659 cm^{-1}, indicating five layer of graphene [23]. The ratio of I2D/IG bands indicates the number of layers of the formed graphene, where the increased ratio point toward the formation of thinner graphene matrix [24]. The I2D/IG ratio of the graphene was estimated to be 0.62. Furthermore, the ratio of ID/IG was equal to 1.26, indicating that graphene had defect densities and are mostly consisted of sp^2 hybridized carbon [16].

VI.3.2 Surface characteristics

The morphologies of VG were observed by SEM at different magnifications (figures VI.3 a & b) proved that the geranium vapor was transformed to uniform interconnected nano-walls. The graphene is completely covered the substrate and appeared vertically with thickness of 7 to 25 nm. In PECVD, growth mechanism take places through three stages [25], firstly growth of carbon buffer layers around ˜ 20 nm thick parallel to the substrate surface. Then, nucleation of vertical graphene stemmed preferentially from the defects. Finally, vertical growth of graphene [25]. According to Yang et al, the high electric field aligned perpendicular to the surface delivered by the active plasma is key to conducing C sp^3-hybridized atoms as nucleation centers for vertical growth of the graphene. On the other hand, the processing temperature mainly influence the size of the formed graphene [26].

Static water contact angle data were recorded for VG surfaces on a minimum of three points. In each test, the drop profile was acquired for 60 seconds by video camera and solved numerically. The wetting behaviour of graphene generally depends on interconnected effect of several extrinsic and intrinsic elements including chemical structure, morphology, topography, oxygen functionality, crystallinity and defects [27]. Furthermore, the stable electronic structure of graphene results in a relatively low surface energy. The attraction from the non-polar lattice to water molecules is weaker than the binding energy among water molecules [26]. Consequently, the roughness and the surface chemistry of the graphene walls reveal highly hydrophobic outcomes. In this study, the mean water contact angle for VG surfaces was measured to be 123 ˚ as shown in figure VI.3 c. The high value of contact angle indicates that a high ratio of sp^2-hybridized bonding and electrons coupling effect enhanced the repellent of polar liquid like water. Besides, contact angle could be improved by quantities of cavities formed by interweaved graphene walls causing the hydrophobic surface performance [28].

AFM image in figure 3 d revealed that VG had a smooth planar structure with surface roughness value ranging around 2.5 nm. The morphology seems to be same as presented in the SEM images. The line scan of the AFM image, as shown in figure VI.3 e, of the surface provides further details about the width of the graphene walls. The thickness of individual nano-wall tip/edge was estimated to be 10 to 20 nm (as explained by red arrows in figure 3 e). This indicates ultra-thin and very sharp edges of the

formed graphene. Compared to 2D graphene, the vertically oriented graphene has definite specific features such as high surface area and very long edges giving exclusive functionalities. Such a property would probably facilitate its integration in low-cost, eco-friendly, self-cleaning surfaces.

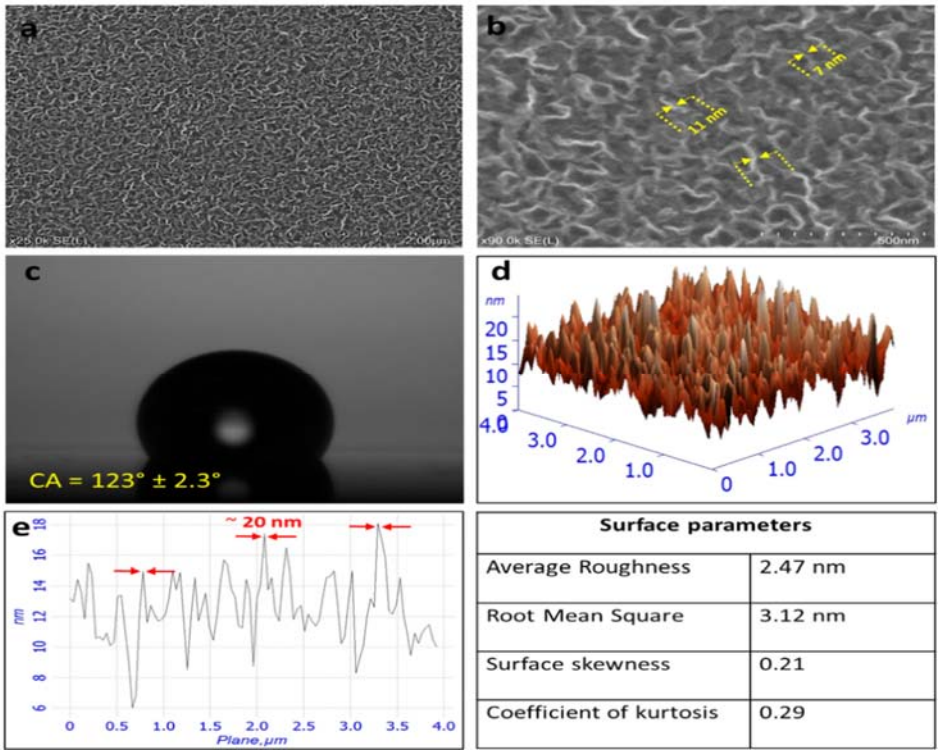

Figure VI.3: (a) & (b) are SEM images of graphene materials acquired at magnifications of 25,000 X and 90,000 X, respectively. (c) is an image of static water contact angle on graphene surface. (d) is AFM image of graphene material. (e) is line spectra from the AFM image and its corresponding surface parameters presented in the given table.

In order to measure the transparency of VG, the optical transmittance was acquired across wavelength of 200 to 1000 nm, as exhibited in figure VI.4. Few layer Graphene revealed high transparency in the visible region. At the wavelength of 550 nm, VG possessed an optical transmittance measured as 82.1%, which is comparable to some previous reports [29, 30]. The obtained transparency of the films can be attributed to graphene's unique electronic structure. Although the transmittance of one atom thick is 97.7%, the absorption of graphene multi-layers system is found to be proportional to the number of layers, where each layer absorb a significant fraction equal to 2.3% of incident light [31]. This unique optical property at a wide range of wavelengths will make the VG useful as coatings for optoelectronics applications.

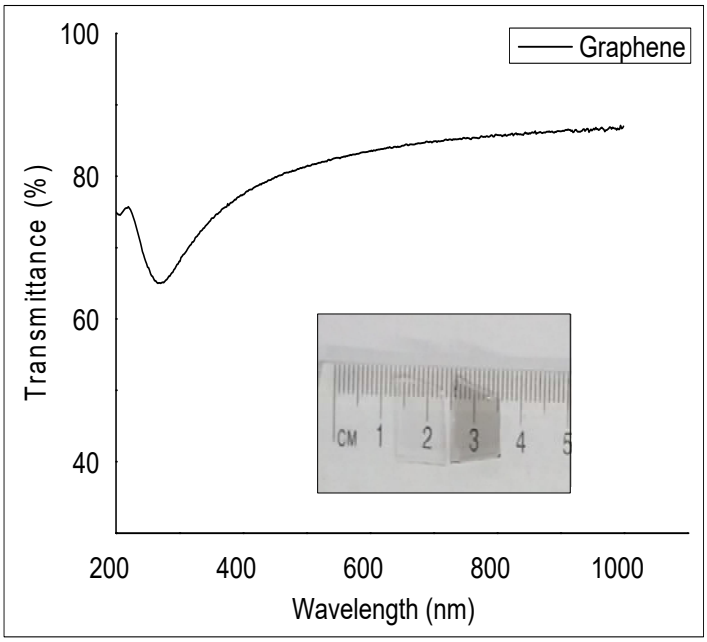

Figure VI.4. Optical transmittance spectra of the graphene films fabricated on quartz substrates.

VI.3.3 The antibacterial performance

The antibacterial performance of VG materials was evaluated against rod-shaped *E. coli* (gram-negative cell) and *S. aureus* (gram-positive cell) in terms of bacteria viability using Live/Dead cell confocal imaging procedure. The ratio of live bacterial cell against the total number of bacteria (both live and dead cells) was determined to calculate the antibacterial performance of the graphene. All data were recorded with a minimum of three replicates. Statistical analysis of numerical data was calculated employing a paired t-test. Statistical significance (*) was measured at $p < 0.05$. Additionally, a confidence interval (95%) was given at each time point, which was considered as an additional pathway to guarantee statistical differences between experimental and control data.

Bactericidal activity of VG against *E. coli* bacteria is presented in figure VI.5. CLSM images clearly show a much higher average number of dead bacterial cells on the graphene samples compare to the control surface. It was estimated that around 80% of *E.coli* were alive on the control, while cells viability on the VG was estimated to be 32%. This indicate a significant reduction in the number of viable cells as shown by statistical analysis bar chart in figure VI.5. Similarly, figure VI.6 showed the bactericidal performance of graphene nanowalls against *S. aureus* pathogen was also significant, where 38% of bacterial cells were viable. Graphene walls revealed much higher antibacterial efficacy against *E. coli* than *S.aureus*. This observation can be attributed to the inherent-differences in the cell wall configuration in gram-negative and gram-positive microorganisms. A gram positive cell has a thick peptidoglycan layer that consists of teichoic and lipoteichoic acids. While a

gram negative cell has a thin peptidoglycan layer and a superficial-membrane that consists of lipopolysaccharide, phospholipids, and proteins.

The dissimilar fundamental properties of graphene materials such as size, layers number, shapes, presence of oxygen, hydrophilicity, quality of the individual graphene wall, defect density, etc. make it challenging to predict their precise antimicrobial mechanisms/models [32]. However, they were categorized into two main categories: physical distraction and chemical oxidation. Physically, the very sharp edges of graphene nanowalls can damage/cut microbial cell membrane, resulting in bacteria cell inactivation [33]. Furthermore, the graphene sheet may extremely extracts phospholipid molecules from the lipid layers of the membranes triggering distortion and irreversible damage of the cell membrane [34]. It had also found that a graphene sheet with a higher oxidization degree can affect a larger scale of irregular membrane perturbation damaging the integrity of the membrane [35]. A recent report observed that vertically oriented graphene oxide nano-sheets revealed a substantially higher degree of antibacterial performance against bacterial cell, compared to randomly oriented and horizontally covered graphene oxide [36].

The chemical oxidation due to graphene materials has also been reported as an additional bactericidal mechanism in the literature. Oxidative stress can be induced via ROS-dependent or ROS-independent pathways. ROS such as hydrogen peroxide, hydroxyl radicals, singlet molecular oxygen and superoxide anions are known to harm biological molecules. The over-production of ROS by graphene causes cells to enter a state of oxidative stress, causing extra destruction to microbial cellular components such as DNA, lipids, proteins and gradual degeneration of cell membrane [37, 38]. Oxidative stress can also be triggered without ROS-formation, where graphene materials act as an electron pump removing charges from microbial cellular membrane [38]. However, some studies observed that the bactericidal effect of vertical PECVD graphene is not related to the generation of oxidative stress [39].

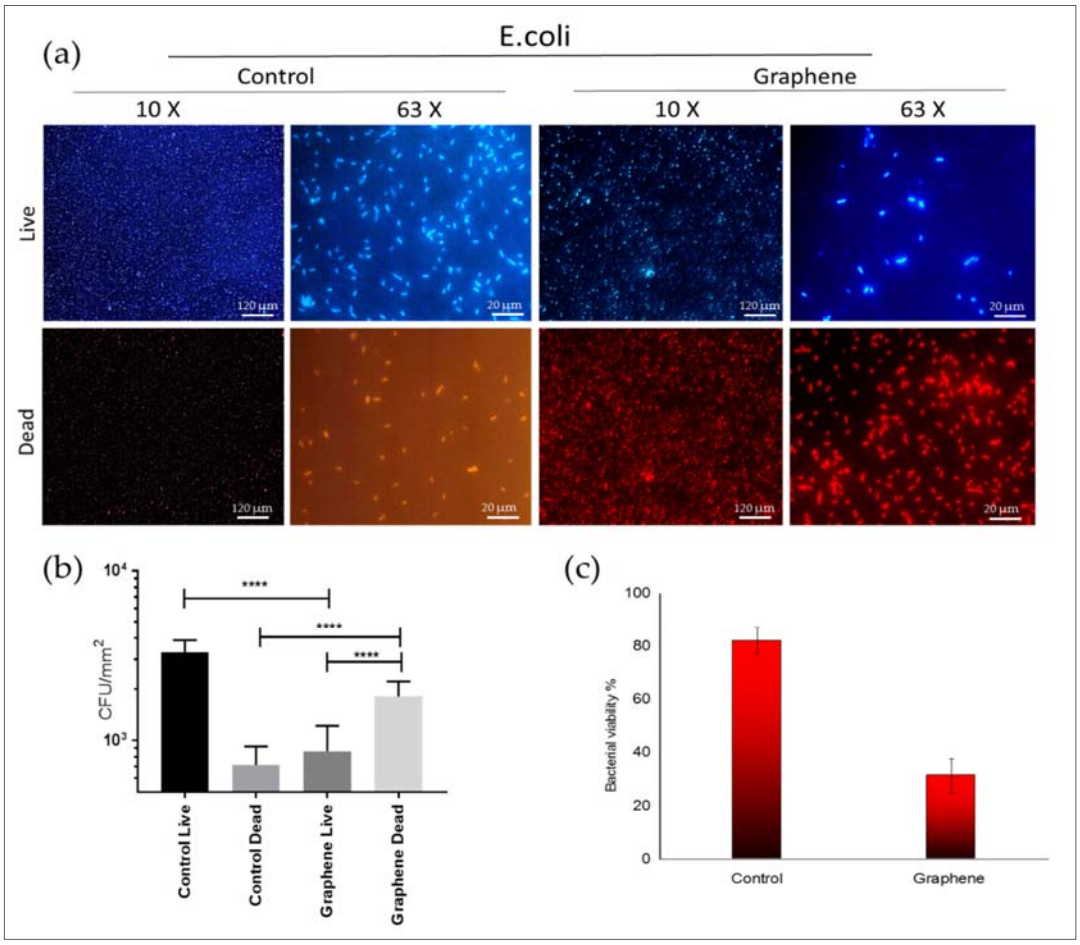

Figure VI.5. The antimicrobial performance of VG toward *E.coli* bacteria, (a) are confocal scanning laser microscopy images of visualize viable cells stained green and dead cells stained red with Invitrogen Dead/Live Kit for live/dead cells at different magnifications (10 X and 63 X). The statistical analysis chart (b) shows the antibacterial performance of graphene and controls (quartz substrates). Data shown represent means ± SD (n = 3). The statistical significance is given in terms of * ($P < 0.05$). The bar chart (c) displays the bacterial viability on the samples.

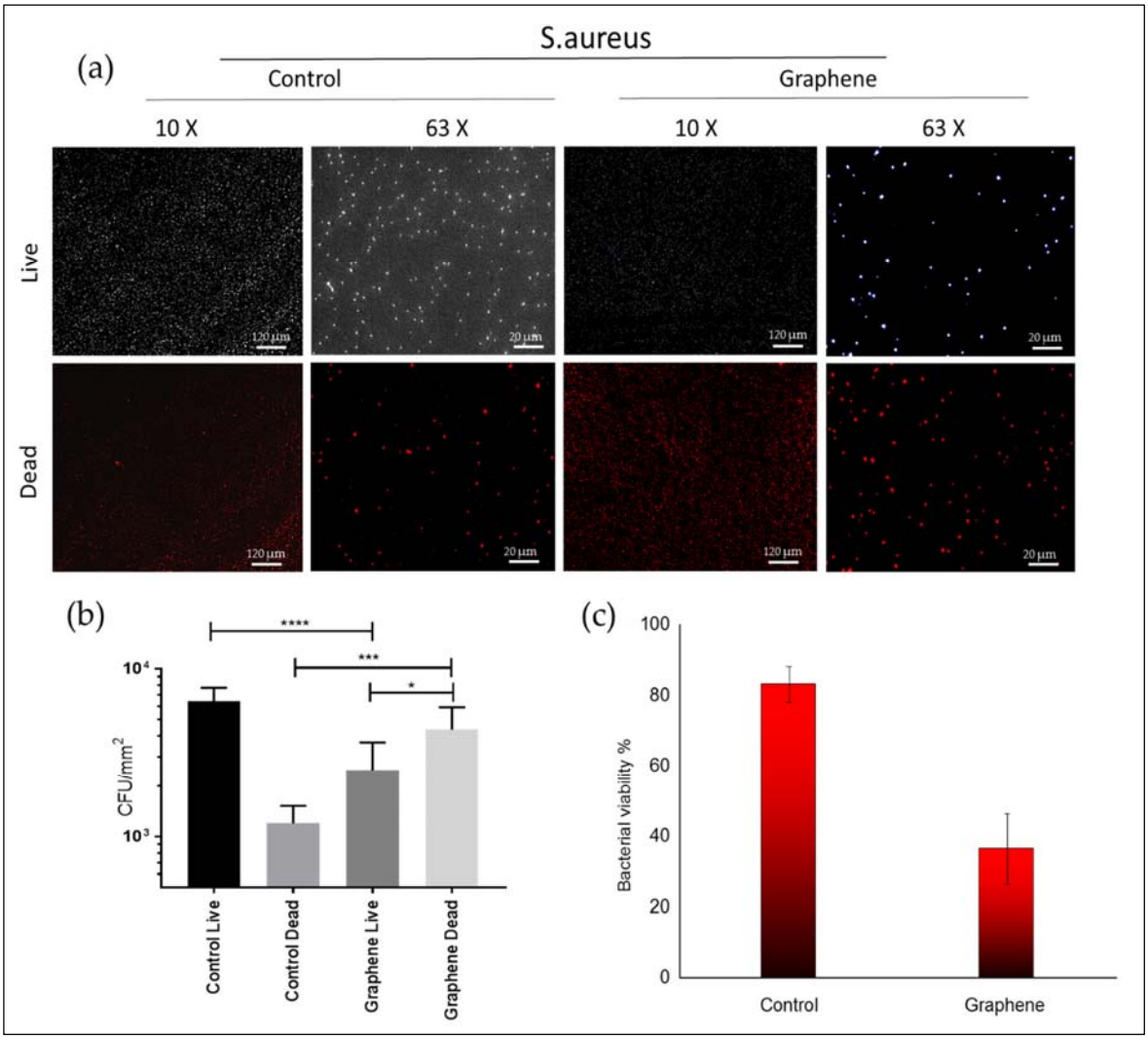

Figure VI.6. The antimicrobial performance of VG toward *S.aureus* bacteria, (a) are confocal scanning laser microscopy images of visualize viable cells stained green and dead cells stained red with Invitrogen Dead/Live Kit for live/dead cells at different magnifications (10 X and 63 X). The statistical analysis chart (b) shows the antibacterial performance of graphene and controls (quartz substrates). Data shown represent means ± SD (n = 3). The statistical significance is given in terms of * ($P < 0.05$). The bar chart (c) displays the bacterial viability on the samples.

VI.4. Conclusion

This work successfully demonstrated the synthesis of uniform vertical graphene from geranium essential oil using single-step PECVD. The fundamental characteristics showed that the graphene is of good quality and is of vertically aligned. The VG graphene showed hydrophobic surface characteristics with water contact angle value of 123˚. The material possessed an optical transmittance measured as 82.1% that appropriate for different optoelectronics applications. The antibacterial performance of the material was demonstrated toward gram positive and gram negative pathogens. The viability of

E.coli and *S. aureus* cells were found to be 32% and 38% on graphene surfaces. The graphene is derived from a cheap and sustainable precursor, easy to re-produce, well-controlled processing parameters. The developed graphene has showed impressive potential in tackling various aspects of microbial infections in many biomedical applications.

References

1. Choi, W., et al., *Synthesis of Graphene and Its Applications: A Review.* Critical Reviews in Solid State and Materials Sciences, 2010. **35**(1): p. 52-71.
2. Bonaccorso, F., et al., *Graphene, related two-dimensional crystals, and hybrid systems for energy conversion and storage.* Science, 2015. **347**(6217): p. 1246501.
3. Prydatko, A.V., et al., *Contact angle measurement of free-standing square-millimeter single-layer graphene.* Nature Communications, 2018. **9**(1): p. 4185.
4. Kuila, T., et al., *Recent advances in graphene-based biosensors.* Biosensors and Bioelectronics, 2011. **26**(12): p. 4637-4648.
5. Kalbacova, M., et al., *Graphene substrates promote adherence of human osteoblasts and mesenchymal stromal cells.* Carbon, 2010. **48**(15): p. 4323-4329.
6. Sanchez, V.C., et al., *Biological interactions of graphene-family nanomaterials: an interdisciplinary review.* Chemical research in toxicology, 2011. **25**(1): p. 15-34.
7. Zhang, L., et al., *Functional graphene oxide as a nanocarrier for controlled loading and targeted delivery of mixed anticancer drugs.* Small, 2010. **6**(4): p. 537-544.
8. Goncalves, G., P. Marques, and M. Vila, *Graphene-based Materials in Health and Environment: New Paradigms*. 2017: Springer.
9. Rojas-Andrade, M.D., et al., *Antibacterial mechanisms of graphene-based composite nanomaterials.* Nanoscale, 2017.
10. Kim, T.I., et al., *Antibacterial Activities of Graphene Oxide-Molybdenum Disulfide Nanocomposite Films.* ACS Applied Materials & Interfaces, 2017.
11. Yuan, G., et al., *Graphene sheets via microwave chemical vapor deposition.* Chemical Physics Letters, 2009. **467**(4-6): p. 361-364.
12. Ostrikov, K. and A. Murphy, *Plasma-aided nanofabrication: where is the cutting edge?* Journal of Physics D: Applied Physics, 2007. **40**(8): p. 2223.
13. Bazaka, K., et al., *Anti-bacterial surfaces: natural agents, mechanisms of action, and plasma surface modification.* RSC Advances, 2015. **5**(60): p. 48739-48759.
14. Bazaka, K., M.V. Jacob, and K. Ostrikov, *Sustainable Life Cycles of Natural-Precursor-Derived Nanocarbons.* Chemical reviews, 2015. **116**(1): p. 163-214.
15. Ouyang, B., et al., *Green synthesis of vertical graphene nanosheets and their application in high-performance supercapacitors.* RSC Advances, 2016. **6**(28): p. 23968-23973.
16. Jacob, M.V., et al., *Catalyst-free plasma enhanced growth of graphene from sustainable sources.* Nano letters, 2015. **15**(9): p. 5702-5708.

17. Jalali-Heravi, M., B. Zekavat, and H. Sereshti, *Characterization of essential oil components of Iranian geranium oil using gas chromatography–mass spectrometry combined with chemometric resolution techniques.* Journal of Chromatography A, 2006. **1114**(1): p. 154-163.
18. Scientific, T.F. *LIVE/DEAD® BacLight Bacterial Viability Kits*. 2004; Available from: https://assets.thermofisher.com/TFS-Assets/LSG/manuals/mp07007.pdf.
19. Ni, Z., et al., *Raman spectroscopic investigation of carbon nanowalls.* The Journal of chemical physics, 2006. **124**(20): p. 204703.
20. Blank, V., et al., *High pressure transformation of single-crystal graphite to form molecular carbon–onions.* Nanotechnology, 2007. **18**(34): p. 345601.
21. Somanathan, T., et al., *Graphene oxide synthesis from agro waste.* Nanomaterials, 2015. **5**(2): p. 826-834.
22. Kim, K.S., et al., *Large-scale pattern growth of graphene films for stretchable transparent electrodes.* Nature, 2009. **457**: p. 706.
23. Eda, G., G. Fanchini, and M. Chhowalla, *Large-area ultrathin films of reduced graphene oxide as a transparent and flexible electronic material.* Nature nanotechnology, 2008. **3**(5): p. 270.
24. Bi, H., et al., *Direct growth of few-layer graphene films on SiO 2 substrates and their photovoltaic applications.* Journal of Materials Chemistry, 2012. **22**(2): p. 411-416.
25. Zhang, L.X., et al., *Understanding the growth mechanism of vertically aligned graphene and control of its wettability.* Carbon, 2016. **103**: p. 339-345.
26. Yang, C., et al., *Direct PECVD growth of vertically erected graphene walls on dielectric substrates as excellent multifunctional electrodes.* Journal of Materials Chemistry A, 2013. **1**(3): p. 770-775.
27. Ghosh, S., et al., *Process-specific mechanisms of vertically oriented graphene growth in plasmas.* Beilstein journal of nanotechnology, 2017. **8**: p. 1658-1670.
28. Watanabe, H., et al., *Control of super hydrophobic and super hydrophilic surfaces of carbon nanowalls using atmospheric pressure plasma treatments.* Japanese Journal of Applied Physics, 2012. **51**(1S): p. 01AJ07.
29. Sun, J., et al., *Direct low-temperature synthesis of graphene on various glasses by plasma-enhanced chemical vapor deposition for versatile, cost-effective electrodes.* Nano Research, 2015. **8**(11): p. 3496-3504.
30. Becerril, H.A., et al., *Evaluation of solution-processed reduced graphene oxide films as transparent conductors.* ACS nano, 2008. **2**(3): p. 463-470.
31. Nair, R.R., et al., *Fine structure constant defines visual transparency of graphene.* Science, 2008. **320**(5881): p. 1308-1308.

32. Al-Jumaili, A., et al., *Review on the Antimicrobial Properties of Carbon Nanostructures.* Materials, 2017. **10**(9): p. 1066.
33. Akhavan, O. and E. Ghaderi, *Toxicity of graphene and graphene oxide nanowalls against bacteria.* ACS nano, 2010. **4**(10): p. 5731-5736.
34. Tu, Y., et al., *Destructive extraction of phospholipids from Escherichia coli membranes by graphene nanosheets.* Nature nanotechnology, 2013. **8**(8): p. 594-601.
35. Mao, J., R. Guo, and L.-T. Yan, *Simulation and analysis of cellular internalization pathways and membrane perturbation for graphene nanosheets.* Biomaterials, 2014. **35**(23): p. 6069-6077.
36. Lu, X., et al., *Enhanced antibacterial activity through the controlled alignment of graphene oxide nanosheets.* Proceedings of the National Academy of Sciences, 2017: p. 201710996.
37. Krishnamoorthy, K., et al., *Antibacterial efficiency of graphene nanosheets against pathogenic bacteria via lipid peroxidation.* The Journal of Physical Chemistry C, 2012. **116**(32): p. 17280-17287.
38. Li, J., et al., *Antibacterial activity of large-area monolayer graphene film manipulated by charge transfer.* Scientific reports, 2014. **4**: p. 4359.
39. Pandit, S., et al., *Vertically Aligned Graphene Coating is Bactericidal and Prevents the Formation of Bacterial Biofilms.* Advanced Materials Interfaces, 2018. **5**(7): p. 1701331.

Chapter VII

Conclusions and Recommendations for Future Work

The interest in the development of effective antibacterial coatings has recently been progressively increasing due to substantial concerns about the microbial-resistance toward synthetics antibiotics. Antimicrobial surfaces particularly that derived from natural essential oils are showing a great potential as active biomaterials in hospital, clinics and implants. In additional to their antimicrobial properties, these materials offer promising features, such as biocompatibility, biodegradable, have good physical stability, costly effective, essential mechanical characteristics, besides reduces the environmental pollution affected by the manufacture of other preservatives. Therefore, research on new naturally-derived, biologically-active coatings and their approaches should yield various possible applications.

Geranium thin films were successfully fabricated using plasma polymerisation at different input power to produce thin films with desired physical, chemical, optical, electrical, biological material characteristics. These properties were discussed and attributed based upon the most recently and commonly reported in literature. Among all processing parameter, the input RF power was founded to be significant to determine material properties.

VII.1. Optical properties

Independent of applied power, geranium oil-derived polymer films were revealed to be optically transparent within the visible wavelength range. Refractive index (n) was found to be not significantly dependent on the RF power. At a short wavelength of 200 nm, the variation in the refractive index between polymers fabricated at applied powers of 10 W and 100 W was approximately ~0.0097. At wavelengths above 900 nm, the variation in the refractive index was ~0.0069. The extinction coefficient (k) also showed very little dependence on the applied power, especially in the high wavelength region (above 900 nm), as the variation was 0.0013. At a short wavelength of 200 nm, the variation in the refractive index for polymers fabricated at applied powers of 10 W and 100 W was ~0.0268. Furthermore, the maximum UV absorption peak was observed at approximately 290 nm, which possibly relates to π–π* transitions. The energy gap of geranium oil-derived polymer films was calculated around $E_g \approx 3.67$ eV. A very small decrease of E_g with an increase in the input power was observed, where samples fabricated at 10, 25, 50, 75, and 100 W had $E_g \approx 3.67$, 3.65, 3.60, 3.61, and 3.60 eV, respectively. The optical properties strongly suggest that geranium films can be used as encapsulating (protective) layers for organic electronics to extend the lifetime and preserve efficiency of oxygen- and water-sensitive organic materials.

VII.2. Surface Topography

Independent of deposition power, the topographical features of the polymers appeared to be uniform, smooth, and pinhole free. The uniformity indicates that polymerisation reactions occurred essentially on the surface of the substrate, instead of in the gas phase. The average roughness parameter was remained below 0.7 nm, which increased slightly as a result of an increase in the input RF power. Moreover, films revealed high spatial uniformity and good adhesion to the substrate. AFM results revealed that the films' entropy also increased as a result of applied power. The entropy increases are possibly related to the surface flatness decreases.

When the ZnO nanoparticles were introduced in the polymers structure, the average roughness parameter significantly increased measuring around 33.7 ± 2.1 and 37.2 ± 2.4 nm for composites fabricated at 10 W and 50 W respectively. The higher surface roughness in comparison with the pristine film indicates that the composite comprised of porous surface with random distribution of ZnO particles.

VII.3. Wettability

In the case of pristine polymers, the water contact angle was 65.6° at deposition power of 100 W, while at the lower power of 10 W, the contact angle value was notably lower, at 55.5°. This was explained by the higher input power conditions produced polymers with highly crosslinked structures due to more fragmentation/dissociation of precursor molecules. Consequently, it caused in the formation of relatively more-rigid polymers as a result of an increase in the bonding interconnection and dense packing of polymer chains within the matrix, minimizing the absorption of water on the surface. This may lead to an increase in the contact angle value, verifying the dependence of contact angle on the degree of crosslinking. Moreover, the increase in the input power affects surface chemistry of the polymers, specifically a decrease in the oxygen content, resulting in a decrease in the polarity of the polymers surfaces.

In the case of composite Zn/Ge films, samples fabricated at 50 W revealed higher contact angle values ranging around 73.4°, while samples fabricated at 10 W revealed approximately 66.4°. This probably is related to the difference in the size of formed nanoparticles at different power of deposition.

VII.4. Chemical Properties

Pristine geranium polymers were founded to be hydrocarbon materials. Carbon was identified to be the main element which contributed up to 87 % and 85 % of the total atomic concentration for samples fabricated at 10 W and 50 W, respectively. Oxygen was identified as a second most abundant element in the films, representing 12 % and 14.45 % of the entire films for geranium films fabricated at 10 W and 50 W. No impurities were identified for any of the pristine polymers.

In composite films, carbon was identified to be around 83 % and 78 % for samples fabricated at 10 W and 50 W, respectively. Likewise, oxygen was estimated to be around 13 % and 16 % for samples fabricated at 10 W and 50 W, respectively. Nitrogen was calculated 2 % and 3 %, and zinc was shown 0.7 % and 1.5 % for samples fabricated at 10 W and 50 W, respectively. It is evident that carbon percentage in the composites decreased with an increase in the power of deposition, which was in contrast to the trend observed in the pristine counterparts. The most rational elucidation for this observation is that the higher input power resulted in a higher fragmentation/dissociation of the zinc acetylacetonate causing a relative increase in oxygen, nitrogen and zinc quantities.

VII.5. Antimicrobial performance

Pristine geranium oil-derived coatings were found to have the potential to reduce the microbial adhesion and biofilm formation of select human pathogens, such as *S. aureus*, *P. aeruginosa* and *E. coli*. The input RF power, in particular, played a substantial role in controlling the surface bio-chemistry and extensively enhanced the biocidal activity of the fabricated coatings. Films deposited at 10 W proved a significant decrease in the number of cells, biovolume, and biofilm thickness. In contrast, there was no significant change in the bacterial colonisation between films fabricated at 50 W and an unmodified glass control.

The antibacterial activity of ZnO-NPs incorporated into geranium films toward both gram-positive (*S. aureus*) and gram-negative (*E. coli*) bacteria were demonstrated. The CLSM imaging evidently showed a much higher average number of cells adhered to the control surface compared to all polymers and composites samples. Although pristine polymers showed weak or moderate antibacterial activity against both gram-positive and gram-negative microorganisms, composites revealed enhanced bactericidal performance. Indeed, zinc nanoparticles were directly involved in the inhibition of the pathogens. In addition, the antibacterial performance of Zn/Ge 10W were greater compared to Zn/Ge 50 W. This observation was linked to the influence of RF power on the size of the formed nanoparticles, where lower power created smaller particles, which revealed much higher antibacterial action in compare to larger nanoparticles.

VII.6. Electrical properties

The electrical properties of pristine and ZnO/composites thin films were systematically studied in metal–insulator–metal structures. The dielectric constant was observed to decrease with increasing deposition power for all samples. Irrespective of power of deposition, all examined polymers almost had the same frequency dependence on the dielectric constant as it sharply decreased in the low frequency region. Additionally, Schottky mechanism was founded to dominant the charge transport mechanisms in the higher field region. Pristine polymers revealed

a relatively low conductivity value (10^{-16}–10^{-17} Ω^{-1} m^{-1}), indicating features of a typical insulator material.

Incorporating ZnO nanoparticles in geranium plasma films did not significantly change the electrical properties nor the charge transport, as the nanocomposite films showed behave as an insulator. It is clear that the composites did not reach the percolation threshold, since the conductivity was kept at relatively low values (10^{-14} Ω^{-1} m^{-1}), rather than increases rapidly. The relative increase in conductivity after introducing ZnO NPs was explained by the increase in the number of dipoles. The high isolation properties, in addition to the antibacterial activities and other desired characteristics of Zn/Ge thin films render them as a suitable candidate for various dielectric applications in advanced microelectronics.

VII.7. Graphene

Vertical graphene from geranium oil is developed using single-step PECVD. The graphene was fabricated at relatively short time (only 4 minutes) directly on silicon and quartz substrates without any catalyst. SEM and AFM confirmed the very sharp edges of graphene walls having a length of few hundreds nanometers with thickness of 7 to 25 nm. The graphene demonstrated high water contact angle value ranging around 123˚. The antibacterial performance of the material was confirmed toward gram positive and gram negative pathogens. Confocal scanning laser microscopy images verified that the viability of *E.coli* and *S. aureus* cells were 32% and 38% were alive on graphene compare to controls, respectively.

Independent of fabrication conditions, several differences can be observed for all fabricated materials in this thesis. Firstly, the topographical features of pristine polymers appeared to be more uniform, and smooth, compared to composites and graphene. Secondly, pristine polymers showed lower contact angle value (˜ 55.5°) compared to composite (66.4°) and graphene (123˚). Thirdly, pristine geranium coatings showed strong anti-biofouling activities, while composites and graphene demonstrated powerful anti-bacterial performance.

In summary, this research contributed to the knowledge of developing plasma polymer thin films from geranium essential oil, incorporating Zinc nano-particles into the fabricated plasma polymer matrix and develop graphene from the geranium essential oil using PECVD. Each of the 3 types of materials were successfully tested to understand the antibacterial nature of the material.

VII.8. Recommendations for future wok

While this study demonstrated geranium plasma polymer thin films as a promising candidate for biomedical and microelectronics applications, it uncovered several questions for further investigation:

- Additional work is required to focus on the degradation and solubility of geranium oil-derived coatings in long-term usage under different environmental conditions. An understanding of the relationship between the processing parameters and the dynamics at the polymer/liquid interface is essential.
- Evaluating the biocompatibility of geranium materials (both pristine and composite films) is very important. Further investigations on eukaryotic cells (human cells) should be achieved in vitro to assess the interaction between of geranium films and human cells for a long period of time. This will enhances opportunities of geranium films to be commercially successful antibacterial coatings for implantable devices.
- As SEM images showed, ZnO particles covered fully/partially with a plasma polymer layer; thus by applying an appropriate energetic plasma on these particles, the polymer layer can be degraded/removed revealing more active-surface area of the ZnO nanoparticle to interact with microorganisms. Further work will assist to explore the influence of different plasma gases, where the optimization of the desired functionality will mainly rely on the input power of the used plasma. Moreover, the influence of Zn nanoparticles can be increased through several ways such reducing the size on the particles, minimizing the aggregation of particles, and increase the number of particles in the polymer.